Possible origin and spectrum of ultrahigh-energy cosmic rays

A. V. Uryson
P. N. Lebedev Physics Institute, Russian Academy of Sciences, 117924 Moscow, Russia

(Submitted 18 February 1997; resubmitted 21 April 1997)
Pis'ma Zh. Éksp. Teor. Fiz. **65**, No. 10, 729–733 (25 May 1997)

The complicated form of the cosmic-ray spectrum recorded in the energy range 10^{17}–10^{20} eV by giant detector arrays is analyzed. It is shown that the spectrum in the region 10^{18}–10^{19} eV is apparently identical to the injection spectrum with power-law exponent approximately equal to $3.2-3.3$. The flat component in the region $(3.2-5)\times 10^{19}$ eV is due to the braking of extragalactic protons by relict photons. The spectrum apparently has no blackbody cutoff at energies above 3.2×10^{19} eV. © *1997 American Institute of Physics.* [S0021-3640(97)00110-2]

PACS numbers: 98.70.Sa

The origin of ultrahigh-energy cosmic rays ($E>10^{17}$ eV) has not been conclusively established. The experimental data show that cosmic rays with energies $E>4\times 10^{19}$ eV are apparently extragalactic.[1–3] If this is so, then their spectrum could have a blackbody cutoff:[4,5] As a result of interactions of cosmic rays with relict photons in the intergalactic space, the recorded flux of 6×10^{19} eV particles will be half the value expected from a power-law extrapolation of the spectrum. However, if the proton sources are no farther away than 40–50 Mpc from us, there will be no blackbody cutoff because protons with any energy up to $E\approx 10^{22}$ eV traverse such distances virtually unimpeded.[6] In Ref. 7 it was shown that the main sources of protons with energy $E>E_{bb}\approx 3.2\times 10^{19}$ eV are apparently nuclei of active galaxies located no farther than 40 Mpc from us, if the Hubble constant equals 75 km/s·Mpc. In this case the proton spectrum has no blackbody cutoff. At present the experimental data obtained with various detector arrays[8–13] neither confirm nor rule out the presence of a blackbody cutoff.

The origin of cosmic rays in the energy range $10^{17}<E\leqslant 10^{19}$ eV has been determined on the basis of not only the spectrum but also the anisotropy and chemical composition.[1–3] However, the existing experimental data are not precise enough to determine whether cosmic rays with such energies are galactic or extragalactic.

In the present work, we analyzed the spectrum of cosmic rays in the energy range $E>10^{17}$ eV in order to determine their origin.

The cosmic-ray spectra measured with the detector arrays of Refs. 8–12 and normalized with respect to energy in the same manner as in Ref. 3 are presented in Fig. 1. The spectrum has the following form:[3,8,10] At $E\sim 5\times 10^{17}$ eV the slope γ of the spectrum increases from $\gamma\approx 3.0$–3.1 to $\gamma\approx 3.2$–3.3 (the error in determining γ equals 0.02–0.06), and in the region $E\sim 10^{19}$ eV it decreases to $\gamma\approx 2.6$–2.7 — a flat component appears in

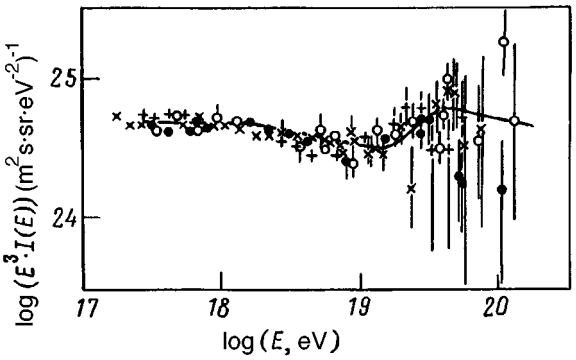

FIG. 1. Cosmic-ray spectra, normalized with respect to energy in the same manner as in Ref. 3, in the region $E>10^{17}$ eV according to measurements performed with the following detector arrays: ● — Yakutsk,[8] × — Akeno and AGASA,[9] + — Fly's Eye,[10] ○ — Haverah Park.[11] Solid line — theoretical spectrum.

the spectrum. The error in determining the slope of the flat component equals 0.1. (The spectral slopes are not given in Refs. 11–13.)

The propagation of protons in the galaxy can be described in the diffusion approximation if their energy does not exceed 10^{17}–10^{18} eV.[14] Furthermore, in Refs. 15–17 it was shown that the particles no longer propagate by diffusion if their energy is greater than some value E_0, the proton spectrum in the energy range $E>E_0$ being identical to the injection spectrum. (We note that this result was obtained by different methods in Refs. 15–17: In Refs. 15 and 16 it was inferred from the drift of ultrahigh-energy cosmic rays in large-scale magnetic fields, while in Ref. 17 it was inferred from a transition to collisionless propagation of particles in a medium in which they excite MHD waves.) An estimate of the energy E_0 was obtained from a numerical simulation of the particle trajectories in the galactic magnetic field:[1] $E_0 \approx 2\times 10^{18}$ eV. Hence it follows that in the region $E \geqslant 2\times 10^{18}$ eV the slope γ_0 for a power-law injection spectrum[1] equals γ, $\gamma_0 = \gamma$.

The region $E \geqslant 2\times 10^{18}$ eV is the region where the slope of the measured spectrum increases. According to the measurements reported in Ref. 18, cosmic rays with such energies consist mostly of protons. This means that their injection spectrum apparently changes at energies $E>10^{18}$ eV: Its slope increases to $\gamma_0 \approx 3.2$–3.3, while for $E<3\times 10^{15}$ eV the slope did not exceed 2.75, $\gamma_0<2.75$.[1] (The slope of the injection spectrum at 3×10^{15}–4×10^{17} eV has not yet been determined, so that we will not make any comparisons for this segment. Different points of view are presented in Refs. 3 and 14.)

Apparently, particles with energy $E>E_{bb}$ are accelerated mainly in sources located no farther than 40–50 Mpc from us,[7,19,20] and so their spectrum has no blackbody cutoff. If this is so, then the slope of the spectrum in this region equals the slope γ_0 of the injection spectrum. Let us assume that in the region $E>E_{bb}$ the injection spectrum is the same as in the region $E \geqslant 2\times 10^{18}$ eV. Then in the region $E>E_{bb}$ the slope of the spectrum will equal $\gamma = 3.2$–3.3.

TABLE I. Computed slope γ_1 of the flat component for different values (within the experimental error) of its upper limit E_3 and the slope γ of the spectrum.

γ	E_3, eV	γ_1
3.0	4.9×10^{19}	2.6
3.05	4.8×10^{19}	2.65
3.05	4.9×10^{19}	2.7
3.1	4.5×10^{19}	2.6
3.2	4.5×10^{19}	2.7
3.25	4.3×10^{19}	2.7
3.3	4.2×10^{19}	2.7

Particles with energy $E>E_{bb}$ which propagate from sources located at distances greater than 40 Mpc from us will interact with the relict radiation until their energy decreases to $E\approx(3.2–5)\times10^{19}$ eV. Particles with such energies may not undergo any interaction in the intergalactic space, since their ranges in the relict radiation field will be quite long — $\lambda>1000$ Mpc.[6] As a result, protons with energies $E>3.2\times10^{19}$ eV are transferred into the region $E\approx(3.2-5)\times10^{19}$ eV, and in consequence the slope of the spectrum in this region will change from $\gamma>3.1$ to γ_1:

$$\int_{E_{bb}}^{\infty} E^{-\gamma}dE=\int_{E_{bb}}^{E_3} E^{-\gamma}dE,$$

where E_3 is the upper limit of the energy range of the flat component. We shall find the value of γ_1 from the data given in Refs. 3 and 8–13. The measured value of E_3 is $E_3\sim4\times10^{19}$ eV, and the particle energy is determined to within $\sim$20–30%.[8,10] For this reason, we estimated the slope γ_1 for several values of E_3 in the interval $4\times10^{19}<E_3<5\times10^{19}$ eV and several values of γ in the interval $3.0<\gamma\leqslant3.3$. The computed values of γ_1 are presented in Table I. Taking into consideration the 30% error in determining the energy, the energy range of the flat component is $E\approx(2-5)\times10^{19}$ eV. It agrees with the measurements performed in Refs. 8, 9, and 11–13 and is not inconsistent with the monocular data presented in Ref. 10. The possible existence of a flat component of this nature in the spectrum was predicted in Refs. 21–23.

Thus protons with energies $E<E_{bb}$ are galactic and protons with energies $E>E_{bb}$ are extragalactic, while the injection spectra of the two types of protons are identical. The theoretical spectrum obtained on the basis of this model for $\gamma_0=3.25$ is displayed in Fig. 1. It is normalized to the intensity measured at $E\approx7\times10^{19}$ eV. Furthermore, it was assumed in the calculations that the flat component lies in the energy range $E\approx(3.2-5)\times10^{19}$ eV. The theoretical spectrum agrees with the measurements within the limits of error.

Let us compare the slopes of the theoretical and measured spectra in the region $E\geqslant10^{19}$ eV. It is evident from Table I that a slope γ_1 in agreement with the slope of the flat component can be obtained on the basis of the proposed model.

To estimate the slope of the measured spectrum in the region $E>E_{bb}$ we shall make use of the experimental data reported in Ref. 3: Up to 1993 only 881 events with energy

$E \geqslant 10^{19}$ eV, seven events with $E \geqslant 10^{20}$ eV, and two events with $E \geqslant 10^{20}$ eV were recorded. For a power-law spectrum with N particles with energy not less than E, $N(\geqslant E)$, we have $N_1(\geqslant E_1)/N_2(\geqslant E_2) = (E_1/E_2)^{\gamma+1}$, whence we obtain $\gamma = 3.1^{+0.2}_{-0.1}$ for $E_1 = 10^{19}$ eV and $E_2 = 10^{20}$ eV.

The energies of some of the 881 events lie in the interval $\approx (1-3.2)\times 10^{19}$ eV, and these events comprise the flat component. Therefore the slope of the spectrum in the region $E > 3.2\times 10^{19}$ eV will be greater than the estimate: $\gamma > 3.1$ and therefore $\gamma_0 > 3.1$.

If there is no blackbody cutoff, the proton spectrum is identical to the injection spectrum in two regions: $2\times 10^{18} \leqslant E < 10^{19}$ eV and $E \geqslant 5\times 10^{19}$ eV. Estimates of the slope of the spectrum in these intervals agree: $\gamma = 3.2-3.3$ and $\gamma > 3.1$. Therefore the measured spectrum apparently has no blackbody cutoff. (In Ref. 3 it was concluded on the basis of the same experimental data that a blackbody spectrum might be present. It was assumed there that if there is no cutoff, then the slope of the spectrum for $E > E_{bb}$ is identical to the slope of the flat component.)

It follows from the picture presented above that in the region of the dip the galactic cosmic rays are replaced by extragalactic cosmic rays. The amplitude of the anisotropy of the galactic cosmic rays for $E > 10^{18}$ eV is somewhat larger than for extragalactic cosmic rays, but because of the large measurement errors their origin still cannot be determined reliably in this manner.[24] Data on the chemical composition in this region are also still not determined. According to the measurements reported in Ref. 10, the composition of cosmic rays in the region $4\times 10^{17} - 4\times 10^{19}$ eV varies — protons start to predominate in this region, but according to the measurements reported in Ref. 18, the proton fraction already starts to increase at $\sim 10^{16}$ eV.

The results obtained can be checked in further measurements of the cosmic-ray spectra in the region $E > 10^{17}$ eV performed with the detector arrays of Refs. 8–11 and with those of Refs. 25 and 26 and also with SHAL-1000,[27] which will have a much better energy resolution.

I am grateful to S. I. Nikol'skiĭ and G. B. Khristiansen for a discussion of the experimental data and to V. A. Dogel' and V. S. Ptuskin for a discussion of galactic cosmic ray propagation models.

[1] V. S. Berezinskiĭ, S. V. Bulanov, V. L. Ginzburg *et al.*, *The Astrophysics of Cosmic Rays* [in Russian], Nauka, Moscow, 1990.
[2] M. N. D'yakonov, T. A. Egorov, N. N. Efimov *et al.*, *Ultra-High-Energy Cosmic Rays* [in Russian], Nauka, Novosibirsk, 1991.
[3] M. Teshima, in *Proc. 23rd ICRC*, Calgary. Invited, Rapporteur and Highlight Papers, edited by D. A. Leakhy, R. B. Hicks, and D. Venkatesan, World Scientific, New York, 1993, p. 257.
[4] G. T. Zatsepin and V. A. Kuz'min, JETP Lett. **4**, 78 (1966).
[5] K. Greisen, Phys. Rev. Lett. **16**, 748 (1966).
[6] F. W. Stecker, Phys. Rev. Lett. **21**, 1016 (1968).
[7] A. V. Uryson, JETP Lett. **64**, 77 (1996).
[8] B. N. Afanasiev, M. N. Dyakonov, T. A. Egorov *et al.* in *Proc. 24th ICRC*, Rome (1995), Vol. 2, p. 756.
[9] M. Nagano *et al.* J. Phys. G: Nucl. Phys. **18,** 423 (1992).
[10] O. J. Bird, S. C. Corbato, H. Y. Dai *et al.*, Astrophys. J. **424**, 491 (1994).
[11] M. A. Lawrence, R. J. O. Reid, and A. A. Watson, J. Phys. G: Nucl. Phys. **17,** 733 (1991).
[12] M. M. Winn, J. Ulrichs, L. S. Deak *et al.*, J. Phys. G: Nucl. Phys. **12,** 653 (1986).

[13] J. Linsley, G. Cunningam, D. M. Edge *et al.*, *Catalogue of Highest Energy Cosmic Rays*, N1, World Data Center C2, Japan, 1980.
[14] V. S. Ptuskin, S. I. Rogovaya, V. N. Zirakashvili *et al.*, Astron. Astrophys. **268**, 726 (1993).
[15] S. I. Syrovatskii, Comments Astrophys. Space Phys. **3**, 155 (1971).
[16] V. S. Berezinsky, A. A. Mikhailov, and S. I. Syrovatskii, *Proc. 16th ICRC*, Kyoto (1979), Vol. 2, p. 86.
[17] V. A. Dogiel, A. V. Gurevich, and K. P. Zybin, Astron. Astrophys. **281**, 937 (1994).
[18] M. N. D'yakonov, V. P. Egorova, A. A. Ivanov *et al.*, JETP Lett. **50**, 442 (1989).
[19] J. Rachen, T. Stanev, and P. Biermann, Astron. Astrophys. **273**, 377 (1995).
[20] R. J. Protheroe and P. A. Johnson, *Proc. 24th ICRC*, Rome (1995), Vol. 3, p. 309.
[21] A. M. Hillas, Can. J. Phys. **21**, 1016 (1968).
[22] C. T. Hill and D. N. Schramm, Phys. Rev. D **31**, 564 (1985).
[23] V. S. Berezinskiĭ and S. I. Grigor'eva, Zh. Éksp. Teor. Fiz. **93,** 812 (1987) [Sov. Phys. JETP **66**, 457 (1987)].
[24] D. N. Pochepkin, V. S. Ptuskin, S. I. Rogovaya *et al.*, *Proc. 24th ICRC*, Rome, **3,** 136 (1995).
[25] M. Teshima *et al.*, Nucl. Phys. B, Proc. Suppl. **28**, 169 (1992).
[26] J. W. Cronin, Nucl. Phys. A **25**, 137 (1992).
[27] S. S. Ameev, I. Y. Chasnikov, Yu. A. Fomin *et al.*, *Proc. 24th ICRC*, Rome (1995), Vol. 1, p. 466.

Translated by M. E. Alferieff

Inclusive semileptonic decays of *B* mesons

S. Ya. Kotkovskiĭ[a)]
Institute of Theoretical and Experimental Physics, 117259 Moscow, Russia

(Submitted 17 April 1997)
Pis'ma Zh. Éksp. Teor. Fiz. **65**, No. 10, 734–737 (25 May 1997)

The probability of inclusive semileptonic decay of *B* mesons is calculated in the constituent-quark model. A compact formula is obtained for the differential decay width of a *B* meson in terms of the corresponding decay width of a free *b* quark and the wave function of the internal motion of the quarks in the *B* meson. Numerical values of semileptonic-decay widths are obtained for a series of models of the wave function. © *1997 American Institute of Physics.* [S0021-3640(97)00210-7]

PACS numbers: 13.20.He, 12.39.Hg

Inclusive decays of *B* mesons in models of the decay of a free *b* quark have been studied many times before.[1,2] In what follows, the probability of the inclusive decay of *B* mesons is calculated in the constituent-quark model, and the quark–hadronic duality principle is checked for different models of the quark wave function. The approach employed below is based on the same method as that developed in Refs. 3 and 4 (which takes into account the nonperturbative coupling of the heavy quark with a spectator), but a number of modifications have been made which have a large effect on the form of the results and make it possible to obtain results in a form whose physical meaning is transparent. Some features of the method are:

a) The nonperturbative wave function of the *B* meson is used under the assumption that all quarks lie on the mass shell. This gives agreement, first, with methods for obtaining the wave function from the Schrödinger equation and, second, with the diagrammatic approach.

b) It allows for the fact that in obtaining the differential decay width of a *B* meson it is preferable, in a certain sense, to integrate first over the transverse momentum $\mathbf{p}_\perp$ of the heavy quark and then over the variable x — the longitudinal momentum fraction in the infinite-momentum frame. This makes it possible to express the decay width of the *B* meson as a product of the decay width of a *b* quark and a weighting function (see Eq. (5)), previously introduced in a general form by Bjorken.[5]

c) The integration over x is performed not over constant limits from 0 to 1 but rather over limits which depend on the values of the kinematic variables y and z' (the notation is explained below). These limits ''collapse'' as the mass of the created hadronic system approaches the lowest hadronic threshold.

The differential inclusive semileptonic decay width with the formation of charmed hadronic states has the form[3]

$$d\Gamma^{e\nu}=\frac{G^2M_B^5}{(4\pi)^3}|V_{cb}|^2\frac{2|\mathbf{q}|}{M_B}\left\langle\frac{L^{e\nu}_{\alpha\beta}}{M_B^2}\right\rangle W^{\alpha\beta}dydz', \tag{1}$$

where M_B is the mass of the B meson; $z'=P'^2/M_B^2$, where P' is the total momentum of the final hadronic state; $y=q^2/M_B^2$, where $q=P-P'$ is the momentum transfer and P is the momentum of the B meson;

$$|\mathbf{q}|=\frac{M_B}{2}\sqrt{(1+y-z')^2-4y};\quad q_0=\frac{M_B}{2}(1+y-z')$$

in the rest frame of the B meson; $\langle L^{e\nu}_{\alpha\beta}\rangle=\frac{2}{3}(q_\alpha q_\beta-g_{\alpha\beta}q^2)$ is the leptonic tensor (the lepton masses are neglected); $W^{\alpha\beta}$ is the hadronic tensor

$$W^{\alpha\beta}=\int L^{\alpha\beta}(p_b,p_c)\,\delta((p_b-q)^2-m_c^2)f(x,\mathbf{p}_\perp^2)\frac{dx}{x}d\mathbf{p}_\perp^2, \tag{2}$$

where $L^{\alpha\beta}(p_b,p_c)=2(p_b^\alpha p_c^\beta+p_b^\beta p_c^\alpha-g^{\alpha\beta}(p_bp_c)-i\varepsilon^{\alpha\beta\gamma\delta}p_b^\gamma p_c^\delta)$; and, x and $\mathbf{p}_\perp$ are light-cone variables for the b quark

$$x=\frac{p_{b+}}{P_+}=\frac{p_b^0+p_b^3}{P^0+P^3},\quad \mathbf{p}_\perp=\mathbf{p}_b-\mathbf{n}_z(xP_z),$$

the z axis being oriented in the direction of the vector $\mathbf{q}$ in the rest frame: $\mathbf{n}_z=\mathbf{q}/|\mathbf{q}|$.

The distribution function $f(x,\mathbf{p}_\perp^2)$ is normalized according to the condition that the elastic form factor $F(0)=1$:

$$\int f(x,\mathbf{p}_\perp^2)dxd\mathbf{p}_\perp^2=1. \tag{3}$$

The contraction of the tensors is

$$\left\langle\frac{L^{e\nu}_{\alpha\beta}}{M_B^2}\right\rangle W^{\alpha\beta}=\frac{2}{3q_+M_B}[(m_b^2-m_c^2)^2+q^2(m_b^2+m_c^2)-2q^4]I_0, \tag{4}$$

where

$$I_0=I_0(q^2,q_0)=\int f(x,\mathbf{p}_{\perp_0}^2)dx;\quad \mathbf{p}_{\perp_0}^2=\mathbf{p}_{\perp_0}^2(x)=\mu^2\frac{xM_B}{q_+}-x^2M_B^2\frac{q_-}{q_+}-m_b^2;$$

$$q_\pm=q_0\pm|\mathbf{q}|;\quad \mu^2=m_b^2+q^2-m_c^2;$$

m_b and m_c are the masses of the b and c quarks. The function $\mathbf{p}_{\perp_0}^2(x)$ appears as the root of the argument of the delta function in Eq. (2).

Finally, the differential decay width is

$$\frac{d^2\Gamma^{e\nu}}{dq^2dq_0}=\frac{d\Gamma_0}{dq^2}F(q^2,q_0), \tag{5}$$

where

$$\frac{d\Gamma_0}{dq^2}=\frac{G^2m_b^5}{192\pi^3}|V_{cb}|^2\frac{4|\mathbf{q}_b|}{m_b^2}\left[(1-\rho)^2+\frac{q^2}{m_b^2}(1+\rho)-2\left(\frac{q^2}{m_b^2}\right)^2\right]$$

is the decay width of a free b quark,

$$|\mathbf{q}_b|=|\mathbf{q}_b|(q^2)=\frac{1}{2m_b}\sqrt{\mu^4-4m_b^2q^2},\quad \rho\equiv\frac{m_c^2}{m_b^2}.$$

The weighting function in our case has the form

$$F(q^2,q_0)=\frac{2m_b^2}{q_+}\frac{|\mathbf{q}|}{|\mathbf{q}_b|}\int f(x,\mathbf{p}_{\perp 0}^2)dx. \tag{6}$$

In Ref. 5 a sum rule is presented for the weighting functions in the limiting case of heavy b and c quarks:

$$\int F(q^2,q_0)dq_0=1, \tag{7}$$

which means that the decay width of the B meson equals the decay width of a b quark. The application of Eq. (7) to our case gives (passing to the limits $m_b\to M_B$, $m_c\to M'=\sqrt{P'^2}$, and simultaneously $m_b\to\infty$, $m_c\to\infty$) our normalization condition (3). This verifies that our approach meets the general requirements.

As stated above, the limits of the x integral in Eq. (4) depend on y and z' as dictated by the requirement $\mathbf{p}_{\perp 0}^2(x)>0$. It follows from this requirement that

$$x_1<x<x_2,\quad x_{1,2}=\frac{1}{2Mq_-}[\mu^2\mp\sqrt{\mu^4-4m_b^2q^2}].$$

The condition $x_1=x_2$, which means that the phase volume of the final quarks reduces to zero, gives the value $z'=z_1(y)$ for the lower limit with respect to z', i.e., the hadronic threshold.

From Eq. (5) it is easy to obtain an expression for the semileptonic width ratio

$$dBr=\frac{d\Gamma^{e\nu}}{\Gamma_{\text{tot}}}=\frac{1}{\beta}\frac{4}{3}\frac{|\mathbf{q}|}{q_+}[(\zeta_b^2-\zeta_c^2)^2+y(\zeta_b^2+\zeta_c^2)-2y^2]M_B^2I_0dydz', \tag{8}$$

where the total width

$$\Gamma_{\text{tot}}=\beta\frac{G^2M_B^5}{(4\pi)^3}|V_{cb}|^2=0.45\times10^{-3}\text{ eV},$$

and β is a factor whose value is close to one.[3]

Formula (8) was used to perform numerical calculations of the total semileptonic ratio (see Table I) for the decay of $B^{\pm}$ mesons for the following model wave functions:

I) Free b quark. This case corresponds to $f(x,\mathbf{p}_\perp^2)=\delta(x-m_b/M_B)\delta(\mathbf{p}_\perp^2)$ and $d\Gamma^{e\nu}/dq^2=d\Gamma_0^{e\nu}/dq^2$. The values of the quark masses were taken to be the same as in model III.

II) Distribution from Ref. 3:

TABLE I.

	Experiment	I	II	III	IV	V
$Br^{e\nu}$	$(10.4\pm 0.4)\%$	11.4%	10.6%	8.4%	9.5%	9.6%

$$f(x,\mathbf{p}_\perp^2)=A\frac{x}{1-x}\exp\left[-\lambda\left(\frac{1-x}{\zeta_0}+\frac{\zeta_0}{1-x}\right)\right]\exp[-\mathbf{p}_\perp^2/p_0^2(1-x)],$$

where $p_0=M_B m_{sp}/\lambda_0$, $\zeta_0=m_{sp}/M_B$, the parameter $\lambda_0=1$, and the quark masses are $m_b=4.8$ GeV, $m_c=1.4$ GeV, and $m_{sp}=0.3$ GeV.

III) The distribution function $f(x,\mathbf{p}_\perp^2)$ obtained by an appropriate transformation[6] from a solution $\Psi(k)$ of the relativistic Schrödinger equation,[7] where k is the magnitude of the relative momentum of the quarks in their center-of-mass frame, and $m_b=4.997$ GeV, $m_c=1.628$ GeV, and $m_{sp}=0.22$ GeV.

IV) The solution of the Schrödinger equation in the nonrelativistic approximation.[6] The masses are: $m_b=5.279$ GeV, $m_c=1.835$ GeV, and $m_{sp}=0.337$ GeV.

V) Approximation of the solution of the Schrödinger equation by a Gaussian distribution:[8] $\Psi(k)=(4\pi/\beta^2)^{3/4}\exp(-k^2/2\beta^2)$, where for a B meson $\beta=0.41$ GeV. The quark masses are $m_b=4.88$ GeV, $m_c=1.55$ GeV, and $m_{sp}=0.33$ GeV.

It can be concluded on the basis of the results obtained that the principle of global duality holds well in the case of semileptonic decays of B mesons for most of the models examined, i.e., the total integral over z' gives branching values which are close to the experimental values.

The integration over z' can be performed starting not at the lowest threshold but rather a some initial value z_1, as done in Ref. 3, thereby obtaining the probability of a transition into the so-called ''continuous spectrum'' $Br^{e\nu}(X')$, which when added with the probabilities of transitions to lower-lying single-particle hadronic states (i.e., D and D^*) should give the total probability. In the calculations the value $z_1=(2.15\ \text{GeV}/M_B)^2$ was used. The model II in this case gives $Br^{e\nu}(X')=2.9\%$, which when added with $Br^{e\nu}(D)=1.87\%$ and $Br^{e\nu}(D^*)=5.64\%$ (Ref. 3) gives the good value $Br^{e\nu}=10.41\%$. Similar figures are obtained for model III: $Br^{e\nu}(X')=4.4\%$, $Br^{e\nu}(D)=2.07\%$, and $Br^{e\nu}(D^*)=5.98\%$. These values give a somewhat higher value than the experimental value $Br^{e\nu}=12.45\%$.

I thank Professors K. A. Ter-Martirosyan and I. M. Narodetskiĭ for a discussion of the questions examined in this letter.

[a)]e-mail: kotkovsk@heron.itep.ru

[1]G. Altarelli, N. Cabbibo, G. Corbo *et al.*, Nucl. Phys. B **208**, 365 (1982).
[2]G. Altarelli and S. Petrarca, Phys. Lett. B **261**, 303 (1992); I. I. Bigi and N. G. Uraltsev, Phys. Lett. B **280**, 271 (1992); I. I. Bigi, N. G. Uraltsev, and A. I. Vainstein, Phys. Lett. B **283**, 430 (1992); I. I. Bigi, M. Shifman, N. G. Uraltsev *et al.*, Preprints TPI-MINN 93/12-T (1993) and TPI-MINN-94/14-T (1994); I. I. Bigi

and N. G. Uraltsev, Preprint CERN-TH 7020/93 (1993); I. I. Bigi, M. A. Shifman, and N. G. Uraltsev, Preprint CERN-TH 7129/93 (1993).
[3] K. A. Ter-Martirosyan, Preprint ITEP 33-93 (1993); V. L. Morgunov and K. A. Ter-Martirosyan, Yad. Fiz. **59**, No. 7 (1996).
[4] C. H. Jin, M. F. Palmer, and E. A. Paschos, Phys. Lett. B **329**, 364 (1994).
[5] J. D. Bjorken, I. Dunietz, and J. Taron, Nucl. Phys. B **371**, 111 (1992).
[6] I. M. Narodetskii, R. Ceuleener, and C. Semay, J. Phys. G **18**, 1901 (1992).
[7] S. Godfrey and N. Isgur, Phys. Rev. D **32**, 185 (1985).
[8] V. O. Galkin, A. Yu. Mishurov, and R. N. Faustov, Yad. Fiz. **55**, 2175 (1992) [Sov. J. Nucl. Phys. **55**, 1207 (1992)].

Translated by M. E. Alferieff

New possibilities for producing photon echoes from a homogeneous ensemble of atoms and with the use of a single light pulse

G. N. Nikolaev[a)]

Institute of Automation and Electrometry, Siberian Branch of the Russian Academy of Sciences, 630090 Novosibirsk, Russia

(Submitted 3 April 1997)
Pis'ma Zh. Éksp. Teor. Fiz. **65**, No. 10, 738–743 (25 May 1997)

In investigations of predicted new types of photon echoes — an echo from a homogeneous ensemble of atoms and an echo of a single light pulse — have established that the magnitude and form of these new types of photon echoes are completely determined by the type of optical transition and by the ''area'' and polarization of the exciting light pulses (and the form can be controlled by varying the magnetic field). It is also established that the echo amplitude decreases for both small (compared to 1) and large light-pulse areas, and the optimal areas for which the maximum echo is obtained have been found. Investigations show that such photon echoes can also appear under conditions when an ordinary photon echo is absent (in atomic or molecular gases at high pressure, in the far-IR region of the spectrum, from cooled trapped atoms or ions, and so on). © *1997 American Institute of Physics.* [S0021-3640(97)00310-1]

PACS numbers: 42.50.Md

1. The photon echo (PE) effect, which was predicted in Refs. 1 and 2, consists in the fact that the irradiation of a medium by two light pulses engenders a response in the form of a radiation pulse separated from the second exciting pulse by the same time interval as that between the two exciting pulses. This interval can be much longer than the decay time of the macroscopic polarization, which decays because of the rapid dephasing of individual radiators due to the difference of their characteristic frequencies. The second pulse serves to rephase the radiators, restoring the macroscopic polarization induced by the first pulse and thus giving rise to a photon echo.

Therefore the ordinary PE effect requires the presence of inhomogeneous line broadening. However, different forms of photon echoes are possible, even in the case of homogeneous broadening, if an external magnetic (electric) field is additionally imposed on the medium.[3,4] This letter reports the results of investigations of PEs from a homogeneous ensemble of atoms[5] and from a single light pulse[6] in the presence of a magnetic field.

2. Let the average optical frequency ω of the exciting pulses be in quasiresonance with the transition frequency ω_0 of the atoms (molecules) between the degenerate energy states l and u with total angular momenta J_l and J_u, respectively. When an atom is placed in a strong external quasistatic magnetic field **H**, the resonance frequencies of the transitions between different degenerate energy sublevels change by the amount[7]

$$\Delta(M_l,t)=\Omega_L(t)[g_l M_l - g_u(M_l+\sigma)], \tag{1}$$

where $\Omega_L(t)=e|\mathbf{H}(t)|/2mc$ is the Larmor frequency, g_k and M_k are the Landé factors and the projections of the total angular momentum of the lower ($k=l$) and upper ($k=u$) levels on the quantization axis z (oriented along the field **H**), e and m are the electron charge and mass, and c is the speed of light.

On account of the selection rules for the allowed dipole transition studied in the present letter, the quantity σ can assume the values 0 and ± 1. For certain distinguished polarizations of the light, σ can take on only one of these values: $\sigma=0$ for linear polarization along **H**, and $\sigma=+1$ or -1 for light propagating in a direction parallel to **H** and having right- or left-circular polarization, respectively. As one can see from expression (1), for such polarizations of the light the interaction with the light couples each lower magnetic sublevel M_l only with one upper sublevel $M_l+\sigma$. Therefore the problem of the interaction of light (with fixed polarizations) with a resonant atom with two quasidegenerate states in a magnetic field reduces (if one neglects the decay from the upper state into the lower state) to analysis of the interaction of light with a collection of two-level systems. Furthermore, as one can see from Eq. (1), the resonance frequencies are different for each such two-level system, differing by the value of M_l. In consequence, such a collection of two-level systems can be treated as an analog of an ensemble of two-level atoms with different frequencies, which therefore exhibits ''inhomogeneous line broadening.'' A characteristic feature of such an ''ensemble'' is that each two-level system differs not only in the resonance frequency but also in the magnitude of the transition dipole moment $d(M_l)$. The behavior of $d(M_l)$ depends on the type of optical transition ($J_u=J_l$ or $J_u=J_l\pm 1$) and the polarization of the light, and $d(M_l)$ can be expressed in terms of a Clebsch–Gordan coefficient:[7] $d(M_l)=\langle J_u||d||J_l\rangle \times(-1)^{J_l-M_l}\langle J_u M_u J_l - M_l|1\sigma\rangle/\sqrt{3}$. Here $\langle J_u||d||J_l\rangle$ is the reduced matrix element of the dipole moment for the transition $u-l$, and $\langle J_u M_u J_l - M_l|1\sigma\rangle$ is a Clebsch–Gordan coefficient.

3. On the basis of the analogy indicated above, it is easy to calculate the magnitude of the PE from such a homogeneous ensemble of quasidegenerate two-level atoms. To simplify the analysis, we shall confine our attention to short square light pulses separated by a time interval T and having durations T_1, $T_2 \ll \Delta(J_l,0)$. In this case the polarization $P(t)$ of the PE at time t after the first pulse can be represented in the form

$$P(t)=2N\ \mathrm{Re}[\mathscr{P}(t)\exp(i\omega t)], \tag{2}$$

$$\mathscr{P}(t)=-i2\sum_{M_l} d(M_l)f(M_l)\left[\frac{\sin(\theta_1(M_l)\sqrt{1+y^2(M_l)})}{\sqrt{1+y^2(M_l)}} - 2i\frac{y(M_l)\sin^2\left(\frac{\theta_1(M_l)}{2}\sqrt{1+y^2(M_l)}\right)}{1+y^2(M_l)}\right]S(M_l,t), \tag{3}$$

$$S(M_l,t)=\{\sin^2(\theta_2(M_l)\sqrt{1+\epsilon^2 y^2(M_l)}/2)/[1+\epsilon^2 y^2(M_l)]\}\exp[i(t-T_1-T_2 - 2T)\Omega(M_l)]. \tag{4}$$

In the expressions presented above, N is the number of atoms per unit volume, $f(M_l)$ is the population distribution over the sublevels of the lower level of the atoms before the interaction with the light, $y(M_l)=\Omega(M_l)/\Omega_{E_1}(M_l)$, $\Omega(M_l)=\omega_0-\omega+\Delta(M_l,0)\equiv\Omega_0+\Delta(M_l,0)$, $\Omega_{E_{1,2}}(M_l)=d(M_l)E_{1,2}/\hbar$, $\theta_{1,2}(M_l)=\Omega_{E_{1,2}}(M_l)T_{1,2}$, and $\epsilon=E_2/E_1$. These expressions were obtained on the assumption that noe ordinary inhomogeneous broadening is present.

To obtain general analytical expressions for a PE for arbitrary values of J_l and J_u, let us examine the case $J\gg 1$ (as the calculations show, these expressions differ from the exact ones by less than 15%, even for $J=3$). In this case the new variable $\mu\equiv M_l/J_l$ can be treated as a continuous variable, which enables the substitution $\Sigma_{M_l}(\ldots)\to J_l\int_{-1}^{1}(\ldots)d\mu$ in expression (3) and makes it possible to use the asymptotic expressions for the Clebsch–Gordan coefficients.[7]

As the calculations show, the behavior of the PE differs substantially for different types of transitions ($J_u=J_l$ or $J_u=J_l\pm 1$) and light polarizations. The computational results for a PE from a homogeneous ensemble of atoms are presented below for two cases. Both results are presented for conditions such that the frequency of the exciting light exactly equals the resonance frequency of the atoms in the absence of a magnetic field and the distribution of the atoms over the lower sublevels is uniform ($f(M_l)=1/(2J_l+1)$).

Let the PE be excited by linearly polarized light ($\sigma=0$) whose frequency is in resonance with the frequency of an atomic transition with $J_u=J_l$. In this case expression (3) for the polarization $\mathscr{P}(t)$ of the light in the continuous approximation indicated above assumes the form

$$\mathscr{P}(t)=i(d(J_l)/[2(1+y^2(J_l)\epsilon^2)\sqrt{(1+y^2(J_l))}])\sum_{s=\pm 1}[D(s\tau+\Theta_1,\Theta_2)-[y(J_l)/\sqrt{1+y^2(J_l)}](D(\tau,\Theta_1)-D(\tau+s\Theta_1,s\Theta_2))], \tag{5}$$

where $D(\tau,\theta)=j_1(\tau)-[j_1(\tau+\theta)-j_1(\tau-\theta)]/2$, $\tau\equiv(g_u-g_l)J_l\Omega_L(t-T_1-T_2-2T)$, $\Theta_1\equiv\theta_1\sqrt{1+y^2(J_l)}$, $\Theta_2\equiv\theta_2\sqrt{1+y^2(J_l)\epsilon^2}$, $\theta_{1,2}=\theta_{1,2}(J_l)$, and $j_1(x)\equiv\cos(x)/x-\sin(x)/x^2$ is a first-order spherical Bessel function.[8] The dependence of the intensity of the PE on θ_1 and τ in the case $\theta_2=\pi$ and $y(J_l)=\epsilon=1$ is displayed in Fig. 1a.

The PE obtained with the same polarization of the light but for the transition $J_u=J_l\pm 1$ behaves qualitatively differently. In this case expression (3) for the polarization $\mathscr{P}(t)$ with $\epsilon=\Omega(J_l)/\Omega_E(0)=1$ becomes

$$\mathscr{P}(t)=i2d(0)\sin(\theta_2/2)\sin(\theta_1/2)[\cos(\theta_1/2)F_1(\tau)+\sin(\theta_1/2)F_2(\tau)], \tag{6}$$

where $F_1(\tau)\equiv 16[3\tau\cos(\tau)+(\tau^2-3)\sin(\tau)]/\tau^5$ and $F_2(\tau)\equiv 16[\tau(\tau^2-15)\cos(\tau)-3(2\tau^2-5)\sin(\tau)]/\theta_{1,2}(0)$. The dependence of the intensity of the PE on θ_1 and τ in the case $\theta_2=\pi$ is displayed in Fig. 1b.

4. It turns out that external fields make it possible to obtain PEs of a completely new type — a photon echo of a single light pulse.[6,9] In the case of an ordinary photon echo the rephasing of the atomic oscillators after the first, $\pi/2$ light pulse is due to the subsequent irradiation of the ensemble of atoms by a second, π pulse. In our case this can be

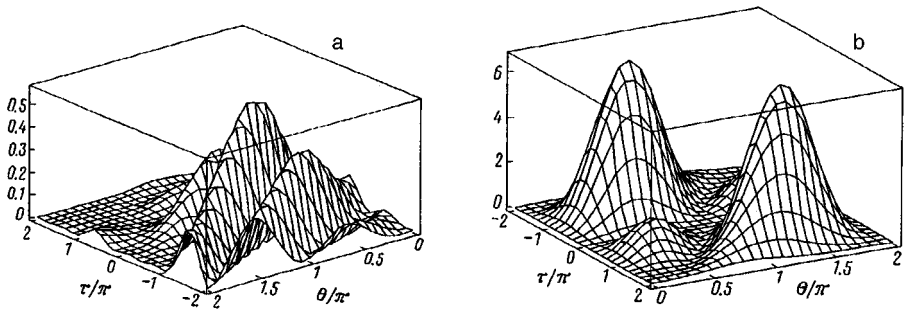

FIG. 1. Intensity of the photon echo (in arbitrary units, $\theta_2=\pi$, $\epsilon=1$) as a function of θ_1 and τ: a — Case of a transition with $J_u=J_l$ ($y(J_l)=1$); b — case of a transition with $J_u=J_l+1$ ($\Omega(J_l)/\Omega_E(0)=1$).

achieved without repeated irradiation by making a specific change in the value of the magnetic field. Indeed, after the atoms are irradiated with a light pulse, the induced macroscopic dipole moment decays as a result of the dephasing of individual oscillators with different frequencies according to Eq. (1). Since this frequency difference depends on **H**, rephasing of the macroscopic dipole moment can be achieved and therefore a PE can be obtained by changing the field (changing its sign) after the light pulse. The intensity of the photon echo in this case reaches a maximum at the time when the integral of the field over the time elapsed after the irradiation with the first pulse vanishes.

The polarization of such a single-pulse PE can be represented by the same relations (2) and (3) which describe a two-pulse PE. However, expression (4) for $S(M_l,t)$ must be replaced in this case by the following expression: $S(M_l,t)=(1/2)\exp(i\,[\Omega_0 t+\tilde{\psi}(M_l,t)])$, where $\tilde{\psi}(M_l,t)=\int_0^t\Delta(M_l,t')dt'$. Let this unusual PE be induced by a single linearly polarized light pulse whose frequency is in resonance with the frequency of the atomic transition with $J_u=J_l$. In this case the expression for the polarization $\mathscr{P}(t)$ of the light in the continuous approximation indicated above has the form

$$\mathscr{P}(t)=i(d(J_l)/\sqrt{1+y^2(J_l)})[j_1(\psi(t)+\Theta)-j_1(\psi(t)-\Theta)+2(y(J_l)/\sqrt{1+y^2(J_l)})D(\psi(t),\Theta)], \tag{7}$$

where $\Theta\equiv\theta\sqrt{1+y^2(J_l)}$ and $\psi(t)\equiv\tilde{\psi}(J_l,t)$. The dependence of the intensity of the PE on θ and ψ in the case $y(J_l)=1$ is displayed in Fig. 2a.

A PE obtained with the same light polarization but for the transition $J_u=J_l\pm1$ behaves qualitatively differently. In this case the expression for the polarization $\mathscr{P}(t)$ with $\Omega(J_l)/\Omega_E(0)=1$ is

$$\mathscr{P}(t)=2id(0)[\sin(\theta)j_1(\psi(t))/\psi(t)-(1-\cos(\theta))j_2(\psi(t))/\psi(t)], \tag{8}$$

where $\theta=\theta(0)$ and $j_2(x)\equiv-x(d/dx)[j_1(x)/x]$ is a second-order spherical Bessel function.[8] The dependence of the intensity of the PE on θ and ψ is shown in Fig. 2b.

5. This qualitative difference in the behavior of PE for different transitions can be interpreted as follows. As indicated above, transitions between different sublevels differ not only in their frequencies, as a result of the anomalous Zeeman effect, but also in the

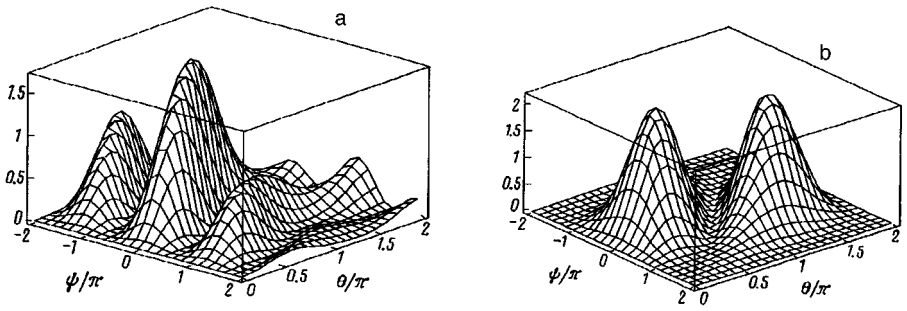

FIG. 2. Intensity of the photon echo of a single light pulse (in arbitrary units) as a function of ψ and θ. a — Case of a transition with $J_u = J_l$ ($y(J_l) = 1$); b — case of a transition with $J_u = J_l + 1$ ($\Omega(J_l)/\Omega_E(0) = 1$).

matrix elements of the dipole moments, which influence the strength of the interaction with the light. Therefore the Bloch vector for each transition is rotated through a different angle by the light pulse, the rotation for each transition occurring, in general, around different axes. As a result of this, the total macroscopic moment of the atoms immediately after the passage of the light pulse will also be different for different transitions. Figure 3 displays for the transitions under study a polar diagram of the initial distribution of the dimensionless dipole moment $(d_s(\mu) + id_q(\mu))/d$ after the passage of a light pulse. Here $d_s(\mu)$ is the in-phase component of the transition dipole moment with $M_l = \mu J_l$ and $d_q(\mu)$ is the quadrature component. The dipole moment d equals $d(J_l)$ for the case in Fig. 3a and $d(0)$ for the case in Fig. 3b. In the ordinary PE effect the dipole moments for all atoms after passage of the first, $\pi/2$ pulse are identical and are directed in the q direction (dashed line in Fig. 3a). The diagram in Fig. 3b is obviously closer to the classical case than the diagram in 3a. Therefore the form of the PE for the case in 3b is closer to that of an ordinary PE.

Since the form of the photon echo depends radically on the type of optical transition, this can be used to determine experimentally the characteristics of the atomic states which are coupled. The above-examined mechanism of the formation of the unusual photon echo extends the conditions under which the echo can appear: Such a PE can be

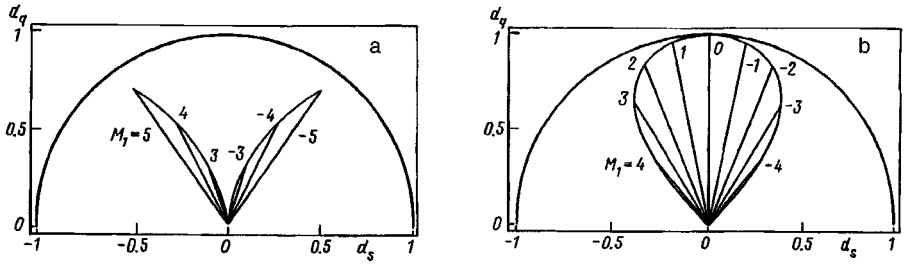

FIG. 3. Polar diagram of the initial (after the first light pulse) distribution of the complex dimensionless dipole moments of the atoms $(d_s(\mu) + id_q(\mu))/d$: a — Case of a transition with $J_u = J_l$; b — case of a transition with $J_u = J_l + 1$.

observed even in the case when homogeneous line broadening predominates. Specifically, a photon echo of this type is possible in atomic or molecular gases under high pressure, in the infrared and far-IR regions of the spectrum, as well as from cooled trapped atoms or ions.

[a)]e-mail: fractal@iaie.nsk.su

[1]U. Kh. Kopvillem and V. R. Nagibarov, Fiz. Met. Metalloved. **15**, 313 (1963).
[2]N. A. Kurnit, I. D. Abella, and S. R. Hartmann, Phys. Rev. Lett. **6**, 567 (1964).
[3]J. H. Eberly and V. M. Yermachenko, Laser Phys. **1**, 167 (1991).
[4]D. Yu. Kuznetsov, G. N. Nikolaev, and U. Kh. Kopvillem, Kratk. Soobshch. Fiz. **7**, 9 (1991).
[5]G. N. Nikolaev, *Proceedings of the Fifth European Quantum Electronics Conference*, IEEE, New Jersey, USA, 1994, p. 59.
[6]G. N. Nikolaev, *QLEO/QELS '95*, May 21–25, 1995, Baltimore, Maryland, USA, Optical Society of America, Washington D. C., 1995, p. 132.
[7]I. I. Sobel'man, *Introduction to the Theory of Atomic Spectra*, Pergamon Press, New York, 1972 [Russian original, Nauka, 1977].
[8]M. Abramowitz and I. Stegun (Eds.), *Handbook of Mathematical Functions*, Dover, New York, 1965 [Russian translation, Nauka, Moscow, 1972].
[9]G. N. Nikolaev, *Technical Digest of the 15th International Conference on Coherent and Nonlinear Optics*, June 27 – July 1, St. Petersburg, 1995, p. 248.

Translated by M. E. Alferieff

Quantum theory of cooling of atoms below the one-photon recoil energy by a pulsed field

A. V. Taĭchenachev,[a)] A. M. Tumaĭkin, and V. I. Yudin
Novosibirsk State University, 630090 Novosibirsk, Russia

(Submitted 24 April 1997)
Pis'ma Zh. Éksp. Teor. Fiz. **65**, No. 10, 744–749 (25 May 1997)

A completely quantum-analytical description of the cooling of atoms with angular momenta $j_g=1\rightarrow j_e=1$ by a pulsed $\sigma_+-\sigma_-$ field is developed. The problem of the change produced in the distribution of the atoms over the internal and translational degrees of freedom by a single field pulse is solved exactly with respect to recoil effects. Recurrence formulas for the distribution after the action of an arbitrary sequence of pulses are found in analytical form. It is shown that N field pulses result in the formation and narrowing of peaks at discrete points in momentum space as well as broadening of the envelope of these peaks. Explicit formulas are obtained for the peaks and envelopes in the case of a wide initial momentum distribution, and their asymptotic behavior for $N\gg 1$ is investigated. © *1997 American Institute of Physics.* [S0021-3640(97)00410-6]

PACS numbers: 32.80.Pj

1. The pioneering works listed as Ref. 1 initiated intensive investigations of the kinetic manifestations of coherent population trapping (CPT). Different schemes for laser cooling of atoms below the one-photon recoil energy by velocity-selective CPT in fields with spatial polarization and intensity gradients have now been developed theoretically[2] and partially implemented experimentally.[1,3] Recently, two groups proposed a new pulsed (Ramsey) cooling scheme,[4,5] which, as is evident from the experimental results[5] and quantum simulations,[4] makes it possible to obtain narrower structures in the velocity distribution of the atoms and within a shorter time than in the case of a continuously acting field. This letter develops a completely quantum-analytical description of the Ramsey cooling effect for the example of the transition $j_g=1\rightarrow j_e=1$ in a pulsed $\sigma_+-\sigma_-$ field. Our basic approximation is that in the dark state the lifetime of the atoms, limited by translational-motion effects, is much longer than the duration τ of the light pulse. In perturbation theory this condition can be expressed as the inequality $\gamma\tau(kv/\Omega)^2\ll 1$ (γ is the radiation width of the excited level, kv is the Doppler shift, and Ω is the Rabi frequency),[1,6] satisfaction of which implies that either the atoms are precooled or the laser field is quite strong. Furthermore, we shall assume that a stationary interaction regime is realized, i.e., $\gamma\tau\gg 1$ and $\gamma S\tau\gg 1$, where $S=\Omega^2/(\gamma^2/4+\delta^2)$ is the saturation parameter and δ is the detuning from resonance. Under these conditions, after the field pulse has acted, the density matrix of the atoms in the coordinate representation has the form

$$\hat{\rho}(z_1,z_2)=|\Psi_{NC}\rangle W(z_1,z_2)\langle\Psi_{NC}|, \tag{1}$$

where $|\Psi_{NC}\rangle$ is the dark state, i.e., the state which has not interacted with the field; this state is a coherent superposition of the wave functions of the magnetic sublevels of the ground state (see Eq. (9) below). The function W depends on the initial (before the application of the light pulse) density matrix and can be found exactly (without the use of an expansion in terms of the recoil momentum) by the method which we described in Ref. 6. The evolution of the density matrix of the atoms in the ground state during free propagation is determined by the kinetic energy operator $\hat{H}_K$. The solution of the problem of calculating the corresponding unitary operator $\exp(-i/\hbar\hat{H}_K T)$ is well known. Applying in the required order the transformations indicated above, the atomic distribution after the action of an arbitrary sequence of field pulses can be calculated. In the present letter this problem is solved for $j_g=1$. Recurrence formulas relating the distribution $W^{(N+1)}$ after the $N+1$-st pulse with the distribution $W^{(N)}$ after N pulses are found in analytical form. It is shown that a sequence of pulses results in the formation and narrowing of peaks at discrete points in momentum space as well as broadening of the envelope of these peaks. Explicit formulas are obtained for the peaks and envelope in a case of practical interest — a wide (compared with the photon pulse) initial momentum distribution — and their asymptotic behavior for $N\gg 1$ is studied. It is found that the width of the peaks decreases as $1/\sqrt{N}$ and the width of the envelope increases as $N^{1/4}$.

2. Let us examine the one-dimensional motion (along the z axis) of atoms whose ground and excited states form the optical transition $j_g=1\rightarrow j_e=1$ under a resonance interaction with a pulsed $\sigma_+-\sigma_-$ field. We assume that the field is monochromatic throughout the pulse duration τ:

$$\mathbf{E}(z,t)=\mathbf{e}(z)E_0\ \exp(-i\omega t)+\text{c.c.}, \tag{2}$$

$\mathbf{e}(z)=(\mathbf{e}_{-1}\ \exp(ikz)-\mathbf{e}_{+1}\ \exp(-ikz))/\sqrt{2}$, where $\mathbf{e}_{\pm 1}=\mp(\mathbf{e}_x\pm i\mathbf{e}_y)/\sqrt{2}$ are cyclic unit vectors. The field (2) is linearly polarized everywhere in space. At the point $z=0$ the polarization vector $\mathbf{e}(z)$ is oriented in the direction of the x axis, and at arbitrary z it is rotated by the angle kz. It is convenient in this connection (as shown in Ref. 6) to switch from the laboratory to a local coordinate system (CS) in which the x' axis rotates together with $\mathbf{e}(z)$. Specifically, the Hamiltonian of the free atom in the rotating CS is $\hat{H}_0=\hat{H}_K+\hbar\omega_0\hat{\Pi}_e$, where

$$\hat{H}_K=\frac{(\hat{p}-\hbar k\hat{J}_z)^2}{2M} \tag{3}$$

is the kinetic energy operator, which now depends on the angular momentum projection operator $\hat{J}_z$, ω_0 is the transition frequency, and

$$\hat{\Pi}_e=\sum_{\mu_e=-j_e}^{j_e}|j_e,\mu_e\rangle\langle j_e,\mu_e| \tag{4}$$

is the projection operator onto the excited state, and $|j_e,\mu_e\rangle$ are the wave functions of the degenerate magnetic sublevels. The Hamiltonian of the resonance interaction of atoms with the field (2) is spatially uniform in the local CS:

$$\hat{H}_{A-F}=\hbar\Omega\hat{V}\ \exp(-i\omega t)+\text{ h.c.}, \tag{5}$$

where Ω is the Rabi frequency (which, with no loss of generality, we shall assume to be positive) and the dimensionless operator $\hat{V}$ is determined in terms of the Clebsch–Gordan coefficients (the quantization axis is directed along the z axis): $\hat{V}=(\hat{V}_{-1}-\hat{V}_{+1})/\sqrt{2}$, where

$$\hat{V}_q=\sum_{\mu_e,\mu_g}|j_e,\mu_e\rangle\langle j_e(j_g,1),\mu_e|j_g,\mu_g;1,q\rangle\langle j_g,\mu_g|. \tag{6}$$

Separating in the standard manner the rapid time dependence at the frequency of the field, we obtain a quantum kinetic equation describing the evolution of the slow components of the density matrix in the rotating CS:

$$\begin{aligned}\frac{\partial}{\partial t}\hat{\rho}(z_1,z_2)=&-\frac{i}{\hbar}[\hat{H}_K,\hat{\rho}(z_1,z_2)]-i\Omega[(\hat{V}+\hat{V}^\dagger),\hat{\rho}(z_1,z_2)]-((\gamma/2-i\delta)\\&\times\hat{\Pi}_e\hat{\rho}(z_1,z_2)+(\gamma/2+i\delta)\hat{\rho}(z_1,z_2)\hat{\Pi}_e)+\gamma\\&\times\sum_{q=\pm1,0}Q_q(k(z_1-z_2))\hat{V}_q^\dagger\hat{\rho}(z_1,z_2)\hat{V}_q,\end{aligned} \tag{7}$$

where $\delta=\omega-\omega_0$ is the detuning from resonance and the functions $Q_q(k(z_1-z_2))$ describe the induced and spontaneous recoil effects:

$$\begin{aligned}Q_{\pm1}(kz)&=\frac{3}{2}\left(\frac{\sin(kz)}{kz}+\frac{\cos(kz)}{(kz)^2}-\frac{\sin(kz)}{(kz)^3}\right)\exp(\mp ikz);\\Q_0(kz)&=3\left(-\frac{\cos(kz)}{(kz)^2}+\frac{\sin(kz)}{(kz)^3}\right).\end{aligned} \tag{8}$$

Equation (7) exactly takes into account the quantum effects which are due both to momentum transfer from the field to the atoms in radiation processes and to the translational motion of the atoms.

3. If the lifetime of the atoms in the dark state is much longer than the pulse duration $\gamma\tau(kv/\Omega)^2\ll1$, then in solving the problem of the change produced in the atomic distribution by a light pulse, the first term on the right-hand side of Eq. (7) can be dropped. This gives a system of first-order ordinary differential equations $\partial\rho/\partial t=\mathscr{L}\rho$ whose stationary solution has the form (1). The dark state $|\Psi_{NC}\rangle$ is annihilated by the operator representing the interaction with the field, $\hat{H}_{A-F}|\Psi_{NC}\rangle=0$, and it is a superposition of the Zeeman wave functions of the ground state:

$$|\Psi_{NC}\rangle=\frac{1}{\sqrt{2}}(|j_g,-1\rangle-|j_g,1\rangle). \tag{9}$$

The function $W(z_1,z_2)$ is a two-point distribution function in the local CS and is determined by the momentum transfer in spontaneous and induced photon scattering processes during the action of the field and also by the initial (before the action of the light pulse) distribution over the internal and translational degrees of freedom. According to Ref. 6, the function W after the action of the field pulse can be written in the form

$$W(z_1,z_2|t+\tau)=\mathrm{Tr}\{\hat{C}(z_1-z_2)\hat{\rho}(z_1,z_2|t)\}, \tag{10}$$

where the matrix $\hat{C}(z_1-z_2)$ is the left eigenvector of the Liouville operator $\mathscr{L}$, corresponds to the zero eigenvalue ($C\mathscr{L}=0$), and satisfies the normalization condition $\langle\Psi_{NC}|\hat{C}(z)|\Psi_{NC}\rangle=1$. The explicit form of the matrix $\hat{C}$ for the transition $j_g=1\to j_e=1$ was found in Ref. 6 (Eq. (37)) and, for lack of space, is not reproduced here.

4. After the field is switched off, the atoms are in the ground state, so that their evolution during free propagation is determined by the kinetic energy operator (3):

$$\hat{\rho}(z_1,z_2|t+T)=\exp\left(-\frac{i}{\hbar}\hat{H}_K T\right)|\Psi_{NC}\rangle W(z_1,z_2|t)\langle\Psi_{NC}|\exp\left(\frac{i}{\hbar}\hat{H}_K T\right). \tag{11}$$

Combining Eqs. (11) and (10), we obtain a recurrence formula relating the distribution $W^{(N+1)}$ after the action of the $N+1$-st pulse with the distribution $W^{(N)}$ after the action of N pulses:

$$W^{(N+1)}(z)=W^{(N)}(z)+S(kz)(W^{(N)}(z+4\omega_r T/k)+W^{(N)}(z-4\omega_r T/k)-2W^{(N)}(z)),$$

$$S(kz)=\frac{2-Q_{-1}(kz)-Q_1(kz)}{8-2Q_{-1}(kz)-2Q_1(kz)}, \tag{12}$$

where $z=z_1-z_2$ and the dependence on z_1+z_2 is dropped (we are studying the spatially homogeneous case). We shall determine the initial conditions for the recurrence (12) as follows. Prior to the first pulse, let the atoms be in the ground state and possess an isotropic distribution over magnetic sublevels $\rho^{(0)}_{\mu_g,\nu_g}(z)=\delta_{\mu_g,\nu_g}F^{(0)}(z)/3$, where $F^{(0)}(z)$ is the initial distribution in the laboratory CS. After the first pulse we obtain

$$W^{(1)}(z)=\frac{2Q_0(kz)+4\cos(kz)}{4-Q_{-1}(kz)-Q_1(kz)}\frac{F^{(0)}(z)}{3}. \tag{13}$$

The formulas obtained solve the problem. Let us now examine separate cases.

5. The natural length scale in Eqs. (12) and (13) is the wavelength $\lambda=2\pi/k$ of the light. If the momentum variance in the initial distribution is much greater than the photon momentum, then the function $F^{(0)}(z)$ is nonzero in a small (compared with λ) neighborhood of $z=0$. In the same approximation, the distribution function after the action of N pulses consists of a regular system of peaks located at the points 0, $\pm 4\omega_r T/k$, $\pm 8\omega_r T/k$ . . . :

$$W^{(N)}(z)=\sum_l \phi_l^{(N)}\mathscr{E}^{(N)}(z-4\omega_r Tl/k), \tag{14}$$

where the functions $\mathscr{E}^{(N)}(0)=1$ are nonzero in a small neighborhood of $z=0$ and describe the change in the envelope at each step. The amplitudes $\phi_l^{(N)}$ of the peaks satisfy the recurrence formula

$$\phi_l^{(N+1)}=\phi_l^{(N)}+S(4\omega_r Tl)(\phi_{l-1}^{(N)}+\phi_{l+1}^{(N)}-2\phi_l^{(N)}) \tag{15}$$

with the initial condition $\phi_l^{(1)}=\delta_{l,0}$; $\mathscr{E}^{(N)}$ can be represented as a finite product

$$\mathscr{E}^{(N)}(z)=\prod_{i=1}^{N}(1-(kz)^2D^{(i)})F^{(0)}(z), \tag{16}$$

where the ''diffusion'' coefficient $D^{(1)}=11/30$, and $D^{(N>1)}=7(1-\phi_1^{(N)})/10$ depends on the amplitude.

The momentum distribution (Fourier transform with respect to the difference z) corresponding to Eq. (14) is a product $\widetilde{W}^{(N)}(p)=\Phi^{(N)}(p)\widetilde{\mathscr{E}}^{(N)}(p)$ of a periodic (with period $2\pi\hbar k/4\omega_r T$) and symmetric (relative to $p=0$) function

$$\Phi^{(N)}(p)=1+2\sum_{l=1}^{N-1}\cos(4\omega_r Tlp/(\hbar k))\phi_l^{(N)} \tag{17}$$

by a smooth envelope $\widetilde{\mathscr{E}}^{(N)}(p)$.

Within the periodicity interval $[-\pi\hbar k/(4\omega_r T),\ \pi\hbar k/(4\omega_r T)]$ the function (17) describes the formation of a maximum at the point where all harmonics interfere constructively, intensifying one another. As one can see from Eq. (15), the coefficients $\phi_l^{(N)}$ are real, symmetric ($\phi_l^{(N)}=\phi_{-l}^{(N)}$), and positive. Therefore the maximum lies at the point $p=0$. As the number N of pulses increases, the number of the harmonics in Eq. (17) and their amplitudes increase. Obviously, this increases the maximum of the function $\Phi^{(N)}(p)$ and decrease its width.

The observed distribution function in the laboratory CS is expressed in terms of $\widetilde{W}^{(N)}(p)$ by the formula $\widetilde{F}^{(N)}(p)=(\widetilde{W}^{(N)}(p+\hbar k)+\widetilde{W}^{(N)}(p-\hbar k))/2$, which describes the splitting of each peak in a local basis into two peaks in the laboratory basis.

6. Formulas (15) and (16) make it possible to analyze the asymptotic behavior of the solution for a large number of pulses. For $N\gg 1$ the dependence of the coefficients $\phi_l^{(N)}$ on N and l can be approximated by a smooth function $\phi(N,l)$, and Eqs. (15) can be approximated by a second-order differential equation $\partial\phi(N,l)/\partial N=a\partial^2\phi(N,l)/\partial l^2$ with the boundary condition $\phi(N,0)=1$ and the initial condition $\phi(0,l)=0$. Here we have neglected the dependence of the coefficient a on l, as is valid for $4\omega_r T\gg 1$. Therefore the problem reduces to the heat conduction equation for a semi-infinite rod whose end is kept at a constant temperature. The solution of this problem has the form $\phi(N,l)=1-\mathrm{erf}(l/(2\sqrt{aN}))$, where the ''thermal conductivity'' is $a=1/4$. Hence one can see that the width of the peaks in the momentum distribution decreases as $1/\sqrt{N}$. The ''diffusion'' coefficient $D^{(N)}$ in Eq. (16) for the envelope of the peaks also has the asymptote $1/\sqrt{N}$. Therefore the width of the envelope increases as $N^{1/4}$, and the relative fraction of atoms in one peak (the area of the peak) decreases as $N^{-1/4}$.

It is interesting to note that similar asymptotes for the width and area of the peaks are obtained in the problem of cooling by velocity-selective CPT in a stationary $\sigma_+-\sigma_-$ field,[7] if N is taken as the interaction time with the field.

7. In this letter we have developed a comparatively simple analytical description of the Ramsey cooling of atoms, assuming that the translational motion of the atoms can be completely neglected during the action of a light pulse. In the method presented the quantum effects due to recoil on absorption (emission) of photons and the free motion of the atoms in the absence of a field are taken into account exactly. We have shown that the

interaction of the atoms with light pulses under conditions of coherent population trapping (CPT) makes it possible to create a correlation between arbitrarily separated points z_1 and z_2. This is of fundamental importance for atomic optics and atomic interferometry.

[a)]e-mail: llf@admin.nsu.ru

[1] A. Aspect, E. Arimondo, R. Kaiser *et al.*, Phys. Rev. Lett. **61**, 826 (1988); A. Aspect, E. Arimondo, R. Kaiser *et al.*, J. Opt. Soc. Am. B **6**, 2112 (1989).
[2] M. A. Ol'shaniĭ, J. Phys. B **24**, L583 (1991); F. Mauri and E. Arimondo, Europhys. Lett. **16**, 717 (1994); C. Foot, H. Wu, E. Arimondo, and G. Morigi, J. Phys. (France) II **4**, 1913 (1994); P. Marte, R. Dum, R. Taïeb *et al.*, Phys. Rev. A **49**, 4826 (1994).
[3] J. Lawall, F. Bardou, B. Saubamea *et al.*, Phys. Rev. Lett. **73**, 1915 (1994); H. Stecher, H. Ritsch, P. Zoller, *et al.* Phys. Rev. A **55**, 545 (1997).
[4] H. Wu, E. Arimondo, and C. Foot, Quantum Semiclassic. Opt. **8**, 983 (1996).
[5] F. Sander, T. Devolder, T. Esslinger, and T. Hänsch, e-preprint physics/9611015 in xxx.lanl.gov.
[6] A. V. Taichenachev, A. M. Tumaikin, and V. I. Yudin, Laser Phys. **2**, 575 (1992).
[7] F. Bardou, J. P. Bouchard, O. Emile *et al.*, Phys. Rev. Lett. **72**, 203 (1994).

Translated by M. E. Alferieff

Properties of IR-active lattice vibrations in the vicinity of kinks in the Frenkel–Kontorova model

V. M. Burlakov and M. A. Moskalenko
Institute of Spectroscopy, Russian Academy of Sciences, 142092 Troitsk, Moscow Region, Russia

(Submitted 10 April 1997)
Pis'ma Zh. Éksp. Teor. Fiz. **65**, No. 10, 750–754 (25 May 1997)

The properties of infrared lattice vibrations in the presence of kinks in the Frenkel–Kontorova model are analyzed. Our results show that the vibration of particles involved in kink formation is very similar to that in a gap mode around a force-constant defect. We found that the IR phonon mode intensity possesses a universal dependence on a certain combination of system parameters and kink concentration. On the basis of these results a criterion is proposed for separating the regime of weakly interacting kinks in the system from the regime of a kink lattice.
 [S0021-3640(97)00510-0]

PACS numbers: 63.20.−e

A system of interacting particles in a sinusoidal external potential (the Frenkel–Kontorova (FK) model[1]) is widely used for description of a broad variety of physical phenomena, such as the statics and dynamics of incommensurate phases (see, e.g., Ref. 2), transport properties in quasi-one dimensional conductors (see Ref. 3 and references therein), diffusion of adatoms on a metal surface,[4] etc. The features of the FK model which are usually explored relate to its kink-like solitons. Properties of the kinks have been described in a number of publications.[5–10] The dynamics of the FK model has also been extensively studied, but mostly in relation to the kink lattice rather than to single kinks.[11–14] At the same time, it is not yet completely clear at what values of the system parameters can the single-kink effects still be important.

The aim of the present study is to investigate the influence of both a single kink and a kink lattice on the infrared-active phonon spectrum and to specify the range of model parameters in which its properties can be treated in terms of nearly independent kinks rather than in terms of the superstructure associated with the kink lattice.

The investigations were performed in two approaches: i) a molecular dynamics (MD) simulation was used for relaxation of the system to an equilibrium state according to the method proposed in Ref. 15, after which all the particles were subjected to a small, uniform, step-like displacement and the subsequent vibrations were analyzed by means of a Fourier transformation; ii) the eigenvector problem (EVP) was solved in the harmonic approximation to study the vibrational spectrum of the system. The kinks in this case were taken into account through expansion of the potential energy around particle equilibrium positions determined from the MD simulation.

Let us consider a chain of particles of mass m and charge e with nearest neighbor

interaction in the sinusoidal external potential $V(x) = -(V \cdot a^2/4\pi^2)\cos(2\pi x/a)$, where a is the period of the potential. In case of a harmonic interparticle potential the equation of motion for nth particle is

$$m\frac{\partial^2 U_n}{\partial t^2} + \gamma\frac{\partial U_n}{\partial t} + K_2(2U_n - U_{n-1} - U_{n+1}) + \frac{Va}{2\pi}\sin\left(2\pi\frac{U_n}{a}\right) = eE(t), \tag{1}$$

where γ is phenomenological damping and $E(t)$ is external electric field. Suppose that the time-dependent position U_n of the particle can be represented as $U_n = na + U_n^0 + \delta_n(t)$, where U_n^0 is quasistatic variable describing a shift of the equilibrium position of the particle with respect to the corresponding potential minimum, and $\delta_n(t)$ describes a vibration of the particle about the new equilibrium position U_n^0. Then with the substitutions $\delta_n(t) = \delta_n(\omega)\exp(i\omega t)$ and $E(t) = E_0 \exp(i\omega t)$, Eq. (1) can be split into two equations:

$$K_2(2U_n^0 - U_{n-1}^0 - U_{n+1}^0) + \frac{V}{2\pi}\sin(2\pi U_n^0) = 0, \tag{2}$$

$$\delta_n(\omega)[V\cos(2\pi U_n^0) - \omega^2 + i\omega\gamma] + K_2(2\delta_n(\omega) - \delta_{n-1}(\omega) - \delta_{n+1}(\omega)) = E_0, \tag{3}$$

here and below we have adopted the values $m = 1$, $e = 1$ and $a = 1$. If one disregards the trivial case $U_n^0 = 0$, Eq. (2) describes a quasistatic kink-like deformation of the chain (due to neglect of the dynamical term we restrict our analysis to standing kinks only), while Eq. (3) describes the particle vibration about the new equilibrium position. In the continuum limit Eq. (2) reduces to the sine-Gordon equation[16] with the single-kink solution[17] $U_n^0(i) = 2\pi^{-1}\tan^{-1}\{\exp[\pm 2(n-i)a/R_k]\}$, $R_k = 2\sqrt{K_2/V}$ can be regarded as the kink radius measured in units of a, and i is the kink position. Substituting this solution into Eq. (3), one can obtain the complex succeptibility $\chi(\omega) = E_0^{-1}\Sigma\,\delta_n(\omega)$, where the peaks in $\mathrm{Im}(\chi(\omega))$ correspond to resonances ω_r, and $\mathrm{Re}(\delta_n(\omega_r))$ corresponds to the suitably normalized eigenvector of the mode at ω_r.

It is well established that the presence of kinks (or domain walls) in case of a negligible Peierls–Nabarro potential barrier results in a zero-frequency peak (phason mode) in the optical conductivity spectrum $\sigma(\omega) = \omega\ \mathrm{Im}(\chi(\omega))$ (see Fig. 1) corresponding to translational motion of kinks. The high-frequency peaks in Fig. 1 correspond to phonons, the strongest one being related to the in-phase vibrations of particles inside potential wells. The particles involved in the kink formation obviously possess a higher vibrational amplitude at low frequencies, while, as is seen in Fig. 2, they are almost completely eliminated from the phonon-like normal mode (the strongest peak in Fig. 1). Also shown, by the dashed lines in Fig. 2, are the eigenvectors for the case of an external force-constant defect $\Delta V(i)$ at the particle site i, with the rest particles being situated inside the potential wells. The corresponding spectrum is also shown in Fig. 1. The strength of the defect is determined from the equation[18]

$$1 + \frac{\Delta V}{N}\sum\frac{1}{V + 4K_2 \cdot \sin^2\left(\frac{k}{2}\right)} = 0, \tag{4}$$

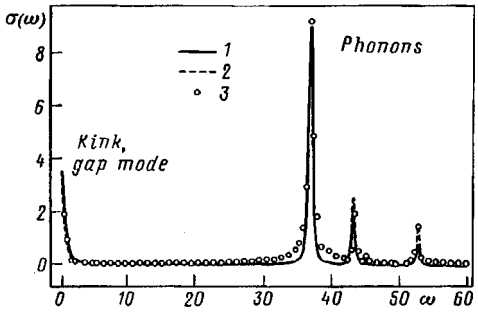

FIG. 1. Conductivity spectra of the Frenkel–Kontorova model containing 32 particles arranged over 31 potential wells: *1* is the spectrum calculated by Eq. (3) and (○) is that obtained by MD simulation for $K_2=4V$, $\sqrt{V}=36$ arb. units; *2* is the spectrum corresponding to a force-constant defect $\Delta V=-4.1231V$ (see text), for a position of the kink at the middle particle No.16.

which implies zero-frequency gap mode formation in the vicinity of the ith particle. As is shown in Fig. 2, the eigenvector of the gap mode is very close to that of the kink, while the eigenvectors of the phonon-like mode are nearly the same in both cases. Also the localization length S_{gap} of the gap mode (the half-width of the peak shown by the dashed line in Fig. 2) is equal to $R_k/\sqrt{2}$ over a wide range of R_k values (see the inset in Fig. 2). On this basis one may treat the system with kinks as a defect, or impurity crystal, taking for the description of its vibrational properties all the results already known. For instance, it is well understood that S_{gap} is basically determined by the separation $\sqrt{V}$ of the gap mode from the optical band and by the bandwidth $2\sqrt{K_2}$. One may argue therefore that the similarity between kink and the gap-mode eigenvectors and the kink eigenvector itself does not depend on the potential anharmonicity, provided that its influence on the above-mentioned parameters is small enough. Thus, we expect that our results will be applicable for a more realistic interparticle potential, too. From the analogy between the kinks and

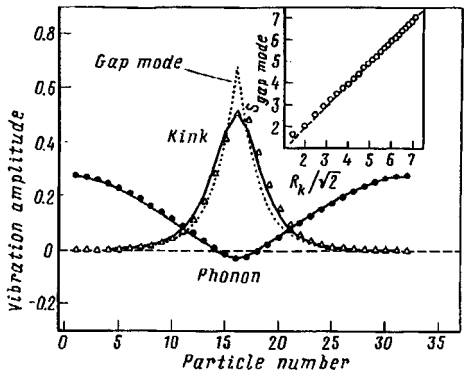

FIG. 2. The kink and the phonon (the strongest peak in Fig. 1) eigenvectors obtained in ways corresponding to those in Fig. 1. The symbols in the inset show the dependence of the gap-mode radius on the kink radius $R_k=2\sqrt{K_2/V}$.

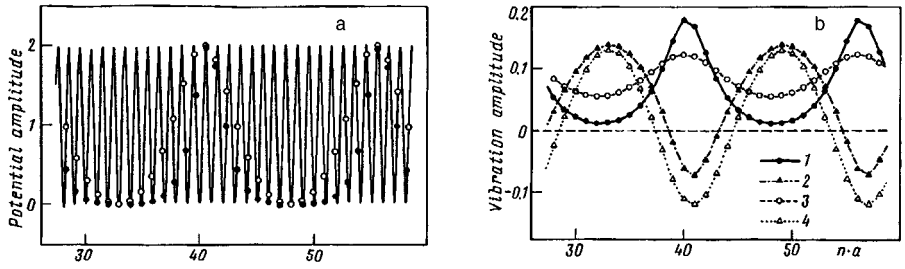

FIG. 3. a: The particle arrangement in the FK model of 128 particles (shown by symbols) in 120 potential wells (solid line). b: The eigenvectors of the kink-like (*1, 3*) and phonon-like (*2, 4*) modes. $K_2=4V$ (solid symbols) and $K_2=16V$ (open symbols), $\sqrt{V}=36$ arb. units.

defects it follows also that the IR phonon mode intensity will show a linear decrease versus n_k for low kink concentration. This indeed does take place in certain range of R_k values.

Although the N-kink solution of Eq. (2) is also available,[19] it is more convenient to approximate it by a sum of single-kink solutions. Our MD study of the ground state of a system consisting of 128 particles arranged in $128N_k$ potential wells with cyclic boundary conditions showed that even for $N_k \gg 1$ (N_k is the number of kinks) the kink lattice can be perfectly described as a sum of the single-kink solutions with $R_k \simeq 2\sqrt{K_2/V}$. Namely, for $N_k=8$ and $K_2=4V$ ($R_k^{\text{theor}}=4.0$) the value $R_k^{\text{exp}} \simeq 3.94$ has been obtained. Similar results have also been obtained for the case when the number of potential wells exceeds that of the particles. The dipole moment spectrum $I(\omega)=\text{Im}[\Sigma \delta_n(\omega)/E_0]$ has been both calculated from (3) with $U_n^0=\Sigma U_n^0(i)$ replaced by $R_k=R_k^{\text{exp}}$ and obtained from MD simulation via a fluctuation-dissipation approach for various values of $\eta=R_k n_k$ ($n_k=N_k/128$ is the kink concentration). The two approaches agree rather well even at very low frequencies, although the harmonic approximation obviously fails at $\omega=0$. Two examples of the particle arrangement and corresponding eigenvectors of the IR vibrations are presented in Fig. 3. The eigenvectors for $\eta=0.25$ look quite similar to those for the single kink or gap mode, while for $\eta=0.5$ even the particles which still occupy the potential wells and are not involved in the kink formation are strongly involved in the characteristic IR vibration (compare Figs. 3a and 3b). It should be pointed out that there is no noticeable difference between the commensurate and incommensurate cases (where the kink lattice period is or is not equal, respectively, to an integer number of the a) if the kink concentration is not too high. Otherwise the difference manifests itself in a small shift of the position of the zero-frequency peak shown in Fig. 1.

Let us now discuss the question of the intensity of the phonon peaks shown in Fig. 1 as a function of the parameter η. For this investigation we used the EVP approach, using Eq. (3) for various values of K_2/V and n_k. The results are presented in Fig. 4. The integrated intensity $I_\Sigma=\int I(\omega)d\omega$ of the phonon peaks reveals a universal dependence on the parameter $\eta=R_k n_k$. We found also that the eigenvectors of the strongest IR vibration obtained for different n_k but for the same η values, can be transformed to each other by proper scaling of a, i.e., they obey some sort of scaling invariance. Note, that the parameter η means the volume fraction (in the 1D case) occupied by the kinks, and the

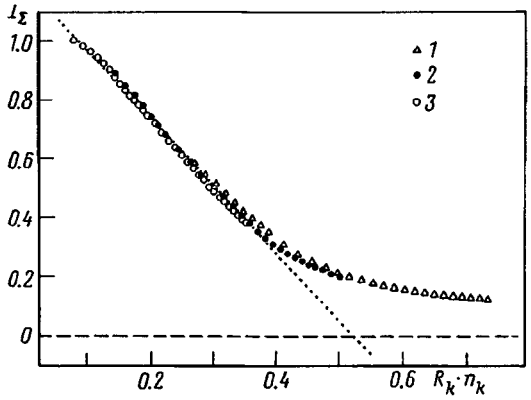

FIG. 4. Integrated intensity of the phonon-like modes versus $\eta = R_k n_k$ calculated according to Eq. (3) for FK model of 128 particles arranged in 112 wells (*1*) ($n_k = 1/8$), 120 wells (*2*) ($n_k = 1/16$), and 124 wells (*3*) ($n_k = 1/32$).

observed decrease in I_Σ at low η values can be interpreted as washing out of the high frequency density of states by gap modes associated with the kinks. At higher η, when the kinks form a real lattice and eventually a sinusoidal superstructure due to interaction with each other, the decrease in $I_\Sigma \propto \eta$ slows down because the real kink radius cannot exceed (in any case) one-half of the kink lattice period. Indeed, the linear decrease in I_Σ shown in Fig. 4 ends at a cutoff value of $\eta \simeq 0.4$, which implies that the aforementioned restriction on the kink radius is $R_k \leqslant 0.4 k_s^{-1}$ ($k_s = n_k$) where k_s is the kink lattice (or superstructure) wave vector measured in units of $\pi/2a$. Thus, we can display a range of parameters $k_s\sqrt{K_2/V} \leqslant 0.2$ in which it is possible (or even necessary) to describe the properties of the system in terms of independent kinks rather than in terms of some effective superstructure related to the kink lattice. Since the IR eigenvectors have been argued to be not very sensitive to anharmonicity, one might expect that this criterion will hold for more realistic potentials too.

Using the above criterion, one can tell whether the kinks are important for the description of some particular system. For example, in the charge-density-wave conductor $(TaSe_4)_2I$ the superstructure wave vector $k_s \simeq 0.085$ (Ref. 20), $\sqrt{V}$ can be associated with the giant IR peak frequency $\omega \sim 0.005$ eV (Ref. 21), and an upper bound on $\sqrt{K_2}$ can be estimated as $\sqrt{K_2} < \omega_p \simeq 1$ eV (Ref. 22), where ω_p is the plasma frequency. Thus one obtains $k_s\sqrt{K_2/V} < 1$, which implies that the kink effects can be important in this compound. A more detailed consideration of the vibrational properties of 1D conductors on the basis of the results obtained here will be given in a forthcoming paper.

In conclusion, we have shown that: i) the vibrational properties of kinks in the Frenkel–Kontorova model are very similar to those of the gap modes in a 1D crystal with force-constant defects; ii) on the basis of the universal dependence of the IR phonon mode intensity on certain combination of the system parameters it is possible to estimate whether single-kink effects are important for a particular physical system.

This work has been supported by Grant No. 96-18114 from the Russian Fund for Fundamental Research.

[1] Y. I. Frenkel and T. Kontorova, Zh. Éksp. Teor. Fiz. **8**, 1340 (1938).
[2] A. D. Novaco, Phys. Rev. B **22**, 1645 (1980).
[3] R. K. Dodd, J. C. Eilbeck, J. D. Gibbon, and H. C. Morris, *Solitons and Nonlinear Wave Equations*, Academic Press, London, 1984.
[4] A. G. Naumovets and Yu. S. Vedula, Surf. Sci. Rep. **4**, 365 (1984).
[5] G. Theodorou and T. M. Rice, Phys. Rev. B **18**, 2840 (1978).
[6] S. C. Ying, Phys. Rev. B **3**, 4160 (1971).
[7] J. A. Snyman and J. H. van der Merwe, Surf. Sci. **42**, 190 (1974).
[8] M. Peyerard and M. Remoissenet, Phys. Rev. B **26**, 2886 (1982).
[9] O. M. Braun, Yu. S. Kivshar, and I. I. Zelenskaya, Phys. Rev. B **41**, 7118 (1990).
[10] O. M. Braun, O. A. Chubykalo, Yu. S. Kivshar, and L. Vazquez, Phys. Rev. B **48**, 3734 (1993).
[11] C. de Lange and T. Janssen, J. Phys. C **14**, 5269 (1981).
[12] J. B. Sokoloff, Phys. Rev. B **25**, 5901 (1982).
[13] G. Radons, J. Keller, and T. Geisel, Z. Phys. B: Cond. Mat. **61**, 339 (1985).
[14] R. Currat and T. Janssen, Solid State Phys. **41**, 257 (1988).
[15] M. Peyrard and S. Aubry, J. Phys. C **18**, 4903 (1985).
[16] F. C. Frank and J. H. van der Merwe, Proc. R. Soc. London, Ser. A **198**, 205 (1949); **198**, 216 (1949); **200**, 125 (1949).
[17] R. K. Bullough and P. J. Caudrey (eds.), *Solitons*, Springer-Verlag, Berlin–Heidelberg–New York, 1980.
[18] A. S. Barker and A. J. Sievers, Rev. Mod. Phys. **47**, Suppl. N2, S1 (1975).
[19] P. J. Caudrey, J. C. Eilbeck, J. D. Gibbon, Nuovo Cimento **25**, 497 (1975).
[20] H. Fujishita, M. Sato, and S. Hoshino, Solid State Commun. **49**, 313 (1984).
[21] M. S. Shervin, Z. Zettl, and P. L. Richards, Phys. Rev. B **36**, 12 (1987).
[22] H. P. Geserich, G. Scheiber, F. Lévy *et al.*, Mol. Cryst. Liq. Cryst. **121**, 19 (1985).

Published in English in the original Russian journal. Edited by Steve Torstveit.

Quasiparticle dynamics and phase locking in a S–I–S multilayer Josephson junction

D. A. Ryndyk[a)]

Institute for Physics of Microstructures, Russian Academy of Sciences, 603600 GSP-105, Nizhny Novgorod, Russia

(Submitted 14 April 1997)
Pis'ma Zh. Éksp. Teor. Fiz. **65**, No. 10, 755–759 (25 May 1997)

New dynamical equations describing the Josephson effect and nonequilibrium quasiparticle distribution in a multilayer Josephson tunnel structure at $T \sim T_c$ are obtained, starting from the microscopic theory. It is shown that quasiparticle dynamics has a strong influence on the Josephson effect. Novel regimes with giant charge-imbalance oscillations are found. A new type of hysteresis on the current–voltage characteristic is predicted. © *1997 American Institute of Physics.* [S0021-3640(97)00610-5]

PACS numbers: 74.40.+k, 74.50.+r, 74.80.Dm

The dynamics of multilayer Josephson structures has been an important subject of theoretical and experimental investigations during the last few years. Recent experiments on the Josephson effect in artificial Nb–AlO_x–Nb stacked junctions[1] and natural layered high-T_c superconductors[2] show that these structures have a similar dynamic behavior and can be considered on a common basis.[3] In both of these systems the interaction between Josephson junctions and their mutual phase locking are of great interest and importance. A theory of magnetic coupling in layered structures is developed in Ref. 4 and applied to the problem of the synchronization of the Josephson vortex motion. But in the case of thin superconducting layers some other mechanisms are to be taken into account, especially disequilibrium (of the electron–hole imbalance type) of the quasiparticle distribution inside the superconducting layers, which can be essential if the layer thickness d_0 is smaller than the characteristic length of the disequilibrium relaxation l_E (see Refs. 5–7 and references therein). This criterion is obviously fulfilled for structures with layers of atomic thickness (high-$T_c$superconductors). For artificial structures $l_E = \sqrt{2\hbar DT/\pi\Delta^2}(1+4\Delta^2 t_\epsilon^2/\hbar^2)^{1/4}$, where $t_\epsilon^{-1} = 14g\hbar^{-1}\Theta_D^{-2}T^3\zeta(3)$is the inelastic electron–phonon scattering frequency, g is the electron–phonon interaction constant, Θ_D is the Debye temperature, $D = lv_F/3$ is the electron diffusion coefficient, Δ is the energy gap, l is the mean free path, and v_F is the Fermi velocity. A typical value of l_E is about 1 μm, so that $d_0 \ll l_E$ can be fulfilled at least at $T \sim T_c$, where $\Delta \to 0$ and $l_E \to \infty$. Disequilibrium results in the so-called quasiparticle coupling, which is well known in S–N–S junction systems.

In this paper we consider the Josephson effect with the quasipartical dynamics taken into account in a S–I–S multilayer Josephson tunnel structure with layer thickness $d_0 \ll l_E$, so that the superconductors are in a homogeneous nonequilibrium state. We also assume the dirty limit ($l \ll d_0$) and use the averaged-over-momentum-direction quasipar-

ticle distribution function n_ϵ^i introduced by Eliashberg,[8] which describes the quasielectron (at $\epsilon>0$) and quasihole (at $\epsilon<0$) energy distributions. In equilibrium $n_\epsilon^i = n_{-\epsilon}^i = n_\epsilon^{(0)} = 1/2(1-\tanh(|\epsilon|/2T))$.

The origin of the nonequilibrium Josephson effect in S–I–S systems is well established.[9–11] First of all, a tunnel junction is a source of disequilibrium in a nonstationary state due to injection of quasiparticles, so that n_ϵ^i changes in some way. We start from the kinetic equation for $n_\epsilon^i(t)$ in the ith layer, obtained for the present system by Bulyzhenkov and Ivlev,[9] Ivlev,[10] and Gulyan and Zharkov:[11]

$$u_\epsilon \frac{\partial n_\epsilon^i}{\partial t} = Q_{i-1\,i}(n_\epsilon) + Q_{i+1\,i}(n_\epsilon) + I^{\mathrm{e-ph}}(n_\epsilon^i), \tag{1}$$

$I^{\mathrm{e-ph}}(n_\epsilon)$ is the electron–phonon collision integral and $Q(n_\epsilon)$ is the tunnel source of disequilibrium, which for tunneling from S_i to S_j has the form (at $T\sim T_c$)

$$Q_{ij}(n_\epsilon) = \frac{\nu}{2}[(u_{\epsilon-v}+u_\epsilon u_{\epsilon-v})(\beta_{\epsilon-v}-\beta_\epsilon-\alpha_\epsilon) - (u_{\epsilon+v}-u_\epsilon u_{\epsilon+v})(\beta_{\epsilon+v}-\beta_\epsilon-\alpha_\epsilon)$$
$$+(1+u_\epsilon)\alpha_{\epsilon-v}+(1-u_\epsilon)\alpha_{\epsilon+v}]\,\mathrm{sign}\;\epsilon, \tag{2}$$

where we introduce the following notations in every layer:

$$\alpha_\epsilon = (n_\epsilon - n_{-\epsilon})\,\theta(\epsilon^2-\Delta^2)\,\mathrm{sign}\;\epsilon, \quad \beta_\epsilon = (n_\epsilon + n_{-\epsilon}-1)\,\theta(\epsilon^2-\Delta^2)\,\mathrm{sign}\;\epsilon, \quad v = \frac{\hbar}{2}\frac{d\varphi_{ij}}{dt},$$

$$u_\epsilon = \frac{|\epsilon|\,\theta(\epsilon^2-\Delta^2)}{\sqrt{\epsilon^2-\Delta^2}}, \quad v_\epsilon = \frac{\Delta\,\theta(\epsilon^2-\Delta^2)\,\mathrm{sign}\;\epsilon}{\sqrt{\epsilon^2-\Delta^2}}, \quad w_\epsilon = \frac{\Delta\,\theta(\Delta^2-\epsilon^2)}{\sqrt{\Delta^2-\epsilon^2}},$$

$\varphi_{ij} = \theta_j - \theta_i$ is the Josephson phase difference, all functions with shifted arguments relate to the superconductor S_i (the injector) and all functions with unshifted arguments relate to the superconductor S_j, $\nu = (4e^2N(0)RSd_0)^{-1}$ is the ''tunnel frequency,'' R is the normal resistivity of the tunnel junction, $V = Sd_0$ is the volume of the superconducting layer, and $N(0) = mp_F/2\pi^2$.

A nonequilibrium n_ϵ results in generation of a nonzero invariant potential

$$\Phi = \phi + (\hbar/2e)(\partial\theta/\partial t)$$

in the superconducting layers, where ϕ is the electrostatic potential and θ is the phase of superconducting condensate ($\Phi = 0$ in the equilibrium state). The shift of the chemical potential of the superconducting condensate from its equilibrium value is $\mu_s = e\Phi$ and is determined by

$$e\Phi = \int_\Delta^\infty (n_\epsilon - n_{-\epsilon})\,d\epsilon = \int_\Delta^\infty \alpha_\epsilon\,d\epsilon, \tag{3}$$

which is a direct consequence of the quasineutrality condition.[8] From (3) one can see that Φ is proportional to the difference in the electron and hole distribution functions and thus is associated with the so-called ''charge imbalance.'' Charge-imbalance phenomena have been extensively studied in tunnel structures, beginning from the pioneer work of Tinkham and Clarke.[12] Besides a large variety of static states (e.g., at a resistive N–S

boundary), weak charge imbalance oscillations are investigated in the form of linear waves (see the review in Ref. 6) and also in Josephson junctions.[13] In this work we show that new regimes with strong charge imbalance oscillations can arise in S–I–S multilayer structures.

Energy gap Δ is to be obtained from the nonequilibrium self-consistency equation

$$1=g\int_{\Delta}^{\Theta_D}\frac{1-n_{\epsilon}-n_{-\epsilon}}{(\epsilon^2-\Delta^2)^{1/2}}d\epsilon=g\int_{\Delta}^{\Theta_D}\frac{-\beta_{\epsilon}}{(\epsilon^2-\Delta^2)^{1/2}}d\epsilon. \tag{4}$$

The next important point to notice is that in the nonequilibrium regime an ordinary Josephson relation $(d\varphi/dt)=(2e/\hbar)V$ between the Josephson phase difference $\varphi_{ij}=\theta_j-\theta_i$ and voltage $V_{ij}=\phi_i-\phi_j$ is violated.[5–7] Instead, we have (from the definition of Φ)

$$\frac{d\varphi_{ij}}{dt}=\frac{2e}{\hbar}V_{ij}+\frac{2e}{\hbar}(\Phi_j-\Phi_i). \tag{5}$$

The tunnel current also is different from the equilibrium one. A correct expression in the case $d\varphi_{ij}/dt=\text{const}$ was obtained by Gulyan and Zharkov:[11]

$$\begin{aligned}
&J_{ij}=J_0\ \sin(\varphi_{ij})+J_1\ \cos(\varphi_{ij})+J_{qp},\\
&J_0=\frac{1}{2eR}\int_{-\infty}^{\infty}d\epsilon[v_{\epsilon}w_{\epsilon+v}\beta_{\epsilon}+v_{\epsilon+v}w_{\epsilon}\beta_{\epsilon+v}],\\
&J_1=\frac{1}{2eR}\int_{-\infty}^{\infty}d\epsilon v_{\epsilon}v_{\epsilon+v}(\beta_{\epsilon+v}-\beta_{\epsilon}),\\
&J_{qp}=\frac{1}{2eR}\int_{-\infty}^{\infty}d\epsilon\{u_{\epsilon}u_{\epsilon+v}(\beta_{\epsilon}-\beta_{\epsilon+v})+u_{\epsilon}\alpha_{\epsilon+v}-u_{\epsilon+v}\alpha_{\epsilon}\}.
\end{aligned} \tag{6}$$

From (5) and (6) we see that disequilibrium modifies the interlayer Josephson effect, and a self-consistent description is necessary. The kinetic equation (1), (2) together with the Josephson relation (5), current expression (6) and self-consistency equations (3), (4) are the full set of equations to be solved.

In this paper we consider temperatures $T\sim T_c$, at which an analytical solution of the kinetic equations may be obtained. It means that we use a small parameter $\Delta/T\ll 1$, and the results have the same accuracy. Furthermore, a typical Josephson voltage is of the order of $V_c=RI_c$, where $I_c=(\pi/2)(\Delta/eR)\tanh(\Delta/2T)$ (the Ambegaokar–Baratoff formula). At $T\sim T_c$ we obtain $V_c=(\pi/4)(\Delta/e)(\Delta/T)$ and thus $eV_c\ll\Delta\ll T$. Typical Josephson frequencies are $\hbar\omega_J\sim 2eV_c\ll\Delta$, T, and finally $e\Phi\ll\Delta$. As a result of these equalities, kinetic equation is linear and may be solved in adiabatic limit in which the microscopic expressions (6) and (2) for the current and tunnel source, respectively, are correct. We can also neglect change in the energy gap in this case.

At $\Delta\ll T$ the potential Φ is determined by the quasiparticle distribution over a large energy range $\epsilon\sim T$, and the anomalies at $\epsilon\sim\Delta$ can all be neglected. Taking $v\ll T$, we obtain from (2)

$$Q_{ij}(n_\epsilon)=\nu\left[-\frac{d\beta_\epsilon^{(0)}}{d\epsilon}v-\alpha_\epsilon^j+\alpha_\epsilon^i\right]\text{sign }\epsilon.$$

Because this tunnel source is antisymmetric over energies, we can take $\beta_\epsilon=\beta_\epsilon^{(0)}=-\tanh(\epsilon/2T)$ at $|\epsilon|>\Delta$ in the first approximation (and, accordingly, for equilibrium Δ), and for α_ϵ^i we obtain

$$\frac{d\alpha_\epsilon^i}{dt}=2\nu\left[\frac{v_{i-1\,i}-v_{ii+1}}{2T\cosh^2(\epsilon/2T)}-2\alpha_\epsilon^i+\alpha_\epsilon^{i-1}+\alpha_\epsilon^{i+1}\right]-\tau_q^{-1}\alpha_\epsilon^i, \tag{7}$$

where we take $I^{\text{e-ph}}(n_\epsilon)$ in the τ approximation, which is correct in our case, and $\tau_q=(4T/\pi\Delta)t_\epsilon$ is a well-known charge-imbalance relaxation time.

A solution of equation (7) in all layers simultaneously can be found in the well-known form[6]

$$\alpha_\epsilon^i=\frac{e\Phi_i(t)}{2T\cosh^2(\epsilon/2T)}. \tag{8}$$

One can see that the self-consistency equation (3) is satisfied automatically, and for $\Phi_i(t)$ we obtain

$$\tau_q\frac{d\Phi_i}{dt}+\Phi_i=\eta(V_{i-1\,i}-V_{ii+1}), \tag{9}$$

where

$$\eta=2\nu\tau_q=\frac{8T}{\pi\Delta}\nu t_\epsilon \tag{10}$$

is the parameter of disequilibrium. At $\eta=0$ we obtain $\Phi=0$ and the ordinary Josephson relations. In the same approximation we obtain from (6) the expression for the current

$$J_{ij}=J_c\sin(\varphi_{ij})+\frac{V_{ij}}{R}. \tag{11}$$

Taking (9), (11), and (5), we obtain the full set of dynamical equations for a S–I–S multilayer structure with nonequilibrium layers.

$$\frac{d\varphi_{ij}}{dt}=\frac{2e}{\hbar}V_{ij}+\frac{2e}{\hbar}(\Phi_j-\Phi_i),$$

$$J_{ij}=J_c\sin(\varphi_{ij})+\frac{V_{ij}}{R}+C\frac{dV_{ij}}{dt}=J(t), \tag{12}$$

$$\tau_q\frac{d\Phi_i}{dt}+\Phi_i=\eta(V_{i-1\,i}-V_{ii+1}),\quad V(t)=\sum_i V_{ii+1}.$$

Here the displacement current CdV/dt associated with the junction capacitance C is added as in the usual tunnel theory, and $J(t)$ and $V(t)$ are the external current and voltage. This set of equations describes the quasiparticle interaction between Josephson junctions. At $\eta=0$ this system describes noninteracting junctions with independent

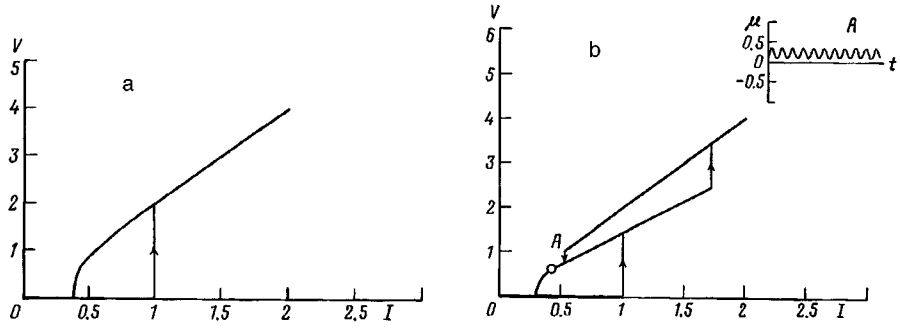

FIG. 1. Current–voltage characteristics of a S–I–S′–I–S Josephson structure at small coupling (a) and large coupling (b) between junctions.

phases $\varphi_{ij}(t)$. In the static limit our equations coincide with the equations obtained by Ivlev.[10] In the case of zero capacitance ($C=0$) they are similar to the system obtained by Artemenko and Volkov for S–N–S like structures.[6] One sees that at finite η a trivial solution $\varphi_{ij}=\varphi(t)$, $\mu=0$ always exists. But we find that this solution can be unstable (due to parametric instability of the charge imbalance), and a strong $\Phi\sim V$ arises in this case.

Below we consider (as an example) a simple S–I–S′–I–S Josephson tunnel structure with equilibrium banks (S) and a thin middle layer (S′) in the fixed-current limit, and in dimensionless form we obtain

$$\beta\frac{d^2\varphi_1}{d\tau^2}+\frac{d\varphi_1}{d\tau}+\sin(\varphi_1)-\mu-\beta\frac{d\mu}{d\tau}=j,$$

$$\beta\frac{d^2\varphi_2}{d\tau^2}+\frac{d\varphi_2}{d\tau}+\sin(\varphi_2)+\mu+\beta\frac{d\mu}{d\tau}=j,$$

$$\alpha\frac{d\mu}{d\tau}+\mu=\tilde{\eta}\left(\frac{d\varphi_1}{d\tau}-\frac{d\varphi_2}{d\tau}\right), \tag{13}$$

$$\beta=\frac{2eJ_cR^2C}{\hbar},\quad \alpha=\frac{\tau_q\omega_c}{1+2\eta},\quad \tilde{\eta}=\frac{\eta}{1+2\eta},$$

$$\mu(t)=\frac{2e}{\hbar\omega_c}\Phi(t),\quad \omega_c=\frac{2eRJ_c}{\hbar},\quad \tau=\omega_c t.$$

The current–voltage characteristics of a large-β junction at various coupling parameters η ($\alpha=0.01$, $\beta=10$, $\tilde{\eta}=0.05, 0.3$) are shown in Fig. 1, and the corresponding $\mu(t)$ dynamics is shown at one selected point. We see that at small coupling ($\tilde{\eta}=0.05$, Fig. 1a) the current–voltage characteristic is the same as for two independent junctions, but the junction phases are locked due to the quasiparticle interaction. At large coupling ($\tilde{\eta}=0.3$, Fig. 1b) the ''charge-imbalance'' regime at low currents gives way to the phase-locked regime at high currents, and novel type of hysteresis takes place.

Finally, we have shown that the dynamics of S–I–S multilayer Josephson structures is drastically altered by quasiparticle effects in the case of strong coupling.

This work is supported by the Russian Fund for Fundamental Research, Grant 97-02-16928. The author thanks Prof. A. A. Andronov, Dr. V. V. Kurin, and Dr. A. S. Mel'nikov for helpful and stimulating discussions.

[a)]e-mail: ryn@ipm.sci-nnov.ru

---

[1] H. Kohlstedt, G. Hallmanns, I. P. Nevirkovets *et al.*, *IEEE Trans. Appl. Supercond.* **AS-3**, 2117 (1993); I. P. Nevirkovets, H. Kohlstedt, G. Hallmanns, and C. Heiden, Supercond. Sci. Technol. **6**, 146 (1993); A. V. Ustinov, H. Kohlstedt, M. Cirillo *et al.*, Phys. Rev. B **48**, 10614 (1993).
[2] R. Kleiner and P. Muller, Phys. Rev. B **49**, 1327 (1994).
[3] R. Kleiner, P. Muller, H. Kohlstedt *et al.*, Phys. Rev. B **50**, 3942 (1994).
[4] S. Sakai, P. Bodin, and N. F. Pedersen, J. Appl. Phys. **73**, 2411 (1993).
[5] D. N. Langenberg and A. I. Larkin (eds.), *Nonequilibrium Superconductivity*, Vol. 12 of Modern Problems in Condensed Matter Science, North-Holland, Amsterdam, 1986.
[6] S. N. Artemenko and A. F. Volkov, Usp. Fiz. Nauk **128**, 3 (1979) [Sov. Phys. Usp. **22**, 295 (1979)].
[7] A. M. Gulyan and G. F. Zharkov, *Superconductors in External Fields (Nonequilibrium Phenomena)* [in Russian], Nauka, Moscow, 1990.
[8] G. M. Eliashberg, Zh. Éksp. Teor. Fiz. **61**, 1254 (1971) [Sov. Phys. JETP **34**, 668 (1972)].
[9] I. E. Bulyzhenkov and B. I. Ivlev, Zh. Éksp. Teor. Fiz. **74**, 224 (1978) [Sov. Phys. JETP **47**, 115 (1978)].
[10] B. I. Ivlev, Zh. Éksp. Teor. Fiz. **75**, 1771 (1978) [Sov. Phys. JETP **48**, 893 (1978)].
[11] A. M. Gulian and G. F. Zharkov, Zh. Éksp. Teor. Fiz. **89**, 156 (1985) [Sov. Phys. JETP **62**, 89 (1985)].
[12] M. Tinkham and J. Clarke, Phys. Rev. Lett. **28**, 1366 (1972).
[13] A. M. Gulian and G. F. Zharkov, Phys. Lett. A **103**, 283 (1984).

Published in English in the original Russian journal. Edited by Steve Torstveit.

Solitary flexural waves on a supersonic domain wall in yttrium orthoferrite

M. V. Chetkin, Yu. N. Kurbatova, and V. N. Filatov
M. V. Lomonosov Moscow State University, 119899 Moscow, Russia

(Submitted 15 April 1997)
Pis'ma Zh. Éksp. Teor. Fiz. **65**, No. 10, 760–765 (25 May 1997)

Solitary flexural waves on a supersonic domain wall in yttrium orthoferrite are observed and investigated. These waves have a sharp leading edge and a protracted trailing edge, reminiscent of the waves accompanying moving vertical Bloch lines in iron garnet films. The total velocity of the solitary flexural waves in yttrium orthoferrites for all observed amplitudes equals the maximum velocity of the domain walls. Two solitary waves with identical amplitudes colliding head-on are annihilated. The waves possess topological charges, and they move and form dynamic profiles under the influence of gyroscopic forces. [S0021-3640(97)00710-X]

PACS numbers: 75.50.Gg, 75.70.Kw

The dynamics and collisions of topological magnetic solitons — vertical Bloch lines (VBLs) — in iron garnet films have now been investigated in detail both experimentally and theoretically. In those investigations the solitary flexural waves arising under the influence of gyroscopic forces accompanying moving VBLs are recorded. This technique employs the Faraday effect and double- and triple-exposure high-speed photography in real-time.[1] Static VBLs are also recorded by the method of dark-field anisotropic diffraction of light.[2]

The existence of VBLs in iron garnets is connected with the fact that the magnetic moments are able to rotate not only in the plane of the domain wall but also in a plane perpendicular to wall. As a rule, the antiferromagnetism vectors **l** of orthoferrites can rotate in the *ac* or the *ab* plane. In the first case, the weak ferromagnetism vector also rotates in the same plane.[3] Until recently, VBLs had not been observed in orthoferrites, neither in statics nor dynamics. In Ref. 4 solitary flexural waves — large-amplitude kinks on domain walls (DWs) — moving with the speed of sound were observed in yttrium orthoferrite. This letter reports the results of an experimental investigation of the motion and collisions of small-amplitude solitary waves on a DW in yttrium orthoferrite that could be interpreted as the observation of dynamic VBLs moving with supersonic velocities on DWs in yttrium orthoferrite. The observation of small-amplitude kinks on supersonic DWs in yttrium orthoferrite was reported in Ref. 5. They were observed for only 4 ns. Their appearance was quite accidental. Their lifetimes and collision times were not investigated. In the present work we studied the dynamics of domain walls in thin (several tens of microns thick) yttrium orthoferrite slabs cut out perpendicular to the optic axis, by double-exposure high-speed photography using 0.25 ns light pulses. The light pulse was obtained by means of a nitrogen laser and a dye laser amplifier pumped by a

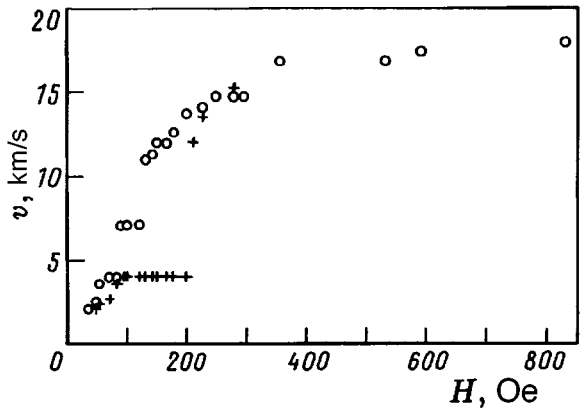

FIG. 1. Velocity of Néel (+) and Bloch (○) domain walls versus the magnetic field in a 30 μm thick $YFeO_3$ slab, cut perpendicular to the optic axis.

transverse discharge. We used this setup before to investigate the dynamics of DWs in orthoferrites, but in the present work we made a number of improvements in it. Specifically, a vitrified glass plate with a small opening was used in the spark gap of the transverse-discharge laser. The opening stabilized the triggering time of the laser and the long-term operation of the laser. A single Néel-type DW, oriented perpendicular to the surface of the sample, was established by means of a gradient magnetic field, oriented perpendicular to the surface of the sample, with grad $H=800$ Oe/cm. This wall was oriented perpendicular to the a axis of the slab. The magnetic moments in the domains on different sides of the wall lay in a plane perpendicular to the a axis, at angles of $\pm 40°$ to the plane of the sample. As usual,[6] the DW was set in motion by a pulsed field produced by two coils (each having an inner diameter of 1.5 mm) glued on the surface of the sample. The dependence of the velocity of DWs in such a slab for different orientations of the walls in the plane of the slab is displayed in Fig. 1. For a purely Néel DW, the region where the velocity of the wall is constant and equal to the velocity of transverse sound extends over 100 Oe. This is a very wide region, and its width could be due to the comparatively small thickness of the experimental sample (in this case 30 μm). The constant-velocity region gradually decreases in width as the DW is rotated in the plane of the sample, and, in accordance with the earlier experimental data and the prediction of the theory in Ref. 6, for a Bloch DW, oriented parallel to the a axis, it practically vanishes. Here a region in which the velocity of the DW is constant and equal to the velocity of transverse [*sic*] sound becomes appreciable. One or two separate wires 20 μm in diameter were glued on the same sample perpendicular to the static position of the Néel DW with the largest constant-velocity region for the purpose of passing a current producing a local decelerating magnetic fields for a brief time (several tens of nanoseconds). This current was applied after the entire DW had acquired a definite velocity in response to the pulsed current in the coils advancing the DW. A theory of the width of the region of constant velocity equal to the velocity of transverse sound for a Néel DW in orthoferrite was examined in Ref. 7, but the finite width of the sample, which influences the width of the region of constant velocity of the DW near the velocity of sound, was neglected. As

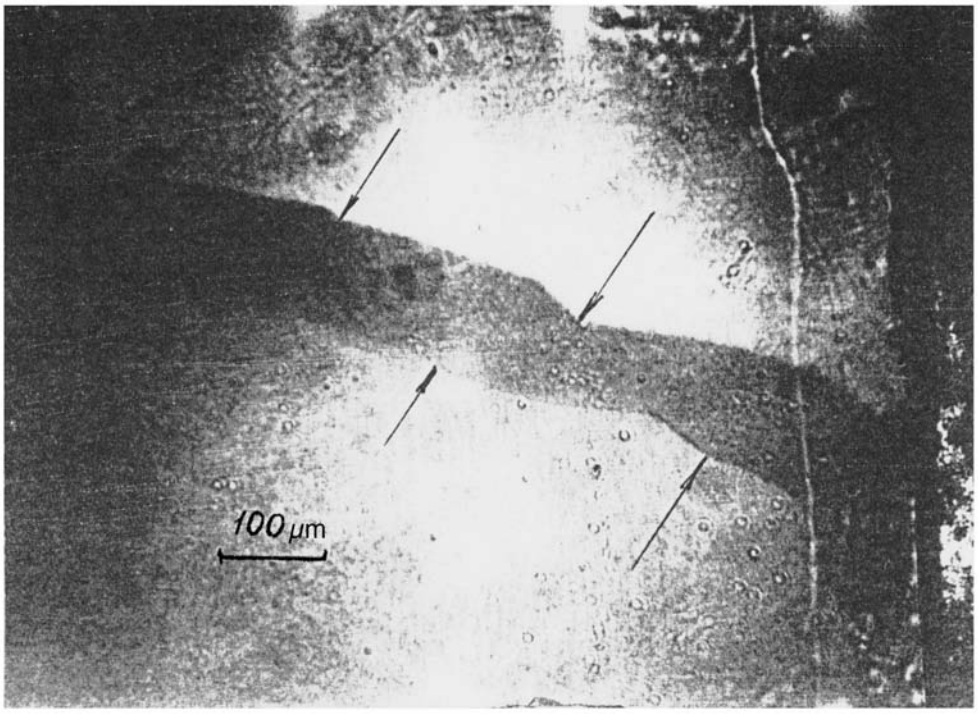

FIG. 2. Double-exposure high-speed photograph of solitary flexural waves on a moving domain wall in yttrium orthoferrite. The wall moves from bottom to top; the solitary waves move from right to left. The delay time $\Delta t = 9$ ns. The arrows mark the positions of the solitary waves.

one can see from Fig. 1, the transition of a Néel DW moving with the velocity of transverse sound to a supersonic velocity occurred very sharply in our experiment. Then, after a decelerating pulse was applied to the separate wires, solitary flexural waves with sharp leading and protracted trailing edges, lagging completely behind the DW and moving from right to left along the wall, were clearly observed on the nearly rectilinear sections of the DW, which were moving with a velocity of 12 km/s from bottom to top. The dark strip in Fig. 2 represents the region traversed by the DW in the time between two light pulses. The velocities of flexural waves with two different amplitudes along the DW, which are determined from the double-exposure high-speed photographs, were equal to 16 km/s. The profile of these solitary flexural waves remained unchanged throughout the entire experimentally accessible observation time, right up to 50–60 ns. Solitary flexural waves, produced by a pulsed current in each of the two separate wires and moving in opposite directions, were observed. The interval of velocities of the entire DW where these solitary flexural waves could be observed was very narrow, 200 m/s. At lower and higher velocities of the DW, solitary flexural waves moving along the DW did not arise and were not observed. Figure 3 displays a double-exposure high-speed photograph of a moving DW. The time delay between the two light pulses equals 9 ns. A solitary flexural wave travels along the DW from left to right. In Fig. 2 the solitary

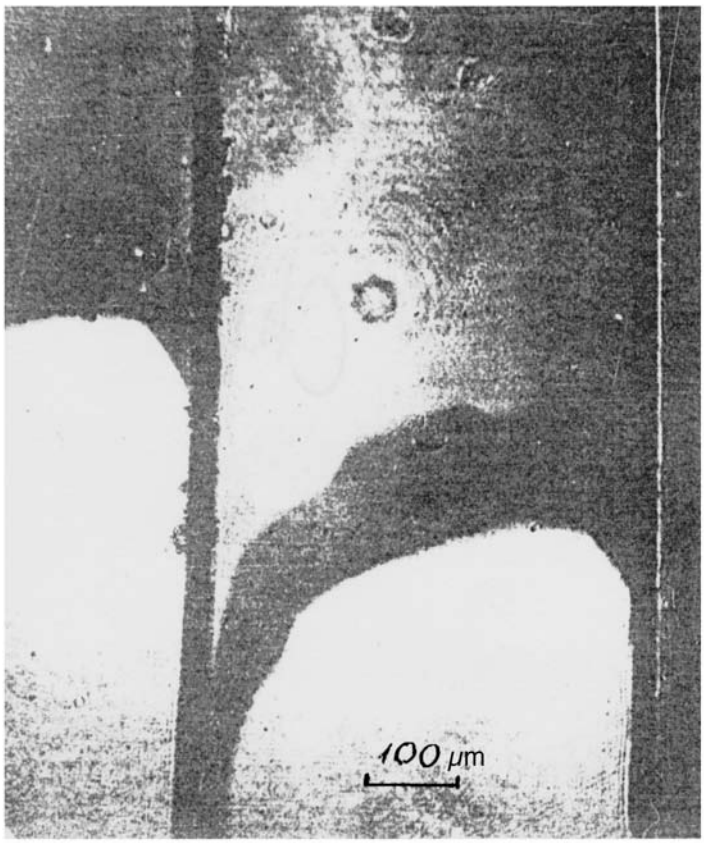

FIG. 3. Same as Fig. 2, for a solitary wave moving from left to right.

conductor is almost invisible; it was glued close to the coils. In Fig. 3 two conductors can be seen to intersect the DW; each conductor could produce a pair of solitary flexural waves moving in opposite directions. In our experiments their velocities along the DW were identical in absolute magnitude. Hence it can be concluded that small-amplitude kinks move under the influence of a gyroscopic force which is proportional to the velocity of the DW. In orthoferrites this velocity is very high and allows motion of kinks with all observed amplitudes and a total velocity of 20 km/s. The velocities of the DWs are much lower in the case of iron garnets, so that the velocities of the waves accompanying VBLs have been linked to their topological charges and, in consequence, with their amplitudes as well. This is why the situation in iron garnets is different from that in yttrium orthoferrite. The maximum velocity of a DW in orthoferrites is 20 km/s and equals the velocity of spin waves on the linear section of their dispersion relation. All of the solitary flexural waves that we observed experimentally in yttrium orthoferrite moved with a velocity of 16 km/s along the DW, regardless of their amplitude. The velocity U of the solitary waves, the velocity V of the DW, and the maximum velocity c were related by the relation

$$U^2 + V^2 = c^2. \quad (1)$$

Such a relation for low-amplitude disturbances on a one-dimensional orthoferrite wall has been obtained theoretically from the linearized equation of motion.[8] The result (1) was obtained experimentally and pertains to easily observable amplitudes of the nonlinear solitary waves. It means that the leading edge of a solitary wave is part of a DW whose velocity cannot exceed a maximum velocity equal to c. Therefore a similarity exists between the dynamic profiles of solitary flexural waves on supersonic DWs in yttrium orthoferrite and the analogous profiles in iron garnet films, where they undoubtedly accompany vertical Bloch lines. It can be concluded from this similarity that VBL-type topological formations arise even on supersonic DWs in orthoferrite. This result is confirmed by direct experiments on head-on collisions of two solitary flexural waves with the same amplitudes and moving along a DW in the experimental orthoferrite slab. In Fig. 4a, under illumination by the first light pulse, these waves are 220 μm apart. Five nanoseconds later they have almost completely annihilated one another. Complete annihilation is seen in Fig. 4b. The dynamics and mechanism of appearance of topological magnetic solitons on DWs in orthoferrite have not yet been studied theoretically. The surface of the orthoferrite slab, where the spin-reorientation field should be weaker than in a bulk sample,[9,10] could play a large role in the appearance of solitary flexural waves and, possibly, the VBL-type topological formations which are associated with them. True, in Kerr-effect magnetooptic investigations, where the Kerr effect apparently occurs at a depth of several tens of angstroms, the effect of the surface was observed only near the spin-orientation temperature. In Ref. 11, no effect was found in $YFeO_3$ in ordinary laboratory magnetic fields. In Ref. 9 it is shown that a Néel DW in an antiferromagnet remains stable with a pair of neighboring spins emerging into a plane perpendicular to the wall. In a high transverse magnetic field, this emergence of the spins can happen in two mutually perpendicular planes. A similar situation possible occurs in weak ferromagnets as well, which in principle could result in the formation of VBLs. It seems to us that the instability of a supersonic domain wall in yttrium orthoferrite, manifested, specifically, as a change in the orientation of the plane of the DW, and the absence of hysteresis in the magnetic-field dependence of the velocity V of the DW in the supersonic range[6] could give rise to topological formations on a supersonic DW in yttrium orthoferrite. It is of interest to perform numerical calculations of the formation and dynamics of solitary flexural waves taking account of the rotation of the magnetic moments of the DW in a plane perpendicular to the ac plane. Model calculations can be performed for small damping parameters, which are characteristic of yttrium orthoferrite. These calculations will shed light on the character of the profiles and amplitude of solitary flexural waves, their dependence on the velocity of the DW, and so on. However, the general mechanism of the production of solitary flexural waves on domain walls in orthoferrites requires a separate theoretical analysis with allowance for the role of the surface and supersonic instability of dynamic DWs in orthoferrite. It should be noted that attempts to decelerate or accelerate local sections of a dynamic DW in yttrium orthoferrite have been made before,[6] but on much longer sections. They did not give rise to solitary waves. It has not been ruled out that the solitary flexural waves observed in the present work in yttrium orthoferrite are much more stable than the analogous waves in iron garnets; this could lead to progress in the development of VBL-based memory systems.

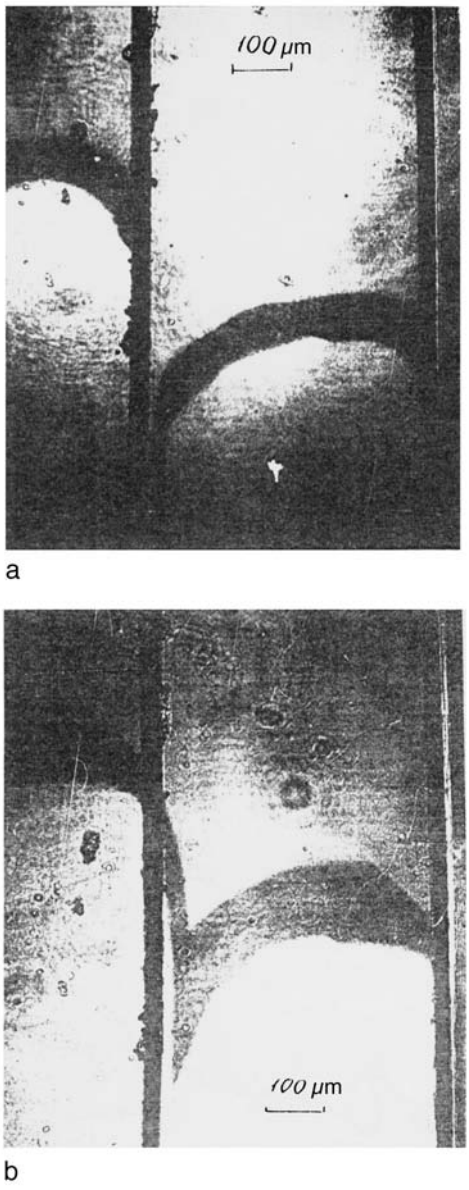

FIG. 4. Double-exposure high-speed photographs of two colliding solitary flexural waves. Onset of the annihilation process, $\Delta t = 5$ ns (a). Total annihilation, $\Delta t = 9$ ns (b).

We sincerely thank A. M. Balbashov for providing the orthoferrite single crystals, A. K. Zvezdin for a discussion of the results of this work, and J. M. Yeomans and his coauthors for kindly providing a preprint of Ref. 10. This work was supported by the

Russian Fund for Fundamental Research under Grant No. 95-02-06188a, for which the authors are deeply grateful.

[1] M. V. Chetkin, I. V. Parygina, and L. L. Savchenko, Zh. Éksp. Teor. Fiz. **110**, 1873 (1996) [JETP **83**, 1031 (1996)].
[2] A. Thiaville, Ben Youssef, Y. Nakatani, and J. Miltat, J. Appl. Phys. **69**, 6090 (1991).
[3] K. P. Belov, A. K. Zvezdin, A. M. Kadomtsev, and R. Z. Levitin, *Orientational Phase Transitions in Rare-Earth Magnets* [in Russian], Nauka, Moscow, 1979.
[4] M. V. Chetkin and S. M. Gadetskiĭ, JETP Lett. **38**, 308 (1983).
[5] M. V. Chetkin, Yu. N. Kurbatova, and A. I. Akhutkina, Phys. Lett. A **215**, 211 (1996); J. Appl. Phys. **79**, 6132 (1996).
[6] V. G. Barjakhtar, M. V. Chetkin, B. A. Ivanov, and S. N. Gadetskiy, *Dynamics of Topological Magnetic Solitons*, Springer Tracts in Modern Physics, Berlin, 1994, Vol. 129, p.182.
[7] S. V. Gomonov, A. K. Zvezdin, and M. V. Chetkin, Zh. Éksp. Teor. Fiz. **94**, 133 (1988) [Sov. Phys. JETP **67**, 2250 (1988)].
[8] A. K. Zvezdin and A. F. Popkov, JETP Lett. **39**, 419 (1988).
[9] N. Papanicolaou, Phys. Rev. B **51**, 15062 (1995).
[10] C. Micheletti, R. B. Griffits, and J. M. Yeomans, Preprint 96–235, University of Oxford (1996).
[11] E. A. Balykina, E. A. Gan'shina, and G. S. Krinchik, Zh. Éksp. Teor. Fiz. **93**, 1879 (1987) [Sov. Phys. JETP **66**, 1073 (1987)].
[12] M. V. Chetkin, S. V. Gomonov, and Yu. N. Kurbatova, Fiz. Tverd. Tela (Leningrad) **31**, 212 (1989) [Sov. Phys. Solid State **31**, 295 (1989)].

Translated by M. E. Alferieff

Fine structure of excitonic levels in quantum dots

R. I. Dzhioev, B. P. Zakharchenya, E. L. Ivchenko, V. L. Korenev, Yu. G. Kusraev, N. N. Ledentsov, V. M. Ustinov, A. E. Zhukov, and A. F. Tsatsul'nikov

A. F. Ioffe Physicotechnical Institute, Russian Academy of Sciences, 194021 St. Petersburg, Russia

(Submitted 21 April 1997)
Pis'ma Zh. Éksp. Teor. Fiz. **65**, No. 10, 766–771 (25 May 1997)

The experimental results of a study of the fine structure of the levels of excitons localized in InAlAs quantum dots in an AlGaAs matrix are reported. Transformations from optical orientation to alignment and from alignment to orientation, which occur due to the exchange splitting of a dipole-active excitonic doublet and are allowed by the low symmetry of a quantum dot, are observed in a longitudinal magnetic field (Faraday geometry). A comparison of theory with experiment for a self-organized ensemble of quantum dots enables a determination of the character of the distribution over the dipole orientations for resonance optical transitions. © *1997 American Institute of Physics.* [S0021-3640(97)00810-4]

PACS numbers: 73.20.Dx, 71.35.−y, 33.15.Pw

When the electron and hole spin states are taken into account, the energy levels of excitons in semiconductors are degenerate, even in the case of simple bands. Specifically, the ground state $e1$-$hh1(1s)$ of an exciton with a heavy hole in quantum wells with the zinc blende lattice is fourfold degenerate and is characterized by the angular momentum projections $M=s+j=\pm 1$ and ± 2, where the electron spin $s=\pm 1/2$ and the hole angular momentum $j=\pm 3/2$. The exchange interaction splits this level into a radiative doublet $|\pm 1\rangle$ and two close-lying, optically-inactive singlets. When the exciton is localized in an anisotropic island or anisotropic quantum dot, the symmetry of the system is lowered and the radiation doublets should split into two sublevels which are linearly polarized in two orthogonal directions whose orientation is determined by the form of the localizing potential.[1] In an optical near-field investigation of the photoluminescence spectra of excitons localized in GaAs/AlGaAs(001) quantum wells, Gammon *et al.*[2] observed exchange splitting of the $e1$-$hh1(1s)$ doublet into two components polarized along the [110] and [1$\bar{1}$0] axes. The analogous splitting occurring in type-II GaAs/AlGaAs(001) superlattices on account of the localization of an exciton at an individual interface and the low (C_{2v}) symmetry of a single isolated interface[3] has been studied by polarized photoluminescence methods.[4,5] It was shown that the observation of the ''optical orientation–optical alignment'' or ''alignment–orientation'' transformation in a magnetic field $\mathbf{B}\|z$, i.e., the observation of the linear (circular) polarization of the photoluminescence in the case of circularly (linearly) polarized excitation, makes it possible to determine reliably the magnitude of the splitting and the direction of polarization of the optically active sublevels without resolving the fine structure spectrally. In the present work we investi-

gated the fine structure of localized excitons in a self-organized system of InAlAs/AlGaAs quantum dots.

The structures investigated were grown on semi-insulating GaAs(100) substrates by molecular-beam epitaxy in a Riber 32P system with a solid-state source of As_4. A quantum-dot array was formed in a process of self-organized growth at a temperature of 485 °C by depositing $In_xAl_{1-x}As$ with an effective thickness of 1.6 nm ($x=0.45$).[6] The rest of the structure was grown at a temperature of 700 °C under conditions of enrichment with arsenic. The active region in the sample consists of three rows of quantum dots separated by 5 nm thick $Al_{0.3}Ga_{0.7}As$ layers. It is bounded on the substrate and surface sides by 50-period $Al_{0.45}Ga_{0.55}As$ (2 nm)/GaAs (1 nm) superlattices, which are followed by 0.15 and 0.1 μm thick $Al_xGa_{1-x}As$ ($x=0.45$–0.6) and $Al_{0.6}Ga_{0.4}As$ layers, respectively. The RHEED pattern from the surface of the growing film was used to monitor the transition from two-dimensional uniform to three-dimensional nonuniform growth of InAlAs.

The samples were placed at the center of a superconducting solenoid and loaded into a cryostat with liquid helium. The helium was pumped down to a temperature $T=2$ K. Both quasiresonance (Kr^+ laser, $\lambda_{ex}=6764$ Å) and nonresonance (He–Ne laser, $\lambda_{ex}=6328$ Å) photoexcitation were performed. The exciting light was incident on the sample at a small angle with respect to the growth axis z, along which the intensity was recorded in the ''reflection'' geometry, and the polarization of the luminescence was analyzed in the Faraday geometry. In the experiments we used a modulation method in which the position of the analyzer is fixed and the sample is excited by light with a variable sign of the circular or linear polarization at the frequency 26.61 kHz of a photoelastic modulator.[5] The values of the effective polarization were measured:

$$\rho_\alpha^c=\frac{I_\alpha^{\sigma_+}-I_\alpha^{\sigma_-}}{I_\alpha^{\sigma_+}+I_\alpha^{\sigma_-}},\quad \rho_\alpha^l=\frac{I_\alpha^{110}-I_\alpha^{\bar{1}10}}{I_\alpha^{110}+I_\alpha^{\bar{1}10}},\quad \rho_\alpha^{l'}=\frac{I_\alpha^{100}-I_\alpha^{010}}{I_\alpha^{100}+I_\alpha^{010}}. \tag{1}$$

Here the symbol I_β^α represents the intensity of the recombination radiation in the (α,β) configuration of the polarizer and analyzer, where α and β stand for linear polarization along the [100], [010], [110], or [$\bar{1}$10] axis or for circular polarization σ_+ or σ_-.

The low-temperature photoluminescence spectrum of the experimental structure under nonresonance excitation consists of a single band with half-width $\Delta=30$ meV and a maximum at $E=1.787$ eV. Under quasiresonance excitation ($\hbar\omega=1.832$ eV), peaks displaced from the exciting line by an amount equal to the energy of optical phonons in GaAs (35 meV) and AlAs (48 meV) as well as a weakly expressed structure appear in the radiation spectrum. Such a transformation of the photoluminescence spectrum under resonance excitation was observed in Refs. 7 and 8 for an analogous system of quantum dots. The experimental data presented below were obtained on a phonon peak displaced from the laser line by 35 meV. Similar results are also obtained on a different phonon line shifted by 48 meV from the exciting line.

Figure 1a displays the degree of circular polarization as a function of the longitudinal magnetic field (Faraday geometry) with excitation by circularly polarized light. A substantial increase in the degree of polarization of the radiation followed by saturation

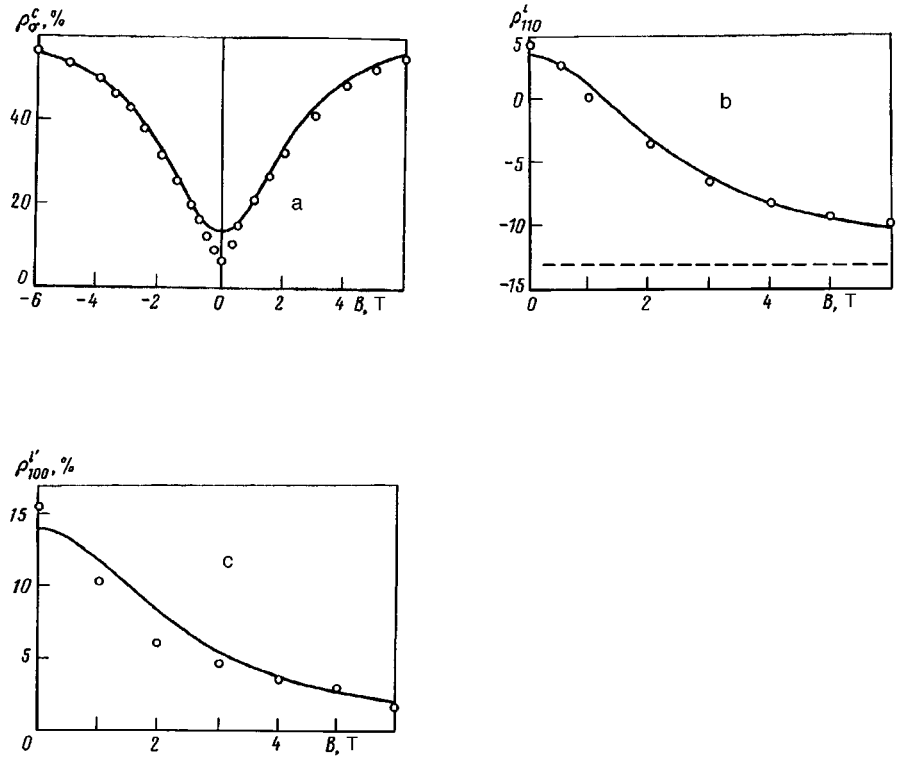

FIG. 1. Optical orientation (a) and optical alignment of excitons along the [110] and [$\overline{1}$10] axes (b) and along the [100] and [010] axes (c) in a structure with quantum dots in a longitudinal magnetic field. The photoluminescence was recorded at the wavelength 6890 Å under quasiresonance excitation with $\lambda_{ex}=6764$ Å. The solid lines show the computational results obtained with the following values of the parameters: $\hbar\tilde{\Omega}/g_\parallel\mu_0=\hbar\tilde{\Omega}_2/g_\parallel\mu_0=1.56$ T, $P_c^0=47\%$, $P_l^0=34\%$, $P_{l'}^0=28\%$.

are observed. The characteristic scale of the variation in the degree of polarization is determined by the energy splitting of the excitonic radiation doublet and equals about 2.5 T.

Optical alignment of excitons is observed under excitation with light linearly polarized along the [110] axis as well as along the [100] axis (Figs. 1b and 1c). In a longitudinal magnetic field linear polarization is suppressed in the same characteristic range of fields where an increase of circular polarization is observed (see Fig. 1a). We note that suppression of the alignment along [110] is determined by the difference of the degrees of linear polarization in zero and strong magnetic fields, since an intensity modulation is superposed on the measured degree of effective linear polarization ρ_{110}^l. This intensity modulation is due to the difference in the absorption coefficients between light polarized along the [110] and [$\overline{1}$10] axes (linear dichroism), equals 13%, and is independent of the field B. There is no linear dichroism in the case of excitation along the [100] and [010] axes.

As indicated at the beginning of this letter, the combination of an anisotropic ex-

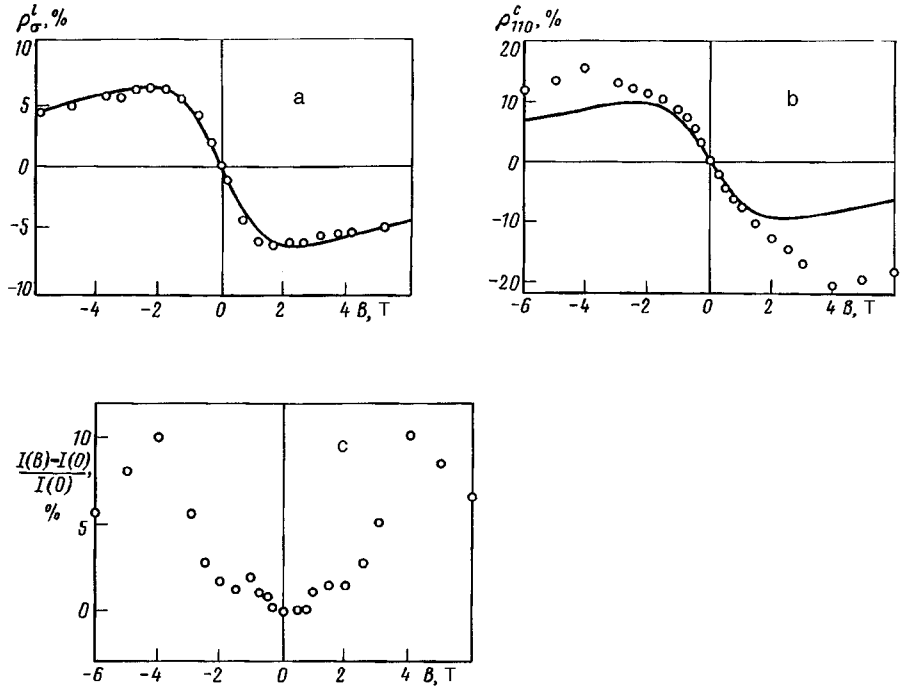

FIG. 2. Conversion of optical alignment along the [110] axis into orientation (a) and conversion of orientation into alignment along the [110] and [1$\bar{1}$0] axes (b) in a longitudinal magnetic field. The solid lines were calculated for the same values of the parameters as the curves in Fig. 1, and the out-of-balance factor $f=0.55$. (c) — Change produced in the intensity of the excitonic photoluminescence by anticrossing of a sublevel of a radiative doublet with an optically inactive state of the exciton.

change interaction and the Zeeman effect in an exciton results in intercoupling of the optical orientation and alignment. This effect is demonstrated in Fig. 2a and 2b: In the experimental structure with quantum dots in a longitudinal magnetic field the orientation of the excitonic spins is intercoupled with the alignment of the oscillating dipole moments in the system of axes [110] and [1$\bar{1}$0]. It should be noted particularly that under excitation with circularly polarized light in a magnetic field a component of linear polarization in the system of axes [100] and [010] does not arise, nor is the reverse effect observed, wherein linear polarization along the axes [100] and [010] is transformed into circular polarization is also not observed.

The intensity of the photoluminescence in a magnetic field was also found to exhibit a resonance change, associated with the anticrossing of the radiative and nonradiative sublevels of the $e1$-$hh1(1s)$ quartet (Fig. 2c). It is obvious that anticrossing occurs at $B=4$ T. A resonance variation in the circular polarization of the radiation is observed for the same value of the field and for excitation with light with a fixed linear polarization $\mathbf{E} \parallel [100]$. Anticrossing of excitonic sublevels has been observed previously in InAs/GaAs quantum dots.[9]

To analyze the optical orientation and alignment of excitons it is convenient to treat

the doublet $|\pm 1\rangle$ as a pair of states with pseudospin $S=1/2$. Then the Hamiltonian describing the splitting of the doublet in a longitudinal magnetic field $\mathbf{B} \parallel z$ can be written in the form

$$\mathscr{H}=\hbar(\Omega_1\sigma_1+\Omega_2\sigma_2+\Omega_\parallel\sigma_3), \tag{2}$$

where $\hbar\Omega_\parallel=g_\parallel\mu_0 B$, $g_\parallel$ is the longitudinal g factor of the exciton, μ_0 is the Bohr magneton, σ_i are the Pauli matrices for the axes 1, 2, and 3 of the effective space in which the pseudospin rotates, and $\hbar\Omega_1$ and $\hbar\Omega_2$ are the exchange splitting parameters of the radiative doublet. For $\Omega_1=\Omega_\parallel=0$, $\Omega_2\neq 0$ the components of the doublet are polarized along the axes $x \parallel [1\bar{1}0]$ and $y \parallel [110]$ and for $\Omega_2=\Omega_\parallel=0$, $\Omega_1\neq 0$ they are polarized along the axes $x' \parallel [100]$, $y' \parallel [010]$ rotated by 45° relative to the x, y axes. The average values of the pseudospin projections are related with the degrees of polarization of the emitted light (Stokes parameters) by the simple relations $P_{l'}=2S_1$, $P_l=-2S_2$, and $P_c=2S_3$. Similar relations exist between the polarization of the incident light and the direction of pseudospin $\mathbf{S}^0$ at the moment of excitation, if no partial loss of polarization occurs in the excitation process. According to Eq. (2), the pseudospin precesses around the vector $\vec{\Omega}(\Omega_1,\Omega_2,\Omega_\parallel)$with frequency $|\vec{\Omega}|$. If this frequency greatly exceeds the reciprocal τ^{-1} of the exciton lifetime and the spin relaxation time satisfies $\tau_s \gg \tau$, to find the average pseudospin vector $\mathbf{S}$ it is sufficient to project the vector $\mathbf{S}^0$ on the direction of $\vec{\Omega}$, i.e., $\mathbf{S}=\vec{\Omega}(\vec{\Omega}\cdot\mathbf{S}^0)/|\vec{\Omega}|^2$. This yields a relation between the polarization of the photoluminescence and the exciting light

$$P_i=\Lambda_{ij}P_j^0 \quad (i,j=l',l,c), \tag{3}$$

$$||\Lambda_{ij}||=\frac{1}{\Omega_1^2+\Omega_2^2+\Omega_\parallel^2}\begin{bmatrix} \Omega_1^2 & -\Omega_1\Omega_2 & \Omega_1\Omega_\parallel \\ -\Omega_1\Omega_2 & \Omega_2^2 & -\Omega_2\Omega_\parallel \\ \Omega_1\Omega_\parallel & -\Omega_2\Omega_\parallel & \Omega_\parallel^2 \end{bmatrix}. \tag{4}$$

We note that if level anticrossing and absorption dichroism are neglected, the polarization P_i^α equals the values ρ_α^i introduced in Eq. (1).

In the experiment, light emitted by a large number of quantum dots is analyzed and the matrix $\Lambda_{\alpha\beta}$ must be averaged over the Ω_1 and Ω_2 distributions, to which shape fluctuations of the quantum dots and local deformations contribute. The apparent inconsistencies in the experimental results — 1) optical alignment of excitons for any direction of linear polarization of the exciting light and 2) ''orientation–alignment'' conversion in a longitudinal field, indicating that the [110] and [$\bar{1}$10] axes are not equivalent — can be satisfactorily explained by assuming that the positive and negative values of Ω_1 are equally probable and the average value of Ω_2 is different from zero. In this case, after the components Λ_{ij} are averaged, the components which are odd in Ω_1 vanish and the matrix (4) assumes the form

$$||\Lambda_{ij}||=\frac{1}{\tilde{\Omega}_1^2+\tilde{\Omega}_2^2+\tilde{\Omega}_\parallel^2}\begin{bmatrix} \tilde{\Omega}_1^2 & 0 & 0 \\ 0 & \tilde{\Omega}_2^2 & -f\tilde{\Omega}_2\Omega_\parallel \\ -f\tilde{\Omega}_2\Omega_\parallel & 0 & \Omega_\parallel^2 \end{bmatrix}. \tag{5}$$

To calculate approximately the random variance in Ω_1 and Ω_2 relative to the average values $\langle\Omega_1\rangle=0$, $\langle\Omega_2\rangle\neq 0$, on switching from expression (4) to Eq. (5) we replaced Ω_n^2

by the mean-square value $\langle \Omega_n^2 \rangle \equiv \tilde{\Omega}_n^2$ $(n=1,2)$ and $\Omega_2 \Omega_\parallel$ by $f\tilde{\Omega}_2 \Omega_\parallel$, where $f=\langle \Omega_2 \rangle / \tilde{\Omega}_2$ and $|f|<1$. The computational results obtained with expressions (3) and (5) are displayed in Figs. 1, 2a, and 2b (solid lines). The deviation of P_j^0 from 1 is due to polarization losses accompanying quasiresonance excitation of the excitons. As one can see from Fig. 2b, the influence of anticrossing on the polarization cannot be completely eliminated in the experiment. A separate analysis is required in order to take this effect into account on the basis of the theory in Ref. 10.

In summary, in contrast to type-II GaAs/AlAs superlattices[5] and the structure GaAs/AlGaAs with quantum wells,[2] the position of the principal axes of the anisotropic exchange splitting for localized excitons in InAlAs/AlGaAs quantum dots is not fixed in the [110] and [1$\bar{1}$0] directions and is characterized by two linearly independent parameters Ω_1 and Ω_2. The quantum dots investigated are shaped in the form of pyramids (possibly, truncated), whose height is parallel to the axis $z \parallel [001]$ and whose rectangular base is oriented along the [100] and [010] axes.[6,11] Quantum dots with a square base are characterized by C_{2v} point symmetry, for which $\Omega_1=0$, $\Omega_2 \neq 0$, and the components of the radiation doublet are polarized along the [110] and [1$\bar{1}$0] axes. In the general case of a rectangular base the symmetry is lowered to C_2, and $\Omega_1 \neq 0$. It is obvious that this quantity has opposite signs for quantum dots with bases extended in the [100] and [010] directions. If the rectangular bases are not predominantly oriented in the (001) plane, the average value $\langle \Omega_1 \rangle = 0$ but the mean-square value of Ω_1 is nonzero.

This work was supported in part by the Volkswagen Foundation, the Russian Fund for Fundamental Research under Grants Nos. 95-02-06038 and 96-02-17824, and INTAS under Grant No. INTAS-REPR 95-618.

[1] S. V. Goupalov, E. L. Ivchenko, and A. V. Kavokin, *Proceedings of the International Symposium ''Nanostructures: Physics and Technology,''* St. Petersburg, 1996, p. 322.
[2] D. Gammon, E. S. Snow, B. V. Shanabrook *et al.*, Phys. Rev. Lett. **76**, 3005 (1996).
[3] I. L. Aleĭner and E. L. Ivchenko, JETP Lett. **55**, 692 (1992); E. L. Ivchenko, A. Yu. Kaminski, and U. Rössler, Phys. Rev. B **54**, 5852 (1996).
[4] E. L. Ivchenko, V. P. Kochereshko, A. Yu. Naumov *et al.*, Superlattices Microstruct. **10**, 497 (1991).
[5] R. I. Dzhioev, H. M. Gibbs, E. L. Ivchenko *et al.*, (in press).
[6] A. F. Tsatsul'nikov, A. Yu. Egorov, A. E. Zhukov *et al.*, Fiz. Tekh. Poluprovodn. **31**, 109 (1997) [Semiconductors **31**, 88 (1997)].
[7] N. N. Ledentsov, M. Grundmann, N. Kirstaedter *et al.*, *Proceedings of the 22nd International Conference on Semiconductor Physics*, Vancouver, Canada, 1994, p. 1855; R. Heitz, M. Grundmann, N. N. Ledentsov *et al.*, Appl. Phys. Lett. **68**, 361 (1996).
[8] S. Raymond, S. Fafard, S. Charbonneau *et al.*, Phys. Rev. B **52**, 17238 (1995).
[9] B. Kowalski, P. Omling, M. S. Miller *et al.*, Solid-State Electron. **40**, 367 (1996).
[10] E. L. Ivchenko and A. Yu. Kaminskiĭ, Fiz. Tverd. Tela (St. Petersburg) **37**, 1418 (1995) [Phys. Solid State **37**, 768 (1995)].
[11] M. Grundmann, O. Strier, and D. Bimberg, Phys. Rev. B **51**, 11969 (1995).

Translated by M. E. Alferieff

Competition between nuclear ferromagnetism and superconductivity

A. M. Dyugaev
L. D. Landau Institute of Theoretical Physics, Russian Academy of Sciences, 142432 Chernogolovka, Moscow Region, Russia

I. D. Vagner and P. Wyder
Max-Planck-Institut für Festkorperforschung, BP166, F-38042 Grenoble, France

(Submitted 24 April 1997)
Pis'ma Zh. Éksp. Teor. Fiz. **65**, No. 10, 772–775 (25 May 1997)

A qualitative theory of nuclear magnetism against a background of superconductivity in metals is proposed. Even though the superconducting transition temperature is much higher than the nuclear ordering temperature, nuclear ferromagnetism can partially or completely destroy superconductivity. An experimental method of determining the effective electron–nuclear spin–spin interaction constant for superconductors is discussed. © *1997 American Institute of Physics.* [S0021-3640(97)00910-9]

PACS numbers: 76.50.+g, 74.25.Nf, 75.50.Bb, 75.50.Cc

1. The strong effect of nuclear ferromagnetism on superconductivity in metals was first discovered in Ref. 1. The fact that ferromagnetic nuclear order can destroy superconductivity was pointed out in Ref. 2. The crux of the phenomenon is, qualitatively, as follows. Even though the superconducting phase transition temperature T_{ce} is ordinarily many orders of magnitude higher than the nuclear ordering temperature T_{cn}, the energy loss accompanying the destruction of superconductivity is only of the order of T_{ce}^2/ϵ_F per electron (ϵ_F is the Fermi energy of the electrons) and not T_{ce}, as appears at first glance. This is because it is only the relatively few electrons that are near the Fermi surface which are responsible for the superconductivity. However, the ferromagnetic nuclear ordering energy is of the order of T_{cn} per nucleus. Therefore if the density of nuclei is not too different from that of the electrons, we obtain as a rough criterion for the destruction of superconductivity $T_{cn}\epsilon_F > T_{ce}^2$.

2. The metallic compound $AuIn_2$, which is a type-I superconductor with critical temperature $T_{ce}=0.207$ K and critical magnetic field $H_c(T\to 0)=1.45$ mT, was investigated in Ref. 1. A ferromagnetic phase transition in the system of In nuclei is observed at $T_{cn}\cong 35\ \mu$K. In consequence of this transition, as T decreases, H_c decreases to 0.87 mT and broadening of the superconducting phase transition line $H_c(T)$ at temperatures $T<T_{cn}$ occurs. As a result of the good thermal contact between them, the electrons and nuclei are in thermodynamic equilibrium, i.e., $T^n=T^e$. The equilibration time is about 1 h. This letter proposes a qualitative theory of the phenomenon discovered in Ref. 1 and predicts results for possible experiments where superconductivity and nuclear ferromagnetism compete with each other.

The (H,T) phase diagram of the metal depends on the method by which nuclear order is obtained. In Ref. 1 low temperatures were achieved by the nuclear demagnetization method, i.e., first, a phase transition to a ferromagnetic state occurs in the nuclear system in the normal phase of the metal and then the metal becomes superconducting as the magnetic field decreases. Therefore the phase transition occurs as a function of the magnetic field and not temperature, in which case the nuclear system becomes ferromagnetic in the superconducting phase as T decreases. This greatly simplifies the analysis of the phenomenon because superconductivity does not have a back effect on the nuclear ferromagnetism: Superconductivity appears in a state with a fixed nuclear magnetic order. This removes in part the question of the existence of a nonuniform superconducting state, i.e., a LOFF phase.[3,4] The transition into this phase can occur only with a long time delay, if the ordinary uniform phase is metastable.

A nuclear domain structure with a spontaneous nuclear moment $M_n(T)$ within a domain arises at temperatures $T<T_{cn}$. The maximum value of $M_n(T)$ corresponds to the total polarization of the nuclei in a domain. The average nuclear moment $\overline{M_n}$ over the metal sample depends on the initial demagnetization conditions, since the domain walls move extremely slowly. To determine the temperature dependence of the critical magnetic field H_c, we employ the well-known[3,5] expression for the free energy F_S of the superconductor,

$$F_S-F_n=\frac{\nu}{4}(2J^2-\Delta_0^2)+\frac{B_c^2}{8\pi},\quad J\equiv\mu_e H_n,\quad B_c=H_c+4\pi\overline{M_n}, \tag{1}$$

where F_n is the energy of the normal metal; ν is the electronic density of states; Δ_0 is the gap in the electron spectrum at $T=0$; J is the energy separation arising between electrons with opposite spins as a result of the magnetization of the electrons by the nuclei; and, H_n is the effective nuclear field at an electron and is proportional to the magnetic nuclear moment $M_n(T)$. Leaving unspecified, for the time being, the relation between $M_n(T)$ and $H_n(T)$, we obtain from Eq. (1) the dependence of $B_c(T)$ on $M_n(T)$ or $M_n(T)$ on $B_c(T)$:

$$B_c(T)=B_c(T_{cn})\left[1-\frac{M_n^2(T)}{M_n^2(0)}\left(1-\frac{B_c^2(0)}{B_c^2(T_{cn})}\right)\right]^{1/2},$$

$$M_n(T)=M_n(0)\left[\frac{B_c^2(T_{cn})-B_c^2(T)}{B_c^2(T_{cn})-B_c^2(0)}\right]^{1/2}. \tag{2}$$

The measured quantity is not $B_c(T)$ but $H_c(T)$. The average nuclear moment $\overline{M_n}$ adjusts to the external magnetic field extremely slowly and is mainly determined by the initial nuclear demagnetization conditions, i.e., by the value of the magnetic field at which nuclear order first appeared, and not by the value of $H_c(T)$. Therefore, upon varying the initial experimental conditions, one can determine $H_c(T)$ from Eq. (2) by subtracting from $B_c(T)$ the T-independent constant $4\pi\overline{M_n}$. The first relation in Eqs. (2) makes it possible to determine, by a rough calculation of $M_n(T)$ in the mean-field approximation, the curve $H_c(T)$ of coexistence of the superconducting and normal phases of the metal. The second relation in Eqs. (2) is more informative and makes it possible to determine from the experimental temperature dependence of H_c the magnetization $M_n(T)$ of a

cubic Heisenberg ferromagnet with spin $S=9/2$ (nuclear spin I_n). We note that in Ref. 1 it was indicated that the measured T dependence of H_c does not correspond to existing theoretical models; however, expressions of the type (2) were not analyzed. Since in Ref. 1 $H_c(T)$ did not depend too strongly on the initial experimental conditions, there are grounds for not distinguishing between B_c and H_c in Eq. (1), i.e., $\overline{M_n}$ can be set equal to zero. Then the value of the maximum nuclear field $H_n(T=0)$ reached upon total polarization of the nuclei can be determined from Eq. (1):

$$H_n(0)=\frac{\Delta_0}{\mu_e\sqrt{2}}\left(1-\frac{H_c^2(0)}{H_c^2(T_{cn})}\right)^{1/2}. \tag{3}$$

Since the density of states ν does not appear in Eq. (3) and $H_c(0)$ and $H_c(T_{cn})$ are known[1] for $AuIn_2$, we obtain, assuming that Δ_0 and T_{ce} are related in accordance with the BCS theory,

$$H_n(0)\approx 0.15 \text{ T}, \quad J(0)\equiv\mu_e H_n(0)\approx 0.21 \text{ K}.$$

The parameter $H_n(0)$ is an important characteristic of the metal. It is known only for two substances — Li and Na (Ref. 6), and it determines the shift of the electronic resonance line with total polarization of the nuclei by the Overhauser method. This shift is very difficult to measure.[6]

3. For this reason, we shall discuss an experimental method of determining the value of H_n at least for superconductors. For this we make use of the possibility of producing a nonequilibrium state in which the nuclear temperature is decoupled from the electron temperature: $T^n \ll T^e$. If $T^e \ll T_{ce}$, then T_e does not appear in the final expressions for the observed quantities, so that it can be conventionally set equal to zero and only the nuclear temperature need be followed. If the experiment starts at a high magnetic field H_0 and high nuclear temperature $T_0^n \gg T_{cn}$, when the nuclear system is almost completely polarized and is ideal, and the magnetic field H is switched off adiabatically, then the nuclear magnetic moment will persist right up to the point of the phase transition of the metal to the superconducting state. It is important that for the nuclear system this transition occurs instantaneously at a nuclear magnetic moment $M_n(H_0,T_0^n)$. The critical field B_c is found from Eq. (2), where $M_n(T)$ must be replaced by $M_n(H_0,T_0^n)$. The initial conditions H_0 and T_0^n can always be chosen so that the magnetization of the electrons by the nuclei (the parameter J in Eq. (1)) is more consequential than the replacement of H_c by B_c in Eq. (1). Indeed, in Eq. (1) J competes with the small quantity Δ_0, while B_c can be estimated from the expression $B_c=H_c(1+\chi_n)$, where χ_n is the nuclear susceptibility, which is small at high temperatures $T \gg T_{cn}$. Thus, $H_c(H_0,T_0^n)$ can be measured during adiabatic demagnetization. In the superconducting phase the field B equals zero and the nuclear moment M_n relaxes to zero. Now, if a magnetic field is switched on, then superconductivity will be destroyed in a field H_{c0} which is higher than $H_c(H_0,T_0^n)$, and from Eq. (1) we find the parameter

$$H_n(H_0,T_0)=\frac{\Delta_0}{\mu_e\sqrt{2}}\left(1-\frac{B_c^2(H_0,T_0^n)}{H_{c0}^2}\right)^{1/2}. \tag{4}$$

Since the values of H_0 and T_0 were chosen such that the nuclear–nuclear interaction can be neglected during the entire adiabatic demagnetization stage, we have

$$H_n(H_0, T_0^n) = H_n^0 B_s\left(\frac{\mu_n H_0}{T_0^n}\right), \tag{5}$$

where B_s is the Brillouin function and H_n^0 is the limiting value of H_n for $\mu_n H_0 \gg T_0^n$, when all nuclei are polarized. Therefore by measuring H_c versus T_0^n and H_0 it is possible to determine on the basis of Eqs. (4) and (5) the effective magnetic nuclear field H_n^0 under conditions of total polarization of the nuclei. We note that in Ref. 7, where nuclear relaxation in superconducting Al was investigated, supercooling of the nuclear system, which causes H_c to differ from H_{c0}, was observed during on–off cycling of the magnetic field.

Let us now determine the phenomenological electron–nuclear spin–spin interaction constant J_0 in the free-electron model, neglecting the band structure of the metal. For this, we write this interaction in the form[8]

$$V_{en} = \frac{J_0}{n_n}\delta(\mathbf{r}_e - \mathbf{r}_n)\frac{(\boldsymbol{\sigma}\cdot\mathbf{S})}{S}, \tag{6}$$

where n_n is the density of nuclei. If now the factor J appearing in Eq. (1) and characterizing the magnetization of the electrons by the nuclei is expressed in terms of V_{en}, one obtains[8]

$$J(H_0, T_0^n) = J_0 B_s\left(\frac{\mu_n H_0}{T_0^n}\right). \tag{7}$$

Analysis of the experimental data presented in Ref. 1 for $AuIn_2$ gives $J_0 \approx 0.21$ K. A nonequilibrium nuclear magnetization should strongly affect superconductivity in the metals In, Ta, Bi (films), Sb, and Tl, which, according to an analysis of the Knight shift data, have high values of the superconducting transition temperature T_{ce} together with a strong electron–nuclear spin–spin interaction V_{en}.

We thank A. Zyuzin and Yu. Ovchinnikov for a discussion. This work was supported by the Russian Fund for Fundamental Research. I. D.V. and P. V. thank the German–Israeli Foundation for the Support of Scientific Research (Grant No. I-0222-136.07/91).

[1] S. Rehmann, T. Herrmannsdorfer, and F. Pobell, Phys. Rev. Lett. **78**, 1122 (1997).
[2] A. M. Dyugaev, I. D. Vagner, and P. Wyder, JETP Lett. **64**, 207 (1996).
[3] A. I. Larkin and Yu. N. Ovchinnikov, Zh. Éksp. Teor. Fiz. **47**, 1136 (1964) [Sov. Phys. JETP **20**, 762 (1964)].
[4] P. Fulde and R. A. Ferrel, Phys. Rev. **135**, 550 (1964).
[5] A. A. Abrikosov, *Fundamentals of the Theory of Metals*, North-Holland, Amsterdam, 1988 [Russian translation, Nauka, Moscow, 1987].
[6] J. Winter, *Magnetic Resonance in Metals*, Clarendon Press, Oxford, 1971 [Russian translation, Mir, Moscow, 1987].
[7] L. C. Hebel and C. P. Slichter, Phys. Rev. **113**, 1504 (1959).
[8] A. A. Abrikosov. Phys. **2**, 21 (1965).

Translated by M. E. Alferieff

Localized states at the helicoidal phase transition

A. Buzdin and Y. Meurdesoif
CPTMB-LPT, University Bordeaux I, 33175 Gradignan Cedex, France

(Submitted 3 April 1997; resubmitted 24 April 1997)
Pis'ma Zh. Éksp. Teor. Fiz. **65**, No. 10, 776–781 (25 May 1997)

The appearence of a new type of localized states at the helicoidal transition is predicted. The order parameter decays with an oscillation in the vicinity of the defect provoking the localized transition. The cases of point, linear, and planar defects are considered, and the specific heat jumps are calculated. © *1997 American Institute of Physics.* [S0021-3640(97)01010-4]

PACS numbers: 75.25.+z, 75.30.Kz

1. INTRODUCTION

The presence of defects and inhomogeneities of various sorts may strongly influence the phase transition in bulk materials. Surface defects are an example. If the local transition temperature near the surface is somewhat higher than in the bulk, then a localized near-surface state appears at a temperature T_{CL} slightly above the bulk critical temperature T_{C0}. This situation is characteristic for surface magnetism,[1] superconductivity localized near a twinning plane,[2] and local structural transitions.[3]

If the Landau functional approach is used to describe the phase transition, the local increase of transition temperature can be modeled by a δ-functional contribution to the free energy density, $-\gamma\delta(r)\psi^2$, where ψ is the order parameter. The problem of finding the critical temperature of the localized transition is then reduced to one of determining the eigenvalue of a corresponding equation for the order parameter $\psi(r)$. This equation, when the gradient term in the Landau free energy functional has the usual form $\sim(\nabla\psi)^2$, is just the Schrödinger equation with a δ-functional potential and self energy $E\sim(T_{CL}-T_{C0})$ (see for example Refs. 1 and 2). The one dimensional potential well always has a localized state with negative energy[4] (note that a local increase in the transition temperature corresponds to a weak negative δ-functional potential). Then near the surface (or plane defect) the temperature of the localized transition will be higher than that of the bulk transition: $T_{CL}-T_{C0}\sim\gamma^2$. For a linear defect the difference is exponentially small[4] and eventually non-observable. In the case of a point defect the local transition is absent, as there is no localized state for a weak three-dimensional δ-functional potential.[4]

However, the situation turns out to be quite different in the case of a phase transition to a helicoidal state. To be more specific, we will consider a magnetic helicoidal transition like that observed in MnSi[5] and FeGe,[6] for example. In the absence of a center of symmetry of the crystal structure, the magnetic free energy functional contains terms $\sim\lambda\mathbf{M}\cdot\mathrm{curl}\,\mathbf{M}$ (where $\mathbf{M}$ is the local magnetization) which lead to the formation of a helicoidal magnetic structure.[7] The same is true also for cholesteric liquid crystals.[8]

In the present article, we demonstrate for a helicoidal transition that even a point-like increase in the transition temperature leads to the formation of a very specific localized state above the bulk critical temperature. We calculate the structure and thermodynamic characteristics of such unusual localized states near point, linear, and planar defects.

2. LOCALIZED STATE NEAR A POINT DEFECT

We consider the problem using the Landau-type functional for the magnetic free energy:

$$F=\frac{n\theta}{M_S^2}\int\left[\tau\mathbf{M}^2+\frac{b}{2}\mathbf{M}^4+a^2(\nabla M_x)^2+a^2(\nabla M_y)^2+a^2(\nabla M_z)^2\right.$$
$$\left.+\lambda\mathbf{M}\cdot\mathrm{curl}\ \mathbf{M}-\gamma\mathbf{M}^2\delta(\mathbf{r})\right]d^3\mathbf{r}. \tag{1}$$

where θ is of the order of the magnetic transition temperature T_{C0}, n is the density of magnetic atoms, M_S is the saturation magnetization at $T=0$, and $\tau=(T-T_{C0})/T_{C0}$. Note that T_{C0} is the critical temperature of the ferromagnetic transition which occurs in the absence of the term $\lambda\mathbf{M}\cdot\mathrm{curl}\ \mathbf{M}$. In the presence of this term (the case of a crystal lattice without a center of symmetry), the transition to the helicoidal magnetic structure occurs at some temperature T_C higher than the ferromagnetic transition temperature $((T_C-T_{C0})/T_{C0}=\tau_0=(\lambda/2a)^2)$. The term $-\gamma\mathbf{M}^2\delta(\mathbf{r})$ describes the local increase in the transition temperature near the point defect, the magnetic stiffness coefficient a is of the order of the interatomic distance, and the coefficient b has the usual meaning. For simplicity, and having in mind MnSi, we consider the functional for the case of cubic crystal symmetry.

To reduce the number of coefficients, it is convenient to make a change of variable to $\mathbf{r}'\to\mathbf{r}/a$, and we will henceforth omit the prime. First we consider the question of the temperature of the localized transition and the magnetic structure that arises. For that we may neglect the term $\sim\mathbf{M}^4$ in the functional (1) and write it in the Fourier representation as

$$F=\frac{n\theta}{M_s^2}V\sum_{\mathbf{q}}\left[(\tau+q^2)\mathbf{M}_{\mathbf{q}}\cdot\mathbf{M}_{-\mathbf{q}}+i\tilde{\lambda}\mathbf{M}_{-\mathbf{q}}(\mathbf{q}\times\mathbf{M}_{\mathbf{q}})-\tilde{\gamma}\sum_{\mathbf{q}}{}'\ \mathbf{M}_{\mathbf{q}}\cdot\mathbf{M}'_{\mathbf{q}}\right]. \tag{2}$$

where $\tilde{\lambda}=\lambda/a$ and $\tilde{\gamma}=\gamma a^3$.

Minimizing the energy over $\mathbf{M}_{\mathbf{q}}$, after some algebra we obtain

$$\mathbf{M}_{\mathbf{q}}[\tilde{\lambda}^2q^2-(\tau+q^2)^2]=i\tilde{\gamma}\tilde{\lambda}(\mathbf{q}\times\mathbf{M}_0)+\frac{\tilde{\gamma}\mathbf{M}_0[\tilde{\lambda}^2q^2-(\tau+q^2)^2]}{(\tau+q^2)}$$
$$+\frac{\tilde{\gamma}\tilde{\lambda}^2[\mathbf{q}(\mathbf{q}\cdot\mathbf{M}_0)-q^2\mathbf{M}_0]}{(\tau+q^2)}, \tag{3}$$

where $\mathbf{M}_0=\mathbf{M}(\mathbf{r}=0)$ is the magnetization at the localized defect. In the absence of defect, for $\tilde{\gamma}=0$, we have from (3) $\tau=\tilde{\lambda}q-q^2$. The actual wave vector of the helicoidal

state corresponds to the maximum temperature over q. This maximum is realized for $q=q_0=\tilde{\lambda}/2$, and the transition temperature is $\tau_0=\tilde{\lambda}^2/4$, which is naturally higher than ferromagnetic critical temperature ($\tau=0$). If we are interested in the formation of the localized state just above the bulk transition at $\delta\tau=\tau-\tau_0\ll\tau_0$, the singular part of $\mathbf{M_q}$ will be related with the wave vector $|\mathbf{q}|\simeq q_0$, and we obtain from (3) the following expressions for $\mathbf{M_q}$:

$$\mathbf{M_q}=-\frac{i\tilde{\gamma}(\mathbf{q}\times\mathbf{M}_0)}{\tilde{\lambda}[\delta\tau+(q-q_0)^2]}-\frac{2\tilde{\gamma}}{\tilde{\lambda}^2}\frac{[\mathbf{q}(\mathbf{q}\cdot\mathbf{M}_0)-q^2\mathbf{M}_0]}{[\delta\tau+(q-q_0)^2]}. \tag{4}$$

The critical temperature for the appearance of the localized solution is given by the ''self-consistent'' equation

$$\mathbf{M}_0=\mathbf{M}(0)=\int \mathbf{M_q}\frac{d^3\mathbf{q}}{(2\pi)^3}. \tag{5}$$

The main contribution to the integral (5) comes from the region $|\mathbf{q}|\simeq q_0$. Taking this into account we obtain for the shift of transition temperature $\delta\tau_C=\tau_{CL}-\tau_0$, (where τ_{CL} is the critical temperature for the localized state): $\delta\tau_C=(\tilde{\gamma}\tau_0/6\pi)^2$. Then even a small local increase of ''bare'' transition temperature gives rise to a localized state. This property is a characteristic of the helicoidal transition and is absent for the ferromagnetic transition.

After taking the Fourier transform of Eq. (4), we obtain the distribution of the magnetic moment in the real space. Choosing the z axis along $\mathbf{M}(0)$, in cylindrical coordinates it may be written as

$$M_\rho=\frac{3}{2}M(0)\sqrt{\frac{\pi}{2}}\frac{(q_0\rho)(q_0z)}{[(q_0\rho)^2+(q_0z)^2]^{5/4}}\ J_{5/2}(\sqrt{(q_0\rho)^2+(q_0z)^2}),$$

$$M_\varphi=\frac{3}{2}M(0)\sqrt{\frac{\pi}{2}}\frac{(q_0\rho)}{[(q_0\rho)^2+(q_0z)^2]^{3/4}}\ J_{3/2}(\sqrt{(q_0\rho)^2+(q_0z)^2}),$$

$$M_z=\frac{3}{2}M(0)\int_0^{\pi/2}\sin^3\theta\ J_0(q_0\rho\ \sin\ \theta)\cos(q_0z\ \cos\ \theta)d\theta. \tag{6}$$

Note that in calculating the Fourier transform of (4) we have put $q=q_0$ in the nominator, as is justified for a distance of $|\mathbf{r}|2\pi/(q_0\sqrt{\delta\tau_c})$ around the defect. At larger distances the magnetic moment decreases exponentially, and the effective volume V of the localized state is $V\sim q_0^{-3}(\delta\tau_C)^{-3/2}$. It increases when $\delta\tau_C\to 0$, which is a general phenomenon for localized states[1–3] and is related with the diverging of the effective coherence length near T_C. Then for smaller $\tilde{\gamma}$ the localized state appears closer to the bulk transition temperature, but its dimensions becomes larger. The structure (6) of the localized state is rather complicated. The distribution of the magnetic moment in the plane $z=2\pi/q_0$ is presented in Fig. 1.

Knowing the magnetic moment distribution, we can obtain the jump in the specific heat at such a localized transition:

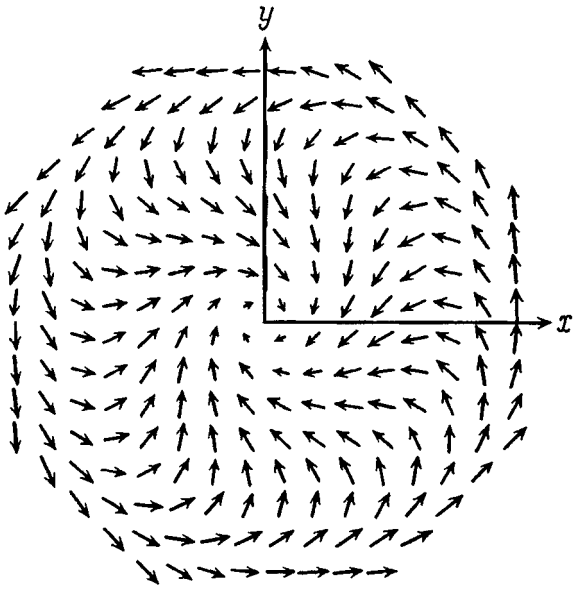

FIG. 1. The magnetic structure for a point defect in the plane $z=2\pi/q_0$. The in-plane M_x and M_y components of magnetization are presented. Note that the z axis is chosen along the magnetic moment at $x=y=z=0$.

$$\Delta C=\frac{n\theta}{M_S^2 bT_{C0}}\frac{\left[\int \mathbf{M}^2 d^3\mathbf{r}\right]^2}{\int \mathbf{M}^4 d^3\mathbf{r}}=\frac{n\theta}{M_S^2 bT_{C0}}\frac{2\pi}{I}\left(\frac{2}{3}\right)^2\frac{1}{q_0\delta\tau_C}$$

where the factor $I\simeq 1.17$ comes from numerical evaluation of the integral. The divergence of ΔC as $\widetilde{\gamma}\to 0$ can be attributed to the increase of the effective volume as $\widetilde{\gamma}\to 0$; however, the specific heat density $\Delta C/V\sim(\delta\tau_C)^{1/2}$ goes to zero for $\widetilde{\gamma}\to 0$.

3. LOCALIZED STATE NEAR A LINEAR DEFECT

The only change in the initial Landau functional for the magnetic free energy in this case is that the local increase of the critical temperature along the linear defect is described by a term $-\widetilde{\gamma}M^2(0,0,z)\delta(x)\delta(y)$, with the z axis chosen along the line. We obtain a self-consistent equation similar to (5) for $\mathbf{M}_0(q_z)$, where $\mathbf{M}_0(q_z)$ is Fourier harmonic of $M(\rho=0,z)$.

Using equation (4), we find the following system of equations giving the relation between $\delta\tau$ and the free parameter q_z, where q_z is a modulation vector along the defect:

$$M_0^x=\frac{\widetilde{\gamma}}{\widetilde{\lambda}^2}\int\frac{i\widetilde{\lambda}q_z M_0^y+(q_y^2+q_z^2)M_0^x}{\delta\tau+(\delta q)^2}\frac{d\mathbf{q}_\perp}{(2\pi)^2},$$

$$M_0^y = \frac{\tilde{\gamma}}{\tilde{\lambda}^2} \int \frac{i\tilde{\lambda} q_z M_0^x + (q_x^2 + q_z^2) M_0^x}{\delta\tau + (\delta q)^2} \frac{d\mathbf{q}_\perp}{(2\pi)^2},$$

$$M_0^z = \frac{2\tilde{\gamma}}{\tilde{\lambda}^2} \int \frac{q_\perp^2 M_0^z}{\delta\tau + (\delta q)^2} \frac{d\mathbf{q}_\perp}{(2\pi)^2}. \tag{7}$$

The critical temperature $\delta\tau_c$ must be obtained by maximization of $\delta\tau$ with respect to q_z. One solution with $M_0^x = M_0^y = 0$ can be easily found. For this solution maximum transition temperature is reached at $q_z = 0$ and $\delta\tau_c = (\tilde{\gamma}\tilde{\lambda}/8)^2$.

However there exists another solution of the type $M_0^x + iM_0^y$ and $M_0^z = 0$ which gives a higher transition temperature. For this solution, the maximum temperature $\delta\tau$ corresponds to wave vector q_z near q_0. We obtain for

$$\varepsilon = \frac{q_0}{q_z} - 1 = \left(\frac{2}{3\pi}\right)^{1/4} \left(\frac{\delta\tau}{q_0^2}\right)^{3/8} \approx \left(\frac{2}{3\pi}\right)^{1/4} \left(\frac{\tilde{\gamma}}{2}\right)^{3/4}$$

the transition temperature

$$\delta\tau_c \approx \left(\frac{\tilde{\gamma}\tilde{\lambda}}{4}\right)^2 \left(1 - 2\left(\frac{4}{3\pi}\right)^{3/4} \tilde{\gamma}^{1/4}\right). \tag{8}$$

This critical temperature is higher than that for the solution $M_0^x = M_0^y = 0$. We conclude that the helicoidal localized state with a modulation vector $\approx q_0$ along z axis must appear at the temperature $\tau_0 + \delta\tau_c$ given by (8).

The structure in the real space is

$$M^x = M(0)\cos(q_0 z) J_0(q_0 \rho \sqrt{2\varepsilon}),$$

$$M^y = M(0)\sin(q_0 z) J_0(q_0 \rho \sqrt{2\varepsilon}). \tag{9}$$

The range of application of these equations is $\rho \ll 1/(q_0 \tilde{\gamma}^{5/8})$. At larger distances, the magnetization decreases exponentially. Figure 2 illustrates the distribution of the magnetization. The specific heat jump at the transition is

$$\Delta C \simeq \frac{n\theta}{M_S^2 b T_{C0}} \left(\frac{\pi^3}{12}\right)^{1/4} \frac{1}{4\tilde{\lambda}^2 \tilde{\gamma}^{1/4} \ln \tilde{\gamma}}.$$

4. LOCALIZED STATE NEAR A PLANAR DEFECT

Considering the case of planar defect, we choose the z axis perpendicular to the plane. The local increase of critical temperature in the plane is described by the term $-\tilde{\gamma} M(x,y,0)\,\delta(z)$ in the magnetic free energy. Analysis of the system of equations analogous to (7) shows that the solution with the highest transition temperature is of the type $M_0^y + iM_0^z$ and $M_0^x = 0$, while the transition temperature is $\delta\tau_c = \frac{3}{16}(2\tilde{\lambda}\tilde{\gamma}^2)^{2/3}$ and the wave vector is directed along the x axis and turns out to be close to q_0 ($\varepsilon = q_0/q_x - 1 = 1/q_0\sqrt{\delta\tau_c/3}$). The magnetic structure of the localized state is

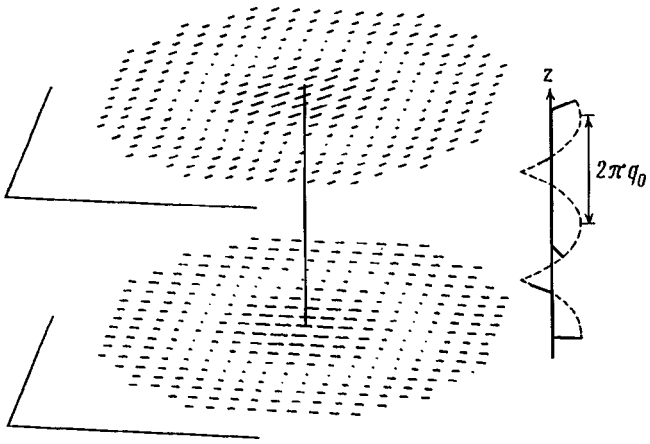

FIG. 2. The magnetic structure for a lineear defect. The z axis is chosen along the defect, and we present the magnetic moment for two planes. The moment is oriented in xy plane and the unit along the z axis corresponds to $\sqrt{2\varepsilon}$ units in the xy plane. This means that the actual structure is obtained by a contraction of $\sqrt{2\varepsilon}$ along the z axis.

$$M^y = M(0)e^{-q_0|z|\sqrt{\varepsilon}}\frac{2}{\sqrt{3}}\sin\left(q_0|z|\sqrt{\frac{\varepsilon}{3}}+\frac{\pi}{3}\right)\cos(q_0 x),$$

$$M^z = M(0)e^{-q_0|z|\sqrt{\varepsilon}}\frac{2}{\sqrt{3}}\sin\left(q_0|z|\sqrt{\frac{\varepsilon}{3}}+\frac{\pi}{3}\right)\sin(q_0 x),$$

and the specific heat jump is

$$\Delta C \simeq \frac{n\theta}{M_S^2 b T_{C0}}\frac{2.12}{q_0\sqrt{\varepsilon}} = 2.12\,\frac{n\theta}{M_S^2 b T_{C0}}\left(\frac{16}{\widetilde{\gamma}\widetilde{\lambda}^2}\right)^{1/3}.$$

5. CONCLUSIONS

We have found the structure of the localized states for systems with helicoidal transitions. It happens that even a small point-like local increase of the transition temperature gives rise to a localized state. The very easy broadening of the helicoidal transitions may be an inherent property. Preliminary data[9] on the specific heat in MnSi support our conclusions. Apparently the main type of defects in MnSi are dislocations. It may be interesting to perform neutron diffraction studies to verify the predictions concerning the structure (see Eq. (8)) of such a linear-defect state. In our analysis we have neglected fluctuations, which could influence the detailed structure of the localized state but would not qualitatively alter our prediction based on the Landau functional approach.

We a grateful to N. Bernhoeft, J. Flouquet, Y. Leroyer, and V. Mineev for helpful discussions and useful comments.

[1] M. I. Kaganov and A. I. Omel'yandchuck, Zh. Éksp. Teor. Fiz. **61**, 1679 (1972) [Sov. Phys. JETP **34**, 895 (1972)].
[2] I. N. Khlustikov and A. I. Buzdin, Adv. Phys. **36**, 271 (1987).
[3] A. P. Levanyuk, V. V. Osipov, A. S. Sigov, and A. A. Sobyanin, Zh. Éksp. Teor. Fiz. **76**, 345 (1979) [Sov. Phys. JETP **49**, 176 (1979)].
[4] L. D. Landau and E. M. Lifshitz, *Quantum Mechanics Pergamon*, Oxford, 1981.
[5] M. L. Plumer, M. B. Walker, J. Phys. C **14**, 4689 (1981).
[6] J. Beille, J. Voicon, M. Roth, Solid State Commun. **47**, 399 (1983).
[7] L. D. Landau and E. M. Lifshitz, *Electrodynamics of Continuous Medium*, Pergamon, Oxford, 1981.
[8] P. G. de Gennes and J. Prost, *The Physics of Liquid Crystals*, Clarendon Press, Oxford, 1993.
[9] N. Bernhoeft (to be published).

Published in English in the original Russian journal. Edited by Steve Torstveit.

Stripe motion in CuO_2 planes of $Y_{1-x}Pr_xBa_2Cu_3O_7$ as observed from the Cu(2) quadrupole resonance

M. A. Teplov, Yu. A. Sakhratov, A. V. Dooglav, A. V. Egorov, E. V. Krjukov, and O. P. Zaitsev
Kazan State University, 420008 Kazan, Russia

(Submitted 24 April, 1997)
Pis'ma Zh. Éksp. Teor. Fiz. **65**, No. 10, 782–787 (25 May 1997)

The NQR spectra of copper in the compounds $YBa_2Cu_3O_7$, $TmBa_2Cu_3O_7$, and $Y_{0.9}Pr_{0.1}Ba_2Cu_3O_7$ at temperatures of 4.2–200 K are investigated by a pulsed NQR technique at frequencies of 28–33 MHz. Quantitative analysis of the spectra shows that the shape of the ''plane'' Cu(2) spectra is well described by using a model of 1D correlations of the charge and spin distribution in the CuO_2 planes (stripe correlations). In the undoped superconductors the charge–spin stripe structure moves fast in the CuO_2 planes, but doping the $YBa_2Cu_3O_7$ lattice with praseodymium slows this motion down. © *1997 American Institute of Physics.* [S0021-3640(97)01110-9]

PACS numbers: 61.72.Hh, 74.72.Bk, 74.80.−g, 76.60.Gv

The hypothesis of 1D ordering of charges and spins in a particular configuration of stripes in CuO_2 planes of $RBa_2Cu_3O_7$ superconductors was suggested two years ago[1] and was later used[2] to explain the NMR and NQR data for $TmBa_2Cu_3O_{6+x}$ and $TmBa_2Cu_4O_8$, but up to now it has not been corroborated directly in the shape of the Cu(2) NQR spectra. In this paper we present such corroboration based on analysis of the Cu(2) NQR spectra for $Y_{1-x}Pr_xBa_2Cu_3O_7$ ($x=0,0.1$) compounds. The $YBa_2Cu_3O_7$ (YBCO) and $Y_{0.9}Pr_{0.1}Ba_2Cu_3O_7$ (YPBCO) samples, prepared by the solid-state reaction method,[3] were kindly placed at our disposal by Xu and Luetgemeier (Forschungszentrum Jǔlich, Germany). The critical temperatures found from susceptibility measurements at a frequency of 1 kHz appeared to be $T_c(\text{onset})=92.5$ and 86 K, respectively. For comparison, besides YBCO and YPBCO, the overdoped compound $TmBa_2Cu_3O_7$ (TmBCO), with a critical temperature of 91.5 K, has also been studied.[2] A home-built spin-echo coherent pulsed spectrometer was used for the copper NQR spectrum measurements.

The examples of YBCO and YBPCO spectra are shown in Fig. 1. It is seen (Fig. 1a,c) that, except the relatively narrow ^{63}Cu(2) and ^{65}Cu(2) NQR lines, both spectra have a broad ''pedestal.'' Representing these spectra on a logarithmic scale (Fig. 1b,d), one can clearly see the asymmetry of the narrow lines, i.e., these lines also have a complex composition in the sample doped with praseodymium.

We managed to get the best fit of the YBCO spectra to six Gaussian curves, three for each isotope: the narrow Gaussian line A', the broad one A'', and the pedestal P. The frequencies ν_i and mean square linewidths $\Delta\nu_i$ of each pair of isotope lines were supposed to be related by the ratio of nuclear quadrupole moments $\alpha={}^{65}Q/{}^{63}Q$

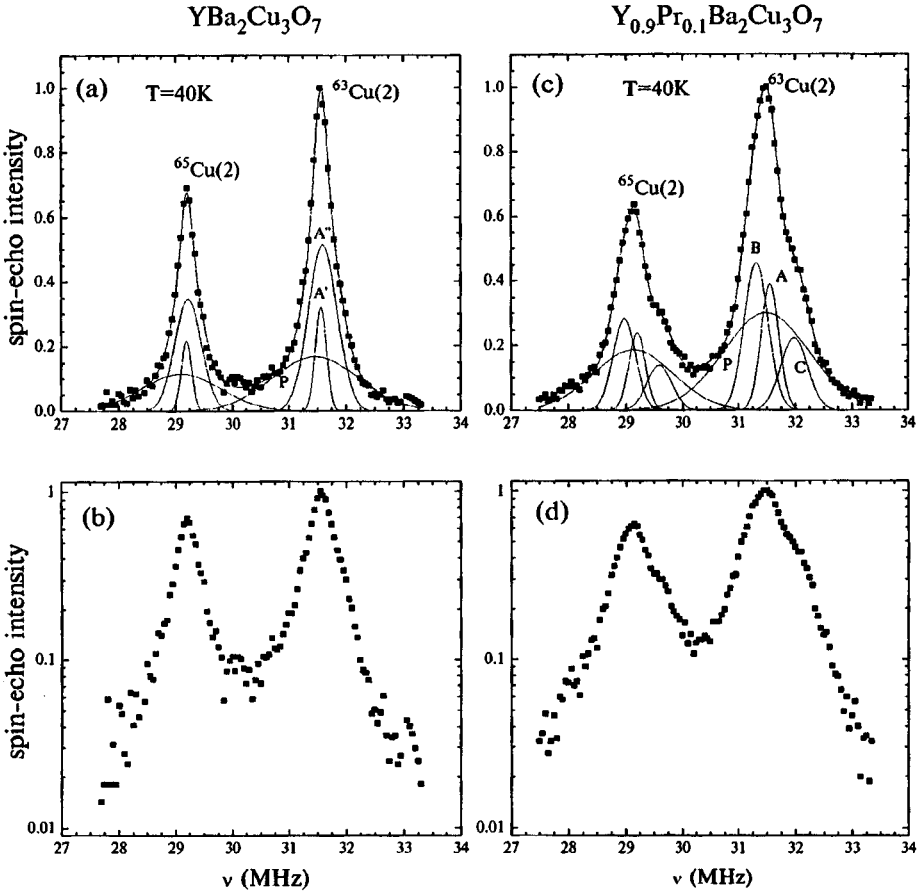

FIG. 1. Copper NQR spectra for $YBa_2Cu_3O_7$ (a,b) and $Y_{0.9}Pr_{0.1}$ $Ba_2Cu_3O_7$ (c,d) taken at $T=40$ K; the solid lines are a best fit (see text and Fig. 2).

($^{65}\nu_i=\alpha^{63}\nu_i$, $^{65}\Delta\nu_i=\alpha^{63}\Delta\nu_i$, $i=A',A'',P$). Thus the fitting function involved 10 parameters: three line frequencies $^{63}\nu_i$, three linewidths $^{63}\Delta\nu_i$, three line intensities $^{63}a_i$ and the ratio $b=^{65}a_i/^{63}a_i$. While fitting the YBCO spectra taken at temperatures 200–4.2 K it was found that the pedestal linewidth (1.5 ± 0.1 MHz) did not depend on temperature, so its value was taken fixed at 1.5 MHz during the final fitting procedure (the results of which are shown in Fig. 1a and Fig. 2a,b,c), thus reducing the total number of fitting parameters to 9. It should be mentioned here that the presence of a pedestal is typical for copper NQR spectra in 1-2-3-7 compounds (but not in 1-2-4-8 compounds[2]). We observed it in the spectra of Tm1-2-3-7 and Y1-2-3-7 samples prepared in different laboratories;[4] in some of them the pedestal looked like several poorly resolved overlapping lines and, in particular, contained the broad NQR line of twofold coordinated ''chain'' $^{63}Cu(1)_2$ copper at a frequency of 30.1 MHz. We suppose the spectrum P to arise from Cu(1) and Cu(2) centers which are located in areas with a partly disordered oxygen sublattice of CuO planes and, respectively, with a reduced (and locally inhomo-

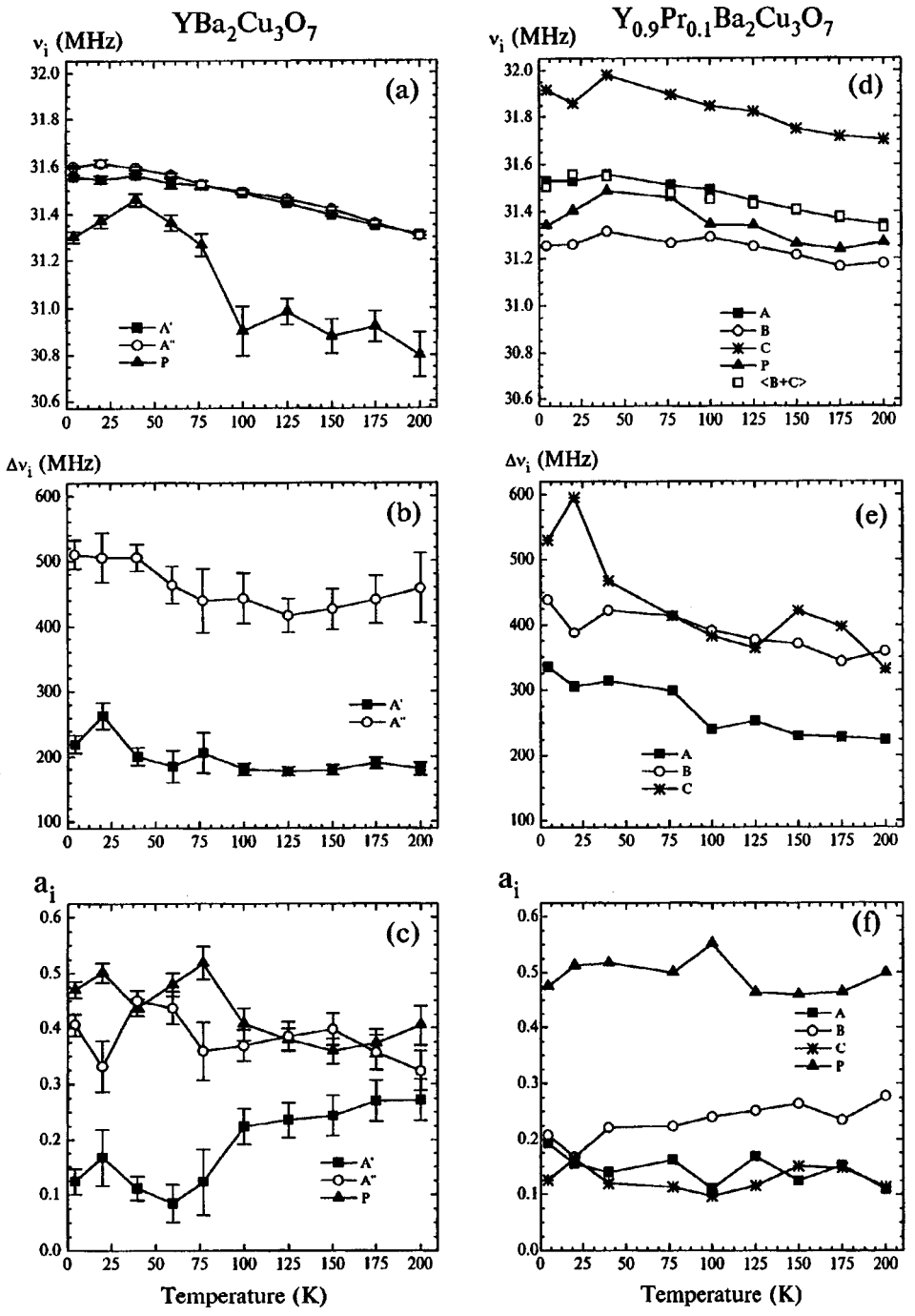

FIG. 2. Temperature dependence of parameters of copper NQR spectra for $YBa_2Cu_3O_7$ (a,b,c) and $Y_{0.9}Pr_{0.1}Ba_2Cu_3O_7$ (d,e,f); see text for details.

geneous) hole concentration in the CuO_2 planes. Extracting the sum $(A'+A'')$ from the observed spectrum, we obtain the spectrum of the ''good'' superconductor, free (or almost free) of crystal structure defects. Actually this procedure allowed us to obtain (for the first time, to our knowledge) a quantitative description of the Cu(2) NQR line shape for the superconductor with the 1-2-3-7 orthorhombic structure. A comparative analysis of spectra for YBCO (Fig. 1a and 2a,b,c) and TmBCO (Ref. 4) has shown that the lineshape is intermediate between Gaussian and Lorentzian, and for both samples the same relation holds between the parameters describing the lines A' and A''. In particular, in the temperature range 100–150 K we have obtained $\nu_{A'}=\nu_{A''}$, $\Delta\nu_{A''}/\Delta\nu_{A'}=2.4(1)$ and $a_{A''}/a_{A'}=1.64(5)$, although the linewidths $\Delta\nu_i$ for TmBCO appeared to be 25–30% larger than those for YBCO.

In order to describe the copper NQR spectra shape for YPBCO sample we used a fitting function containing four Gaussians for each isotope: besides the pedestal (its linewidth $^{63}\Delta\nu_P$ was again taken equal to 1.5 MHz), the central line A (since the frequencies $\nu_{A'}$ and $\nu_{A''}$ are close in YBCO, we considered it possible to restrict the description of this line in YPBCO to one line) and the satellite C on the right-hand slope of the spectrum, we introduced a line B located at a frequency $\nu_B<\nu_A$ in the spectrum (the presence of this line is revealed by the bulging left-hand slope of the ^{63}Cu line in Fig. 1d). Thus the fitting function contained 12 parameters: four frequencies $^{63}\nu_i$, three linewidths $^{63}\Delta\nu_i$, four intensities $^{63}a_i$, and the intensity ratio $b=^{65}a_i/^{63}a_i$. The results of fitting of YBCO spectra taken at 200–4.2 K are given in Fig. 2d,e,f. Let us point out and discuss the main features of the copper NQR spectra for YBCO, TmBCO, and YPBCO samples.

1. The integral intensity of the pedestal P is the same for YBCO and TmBCO and equals approximately to 1/3, but for YPBCO it increases to $\sim 1/2$; this confirms our assumption that the component P of the spectra belongs to a partly disordered phase of the compounds studied.

Other remarks pertain to the ''pure'' spectra of the Cu(2) NQR, characterized by the components A', A'' (YBCO, TmBCO), and A, B , C (YPBCO).

2. In the spectra of YBCO (Fig. 2a,b,c) and TmBCO (Ref. 4) at temperatures of 100–200 K the frequencies $\nu_{A'}$ and $\nu_{A''}$ are approximately equal to each other, and $\nu_{A'}<\nu_{A''}$ at $T<T_c$. In general the difference of these frequencies is small ($<0.2\%$), so that for rough estimates it is possible to assume that the sum $(A'+A'')$ describes a single Cu(2) NQR line in the YBCO and TmBCO samples.

3. The temperature dependence of the frequency of this line in the YBCO spectrum is the same as the temperature dependence of the line A in the spectrum of the YPBCO sample (cf. Figs. 2a and 2d). This allows us to ascribe the line A (Fig. 2d) to Cu(2) nuclei which are located far away from Pr atoms and not influenced by them. Let us call these nuclei ''remote.''

4. The main result of this paper is the temperature dependences of the parameters of the lines A, B, and C for YPBCO (Fig. 2d,e,f).

We ascribe the lines B and C, which are absent in the YBCO spectrum (Fig. 2a), to the ''neighboring'' nuclei, i.e., to those located not far from Pr atoms. Comparing the integral intensities a_i of the lines at temperatures above T_c (when the spectra are free of possible distortions due to different penetration depth of the rf field H_1 into areas with

different local concentrations of holes), we obtain the same ratio of the mean intensities, viz., $\langle a_B \rangle : \langle a_C \rangle = 2:1$, as that following from the model of quasi-1D ordering of charges and spins in the CuO_2 planes (stripe model).[1] Furthermore, we have noticed that the lines B and C are located asymmetrically with respect to the line A, but in such a way that $(\nu_B a_B + \nu_C a_C)/(a_B + a_C) = \nu_A$ (open squares in Fig. 2d). These two facts immediately suggest the idea that both spectra, those for the ''remote'' nuclei (A) and for the ''neighboring'' nuclei ($B+C$), belong to stripes moving in the CuO_2 planes, the only difference between them being different rates of motion: for ''remote'' nuclei the case of fast motion is realized, while for the ''neighboring'' nuclei — slow motion. Two types of Cu(2) centers are distinguished in the model[1] — those located at the center of the stripe (type C, the hole density on the oxygen ligands is high), and those at the stripe boundaries (type B, the hole density is low), so that at the optimal doping of the CuO_2 planes by holes and for close packing of the stripes, the number of centers B is twice as large as that of centers C. The shape of the Cu(2) NQR spectrum in the system of moving stripes can be described by the following function:[5]

$$I(\omega,\Omega) = \frac{W_B W_C (\omega_B - \omega_C)^2 (\tau_B + \tau_C)\tau_B \tau_C}{[\tau_B \tau_C (\omega - \omega_B)(\omega - \omega_C)]^2 + [\tau_B (\omega - \omega_B) + \tau_C (\omega - \omega_C)]^2}, \tag{1}$$

where W_i is the probability of finding the nucleus in the ith state, and τ_i and $\omega_i = \Omega + \Delta_i$ are the lifetime of this state and the corresponding NQR frequency, respectively. Actually, since the frequency Ω is randomly distributed about the mean value $\langle \Omega \rangle = \omega_0$ (quadrupole broadening due to lattice imperfections), the spectrum shape is obtained by averaging Eq. (1) with the Gaussian distribution of Ω:

$$S(\omega) \sim \int I(\omega,\Omega) \exp[-(\Omega - \omega_0)^2/2\sigma^2] d\Omega. \tag{2}$$

The ^{63}Cu(2) NQR spectrum taken at 100 K is shown by circles in Fig. 3a, the squares in Fig. 3b depict the spectrum $^{63}(B+C)$ for the ^{63}Cu isotope, obtained by subtraction of three lines (^{63}A, ^{63}P, and the P component for the ^{65}Cu isotope) from the experimental spectrum (Fig. 3a), and the triangles in Fig. 3c display the $^{63}(A+B+C)$ spectrum. The solid line in Fig. 3b represents the calculated spectrum $S_{B+C}(\omega)$ obtained at the following values of the parameters: $\Delta_B = -\Delta = -2\pi \cdot 217 \times 10^3$ s^{-1}, $\Delta_C = 2\Delta$, $\tau_C = \tau = 2.9 \times 10^{-6}$ s, $\tau_B = 2\tau$, $\omega_0 = 2\pi \cdot 31.465 \times 10^6$ s^{-1}, $\sigma = 2\pi \cdot 159 \times 10^3$ s^{-1}. One can see that the experimental spectrum S_{B+C} of the ''neighboring'' nuclei and the total NQR spectrum ($S_A + S_{B+C}$) are described very well in the framework of our model of moving stripes (Fig. 3b,c). The spectrum of ''remote'' nuclei (dashed line S_A in Fig. 3c) is obtained at the same Δ_B, Δ_C values, but when a short lifetime τ ($< 10^{-7}$ s) is assumed; the frequency of the line A appears to be 0.09% higher (this corresponds to a higher mean concentration of the holes), and the quadrupolar linewidth 25% less than the corresponding parameters for ''neighboring'' nuclei. Thus far away from impurity Pr ions the velocity of the stripes is high, and the corresponding lifetime τ is very small and cannot be evaluated in the present experiment.

Two conclusions can be inferred from the above: 1) fast motion of the stripes in the CuO_2 planes seems to be necessary for cuprates to superconduct; 2) Pr doping leads to

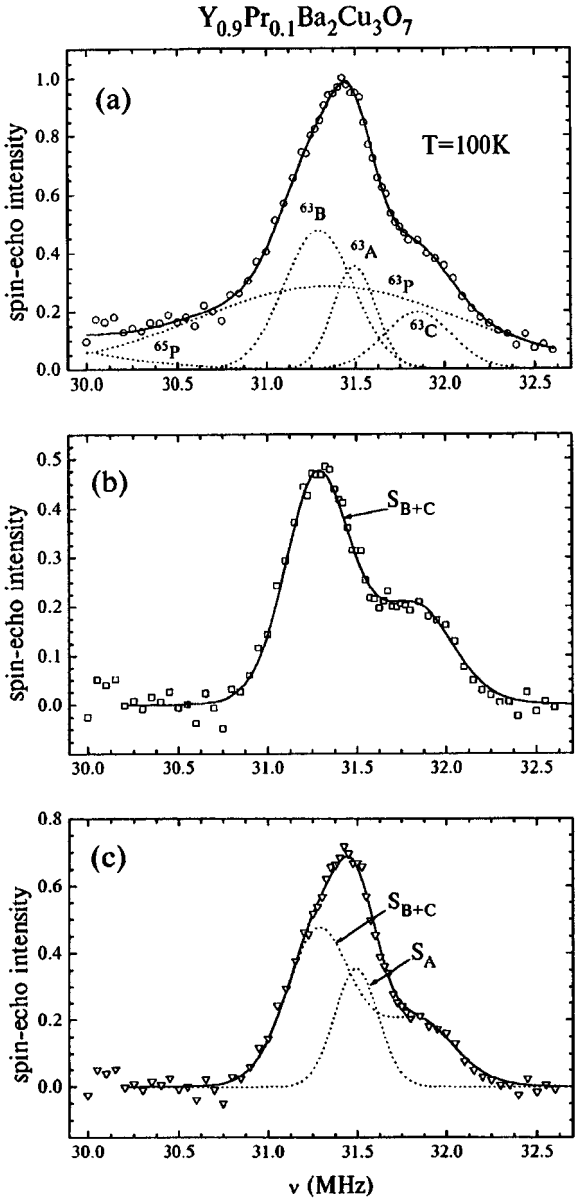

FIG. 3. Fragments of ^{63}Cu(2) NQR spectra for $Y_{0.9}Pr_{0.1}Ba_2Cu_3O_7$ at $T=100$ K: (a) — best fit to the sum of five Gaussian curves $^{63}(A+B+C+P)$ and ^{65}P; (b) — best fit to the $^{63}(B+C)$ contribution according to Eqs. (1) and (2) with the parameters $\Delta_B/2\pi=-217$ kHz, $\Delta_C/2\pi=434$ kHz, $\tau_C=2.9$ μs, $\tau_B=2\tau_C$, $\omega_0/2\pi=31.465$ MHz, $\sigma/2\pi=159$ kHz; (c) — the same as (b) with the addition of the ^{63}A contribution, with parameters $\Delta_B/2\pi=-217$ kHz, $\Delta_C/2\pi=434$ kHz, $\tau_C<10^{-7}$ s, $\tau_B=2\tau_C$, $\omega_0/2\pi=31.492$ MHz, $\sigma/2\pi=119$ kHz.

the pinning of the stripes, resulting in a suppression of superconductivity in

$Y_{1-x}Pr_xBa_2Cu_3O_7$. The 1D correlations in the charge and spin distributions remain valid in the latter case, too, but they become static in character.

We are indebted to Dr. Y. Xu and Dr. H. Luetgemeier for the samples placed at our disposal. Valuable discussions with V. A. Atsarkin, M. V. Eremin, and V. F. Gantmakher are gratefully aknowledged. This work was conducted as a part of the Russian State Program ''Superconductivity'' (Grant 94029) and the International Russian–German Program ''Spectroscopy of High-T_c Superconductors.''

[1] O. N. Bakharev, M. V. Eremin, and M. A. Teplov, JETP Lett. **61**, 515 (1995).
[2] M. A. Teplov, A. V. Dooglav, E. V. Krjukov *et al.*, Zh. Éksp. Teor. Fiz. **109**, 689 (1996) [JETP **82**, 370 (1996)]; M. A. Teplov, E. V. Krjukov, A. V. Dooglav *et al.*, JETP Lett. **63**, 227 (1996); O. N. Bakharev A. V. Dooglav, A. V. Egorov *et al.*, JETP Lett. **64**, 398 (1996); M. A. Teplov, O. N. Bakharev, A. V. Dooglav *et al., Proceedings of the NATO ASI ''Materials Aspects of High T_c Superconductivity: 10 Years After the Discovery''* (Delphi, 19–31 Aug. 1996), Kluwer, Dordrecht (in press).
[3] Y. Xu and W. Guan, Solid State Commun. **80**, 105 (1991).
[4] A. V. Egorov, Yu. A. Sakhratov, M. A. Teplov *et al.*, (to be published).
[5] P. W. Anderson, J. Phys. Soc. Jpn. **9**, 316 (1954); C. P. Slichter, *Principles of Magnetic Resonance*, 3rd ed., Springer-Verlag, New York, 1992; L. K. Aminov and M. A. Teplov, Usp. Fiz. Nauk. **147**, 49 (1985) [Sov. Phys. Usp. **28**, 762 (1985)].

Published in English in the original Russian journal. Edited by Steve Torstveit.

Observation of stochastic resonance in a monostable magnetic system

A. N. Grigorenko,[a)] P. I. Nikitin, and G. V. Roshchepkin
Institute of General Physics, Russian Academy of Sciences, 117942 Moscow, Russia

(Submitted 26 March 1997; resubmitted 21 April 1997)
Pis'ma Zh. Éksp. Teor. Fiz. **65**, No. 10, 788–792 (25 May 1997)

A stochastic resonance on mixed harmonics is observed experimentally in a monostable magnetic system. The curve of the stochastic resonance at higher-order harmonics in systems with a weak nonlinearity is calculated. © *1997 American Institute of Physics.*
[S0021-3640(97)01210-3]

PACS numbers: 75.40.Cx, 75.30.Cr, 05.40.+j

In recent years stochastic resonance (SR), which can be defined as a noise-induced increase in the signal-to-noise ratio, has been attracting a great deal of attention from investigators.[1–10] This is due to both the fundamental character of the phenomenon (stochastic resonance is a substantial advance in the theory of nonlinear susceptibilities) and possible interesting applications.[9] Up to now SR has been observed in systems with a threshold and in bistable systems. At the same time, the interesting possibility that a divergent signal-to-noise ratio can exist in monostable systems of a special type has been demonstrated in Ref. 10.

Stochastic resonance in a bistable magnetic system was proposed in Ref. 6 and detected experimentally in Ref. 8. In this letter we report the experimental observation of stochastic resonance at higher-order harmonics in a monostable magnetic potential. We also shows that SR at mixed harmonics has a wider range of applications than SR at the fundamental harmonic and can be observed in various monostable systems.

Consider a physical system subjected to harmonic modulation and a random noise force. With weak noise and weak modulation the system moves in a linear region near the equilibrium state and, in consequence, generates virtually no higher-order harmonics. The application of sufficiently strong noise drives the system out of the linear into a nonlinear region where mixing of the harmonics occurs. This increases the signal-to-noise ratio at the higher-order harmonics, i.e., it results in a SR peak.

OBSERVATION OF SR IN A MONOSTABLE SYSTEM

As a model system for observing SR at higher-order harmonics in a monostable potential, we chose a solitary domain wall (DW) in an easy-axis iron-garnet film stabilized by a gradient of an external magnetic field. For not too high frequencies, the DW moves by jumps of local sections which interact with microdefects in the sample.[11] The DW was fixed in the monostable potential of a microdefect, and the response of the DW to an applied harmonic and random noise magnetic fields was studied as a function of the intensity of the noise field. The response, consisting of a change in the magnetization of

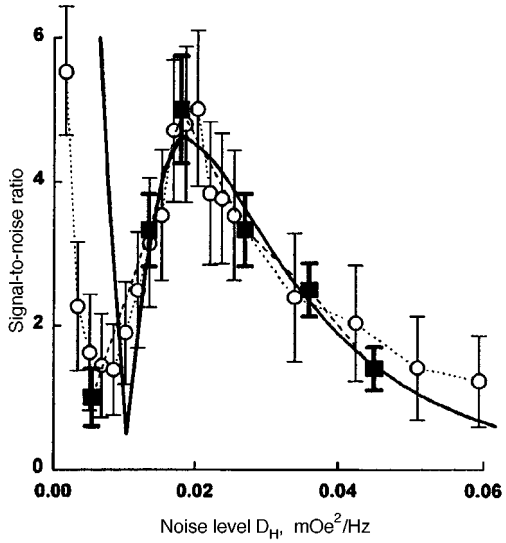

FIG. 1. Signal-to-noise ratio for a local section of a DW as a function of the magnetic-field noise intensity: measured values (□), computer simulation (○ and dotted curve), and SR curve (solid line) calculated using Eqs. (6) and (7).

a $5\times5\times30$ μm local section of the sample illuminated by a laser, was measured by a standard magnetooptic method. The fields were applied with the aid of coils with inductance $L\sim10$ μH and conversion ratio ~10 Oe/A. The random magnetic field generator produced noise in the frequency range up to 20 kHz. The harmonics were detected with a selective nanovoltmeter, which was also used to determine the noise intensity. The experimental setup and measurement procedure are described in greater detail in Ref. 12.

Figure 1 displays the stochastic resonance curve measured at the third harmonic in the monostable potential of a defect. The curve was obtained for a $(LuBi)_3(FeGa)_5O_{12}$ film 30 μm thick, with an anisotropy of 1800 Oe, a magnetization of 80 G, a stripe period of 25 μm, and a DM mobility $\mu=10^3$ cm/Oe·s. The gradient of the external magnetic field was equal to $\beta=15$ kOe/cm, and the internal gradient of the defect was equal to $\beta_0=100$ kOe/cm. The modulation frequency was equal to 1.1 kHz, the amplitude was equal to 20 mOe, and the detection frequency was equal to 3.3 kHz. The SR peak was observed with a random noise field of intensity $D_H=0.018$ (mOe)^2/Hz, which corresponds to a random force of strength $D=\mu^2D_H=0.018$ cm^2/s ($f_{\rm ran}=\mu H_{\rm ran}$). This strength should be compared with the energy of the defect $U_{\rm eff}=\mu H_{\rm b}\delta=0.016$ cm^2/s, where $H_{\rm b}$ is the field for breakaway of the defect and $\delta=0.4$ Oe is the radius of influence of the defect.

Figure 1 also displays the result of the numerical simulation of the motion of the DW, described by the equation

$$dx/dt=-dU/dx+\mu H\cos(\omega t+\varphi)+\mu H_{\rm ran}(t), \tag{1}$$

where $H_{\text{ran}}(t)$ is the random magnetic field, which satisfies $\langle H_{\text{ran}}(t_1)H_{\text{ran}}(t_2)\rangle = 2D_H\delta(t_1-t_2)$, in the monostable potential

$$U(x) = \frac{\mu\beta x^2}{2} + \frac{\mu\beta_\delta x^2}{2}\exp\left(-\frac{2x^2}{\delta^2}\right), \tag{2}$$

produced by the gradient of an external magnetic field and the field of the defect. The values of the main parameters ($\mu = 10^3$ cm/Oe·s, $\beta = 15$ kOe/cm, $\beta_\delta = 100$ kOe/cm, $\delta = 0.4$ μm, and $H = 50$ mOe) corresponded to the experimental values. The equation (1) was reduced to a dimensionless form by means of the substitutions $x/\delta \to x$ and $\mu\beta t \to t$ and integrated numerically by a second-order Runge–Kutta method. The time ensemble of the DW positions obtained with a prescribed time series of the random force was used to obtain the correlation function and the spectral density (the initial dynamics of the system during the first ten relaxation times of the system was neglected). To decrease the random error, which in our case was equal to $\sim 10\%$ for the spectral density of the signal and $\sim 20\%$ for the signal-to-noise ratio, the spectral density was averaged over the phase φ of the periodic magnetic field (initial time) and also over ~ 700 different time series of the noise. A standard Gaussian white noise generator was used, and the numerical integration step ($\Delta t = 0.005$) was chosen to be small enough so that changing it did not change the results substantially.

As one can see from Fig. 1, the signal-to-noise ratio obtained by numerical integration agrees well with the measured curve.

SR AT HIGHER-ORDER HARMONICS IN A SYSTEM WITH WEAK NONLINEARITY

Let us consider a system moving in a parabolic potential $U_0(x) = ax^2/2$ and perturbed by a weak nonlinearity $u(x)$:

$$\dot{x} = -ax - u'(x) + f_0\cos(\omega_0 t) + \xi(t), \tag{3}$$

where $f_0\cos(\omega_0 t)$ is a small periodic modulation and $\xi(t)$ is white noise with $\langle \xi(\overline{t})\xi(t)\rangle = 2D\delta(\overline{t} - t)$. Writing the solution in the form

$$x(t) = X_0(t) + X_{\text{n}}(t) + \eta(t), \tag{4}$$

where $X_0(t)$ are small oscillations produced by a periodic force in the absence of noise and nonlinearity, $X_{\text{n}}(t)$ is an Ornstein–Uhlenbeck process produced by the noise, and $\eta(t)$ are small corrections due to the nonlinearity $u(x)$. To first order in $u(x)$, we obtain after simple calculations

$$\langle \eta(\overline{t})\eta(t)\rangle = \exp(-a(\overline{t} + t))\int_{-\infty}^{\overline{t}}\int_{-\infty}^{t}\exp(a(\overline{\tau} + \tau))K(\overline{\tau}, \tau)d\,\overline{\tau}\,d\,\tau,$$

$$K(\overline{\tau}, \tau) = \int_{-\infty}^{\infty}\int_{-\infty}^{\infty}u'(X_0(\overline{\tau}) + \overline{x})\rho_1(\overline{x} - x, \overline{\tau} - \tau)u'(X_0(\tau) + x)\rho_0(x)d\,\overline{x}\,dx, \tag{5}$$

where $\rho_0(x) = \sqrt{a/2\pi D}\,\exp(-ax^2/2D)$ is a stationary distribution and $\rho_1(\overline{x} - x, \overline{\tau} - \tau)$ is the transition probability for the Ornstein–Uhlenbeck process.

For simplicity we assume that $\omega_0 \ll a$, so that the region $\overline{\tau} - \tau \gg 1/a$, where $\rho_1(\overline{x} - x, \overline{\tau} - \tau) \approx \rho_0(\overline{x})$, makes the main contribution to expression (5). Then, expanding expression (5) with respect to $X_0(t)$ and including noise to zeroth order, we obtain as the final result for the signal-to-noise ratio at the nth harmonic ($n \geqslant 2$):

$$R_{n\omega} = \frac{\pi q_n^2 f_0^{2n}}{2^{n-1}(n!)^2 a^{2n} D \Delta\nu}, \tag{6}$$

where $\Delta\nu$ is the detectable frequency band and

$$q_n = \int_{-\infty}^{\infty} \rho_0(x) u^{n+1}(x) dx = \sqrt{\frac{a}{2\pi D}} \int_{-\infty}^{\infty} \exp\left(-\frac{ax^2}{2D}\right) u^{(n+1)}(x) dx, \tag{7}$$

where $u^{(n)}(x)$ is the nth spatial derivative.

It is easy to see that Eqs. (6) and (7) imply the existence of an optimal noise intensity for which the maximum signal-to-noise ratio obtains. In the general case, an exponential factor $\exp(-al^2/D)$, where l is the effective length characterizing the potential $u(x)$, can be separated out in the integral (7). Together with the factor D in the denominator in Eq. (6), this gives the SR peak.

For the experimental system under study the conditions under which expressions (6) and (7) obtain are satisfied for noise levels greater than the energy of the defect. (The frequency 3 kHz of the external force was much lower than the relaxational frequency of the system ~ 15 MHz, the amplitude of the external force $H = 50$ mOe was much lower than the characteristic force $H_b \sim 0.4$ Oe of the defect, and the potential of the defect could be regarded as a perturbation with respect to the parabolic potential of the gradient magnetic field at an average energy of the system greater than the energy of the defect.) A curve of the stochastic resonance at the third harmonic is displayed in Fig. 1. The curve was calculated using expressions (6) and (7) for the potential (2), whose parameters corresponded to the experimental potentials of a magnetic defect and an external gradient magnetic field. For high noise intensities, the curve agrees with the experimental data and the results of numerical simulation.

As another example, let us examine the case when the nonlinearity is concentrated near a point x_0:

$$u(x) = \epsilon \exp\left(-\frac{(x - x_0)^2}{2\lambda^2}\right). \tag{8}$$

Calculating the integral (7), we find the signal-to-noise ratio at the second harmonic

$$D \ll a\lambda^2, \quad R_{2\omega} = \frac{\pi x_0^6 \epsilon^2 f_0^4}{8a^4 \lambda^{12} D \Delta\nu} \exp\left(-\frac{x_0^2}{\lambda^2}\right),$$

$$D \gg a\lambda^2, \quad R_{2\omega} = \frac{\pi a x_0^2 \lambda^2 \epsilon^2 f_0^4}{8D^6 \Delta\nu} \left(3 - \frac{ax_0^2}{D}\right)^2 \exp\left(-\frac{ax_0^2}{D}\right). \tag{9}$$

In this elementary example the stochastic-resonance peak exists only for $\lambda < x_0/4$, i.e., under conditions for which the nonlinearity is sufficiently localized. Furthermore, the SR peak for high noise intensities can actually be described by the expression

$$R_{2\omega} \approx \frac{C}{D^8} \exp\left(-\frac{ax_0^2}{D}\right),$$

similar to the formula for a stochastic resonance at the fundamental harmonic.

The result presented makes clear the physical reason for the analogy. Indeed, the SR signals are generated at some nonzero energy. For the potential (8) this energy is $U_0 = ax_0^2/2$, where the nonlinearity is concentrated. The probability of finding the system near this energy is proportional to $\exp(-U_0/D)$. This gives the factor $\exp(-2U_0/D)$ for the correlation function, which is a product of two coordinates of the system taken at different times. The factor $1/D^n$ arises from the spectral noise density and the capacity of the system to generate signals.

In summary, we have shown that stochastic resonance at higher-order harmonics does not require bistability and can be observed in different types of monostable systems.

This work was supported by the Russian Fund for Fundamental Research under Grants Nos. 96-02-18956 and 96-02-19608 and by INTAS under Grant No. 94-1720.

[a)]e-mail: grig@kapella.gpi.ru

[1] R. Benzi, A. Sutera, and A. Vulpiani, J. Phys. A **14**, L453 (1981).
[2] R. Benzi, G. Parisi, A. Sutera *et al.*, Tellus **34,** 10 (1982).
[3] B. McNamara and K. Wiesenfeld, Phys. Rev. A **39**, 4854 (1989).
[4] L. Gammaitoni, F. Marchesoni, E. Menichella-Saetta *et al.*, Phys. Rev. Lett. **62**, 349 (1989).
[5] M. I. Dykman, P. V. E. McClintock, R. Mannella, and N. Stokes, JETP Lett. **52**, 141 (1990).
[6] A. N. Grigorenko, V. I. Konov, and P. I. Nikitin, JETP Lett. **52**, 593 (1990).
[7] R. Bartussek, P. Jung, and P. Hanggi, Phys. Rev. E **49**, 3930 (1994).
[8] A. N. Grigorenko, P. I. Nikitin, A. N. Slavin *et al.*, J. Appl. Phys. **76**, 6335 (1994).
[9] K. Wiesenfeld and F. Moss, Nature **373**, 33 (1995).
[10] J. M. G. Vilar and J. M. Rubi, Phys. Rev. Lett. **77**, 2863 (1996).
[11] A. N. Grigorenko, S. A. Mishin, A. M. Prokhorov *et al.*, Fiz. Tverd. Tela (Leningrad) **30**, 2948 (1988) [Sov. Phys. Solid State **30**, 1699 (1988)].
[12] A. N. Grigorenko, P. I. Nikitin, and G. V. Roschepkin, Zh. Éksp. Teor. Fiz. **111** (1997) [*sic*].

Translated by M. E. Alferieff